Modeling and production of metal nanoparticles through laser ablation and applications to photocatalytic water oxidation

PhD candidate: Alberto Mazzi

Supervisor: prof. Antonio Miotello

UNIVERSITY OF TRENTO
Department of Physics
Doctoral Program in Physics
XXIX Cycle

March 2017

Modeling and production of metal nanoparticles through laser ablation and applications to photocatalytic water oxidation

by

Alberto Mazzi

B.S. in Physics University of Padova, Italy (2011)
M.S. in Physics University of Padova, Italy (2013)

Thesis submitted to the Doctoral Program in Physics
in partial fulfillment of the requirements for the degree of
Doctor of Philosophy in Physics

Committee members:

Prof. Vincenzo Amendola
Department of Chemical Sciences
University of Padova, Italy

Prof. Leonid V. Zhigilei
Department of Materials Science and Engineering
University of Virginia, USA

Prof. Francesco Pederiva
Department of Physics
University of Trento, Italy

To my parents

To Veronica and our future family

Abstract

The contents of the present thesis can be divided into three parts. The first three chapters introduce the general context in which this work was developed: the social impact, the motivations and the key concepts of our research field. In particular, in Chapter 1 we discuss about the energy issue, focusing on the problem of sustainability of the energy sources. Through an analysis of updated energy and population statistics, we come to the conclusion that solar energy is the most environmentally, economically and socially sustainable energy source. Then, in Chapter 2 we present the basics of photoelectrochemical water splitting, as a possible strategy of solar hydrogen production. This discussion is inserted in the more general topic of artificial photosynthesis toward solar fuel generation. In view of the experimental work presented in this thesis, we put attention on semiconductor-based photoelectrochemical water splitting and on heterogeneous catalysis with inorganic catalytic materials. More specifically, we propose physical vapor deposition techniques as synthetic methods suitable for the industrial production of thin films for photoelectrochemical applications. In Chapter 3 we introduce the fundamentals of physical vapor deposition techniques (namely, radiofrequency magnetron sputtering, electron-beam deposition and pulsed laser deposition).

The second part highlights some fundamental mechanisms that are relevant in the pulsed laser ablation of metals. In particular, we review our recent results on the modeling of liquid nanodroplet formation in the nanosecond laser ablation of pure metals. Chapter 4 develops a simplified model of phase explosion, based on the theory of homogeneous boiling. Through a continuum approach, we describe the liquid nanoparticle formation in a metastable liquid metal, whose temperature is constant over time and space. The results of our computational simulations are presented here for a set of seven metals (Al, Fe, Co, Ni, Cu, Ag and Au), commonly used in pulsed laser deposition. Our modeling was further improved, taking into account a more realistic spatial and temporal dependence of the temperature. In Chapter 5 we design a simulation of the nanosecond laser ablation of aluminum, which considers phase explosion and vaporization mechanisms. A nanosecond Gaussian-shaped laser pulse was assumed and the spatial gra-

dient of the temperature was calculated according to the heat conduction equation. In this way, space–time resolved homogeneous boiling was studied and the size distribution of the produced liquid nanodroplets is presented.

After this long digression on the fundamentals of laser ablation mechanisms, we return to focus on the application of physical vapor deposition techniques to the synthesis of solid-state thin layers for photoelectrochemical water splitting. This third part is composed of three chapters, each one dealing with a different physical vapor deposition technique. Chapter 6 presents the synthesis and characterization of tin-doped hematite through radiofrequency magnetron sputtering. That study allowed us to shed some light on the effect of tin doping on the structural, optical and electrochemical properties of hematite. Indeed, tin-doped hematite was studied as a photoanodic material in some considerable experimental works, but the employed techniques made difficult to decouple the effect of the dopant from other structural and morphological features. Chapters 7 and 8 present the results of our work on the pulsed laser deposition and electron-beam deposition of water oxidation catalysts, respectively. In particular, Chapter 7 proposes the synthesis of a porous amorphous iron oxide catalyst employed to functionalize hematite photoanodes. The small-scale nanostructuring obtained through pulsed laser deposition allowed minimizing some issues such as the parasitic light absorption. In Chapter 8 we characterize pure and binary metal oxide thin films based on Fe, Co and Ni, deposited through electron-beam deposition. In our investigation of the electrocatalytic performance of these water oxidation catalysts, $NiFe_2O_x$ results as the most active material, in agreement with recent literature.

Contents

x

Chapter 1

Energy demand and global warming

1.1 An unsustainable economy

In the long story of our planet, the last few centuries represent an unprecedented event. Compared to the previous ages, the human population has experienced a high growth rate, especially as a consequence of the industrial revolutions. The big innovations in the technical and sanitary tools allowed a progressive improvement of the life expectancy and quality. Of course, any human activity requires energy and causes some sort of change in the environment where we live. The increasingly energy intensive human activities multiplied by the growing world population produced in the last three centuries an increasing environmental impact of mankind. This rapid escalation led to the fact that a single species is now altering the natural evolution of the global environment, so that the scientists formulated the concept of Antropocene, as a human-dominated geological epoch [1].

Alongside the environmental considerations, the current use of the primary energy sources available on our planet is clearly unsustainable. In order to evaluate the sustainability of the global economy and more specifically of the energy policies we can split this problem in two parts. Firstly, we need to understand how much demanding is the global energy consumption compared to the energy potentially available on our planet. Secondly, we should evaluate if the share of energy obtained from the different primary energy sources is congruous with their availability.

In the last years, the global average power consumption has been of the order of 15 TW [2], mostly obtained from fossil fuels. On the other hand, if we want to estimate the global power availability on Earth, we can consider that all the forms of energy sources that we use, with the only exception of nuclear and geothermal power, are someway due to solar-driven processes,
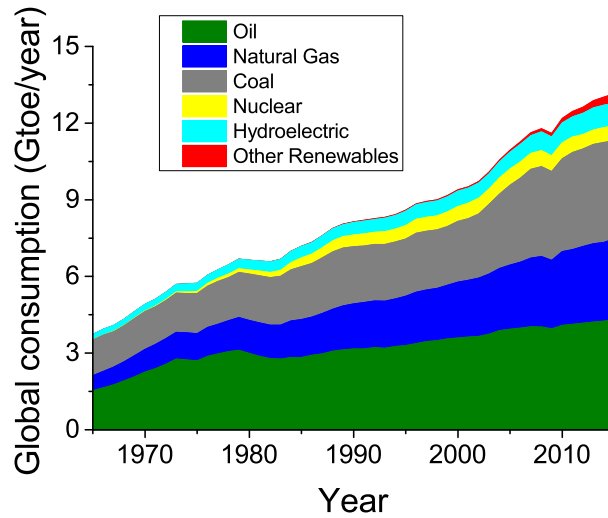
Figure 1.1: Global consumption of primary energy sources in gigatonnes of oil equivalent (Gtoe) per year.

such as photosynthesis, the water cycle or the atmospheric phenomena. For this reason, the total solar power that is collected by our planet can give a reasonable estimate of the power that our planet is able to provide us on a long-term. The average power density of solar radiation on the Earth's surface is of about 170 Wm^{-2} that, integrated over the entire surface gives the enormous amount of 90 PW [3]. This is of course a crude overestimation of the power that is potentially available on our planet, but this tells us that the energy issue is not currently motivated by a limit of available sources, but it is rather due to the problem of efficiently exploit the energy available in a convenient form.

In the last fifty years, the global energy demand has increased almost linearly, as shown in Fig. 1.1, despite the effect of the economic or geopolitical crisis that for some years caused a reduction of demand or a rationing of the energy sources in some affluent countries. On the global, long-term scale, there is a clear tendency to a quite stable growth of the energy consumption that, especially considering the recent evolution of the developing countries, will reasonably continue for the next decades. At present, more than 85% of the global energy is obtained from fossil fuels [2] (oil, coal and natural gas), while in the last fifty years the share of renewable resources (e.g. hydroelectric, solar and wind energy) remained quite constant, between 5 and 10%. The energy provided by nuclear power plants is a considerable fraction, of about 5%, but its share is stuck at the level of mid-80s, mainly because of the social impact of the nuclear accidents (Three Mile Island, Chernobyl and Fukushima).

Therefore, we can conclude that the present economy is sustained by the fossil fuels. This fact not only represents a big threat for the natural environment, due to the alteration of the atmospheric composition, but it is also evidently an unsustainable choice on the long-term. It was estimated that the annual global consumption of fossil fuels burns organic carbon that would require about 400 years of current annual biomass net primary productivity [4]. This is the reason why the global energy policies should be addressed to promote a rapid switch to renewable energy sources and, given the huge potential of solar radiation, discussed above, our star looks as the brightest solution.

1.2 From fossil fuels to a sun-powered world

The consumption, production and availability of fossil fuels are highly inhomogeneous on Earth. Due to the large difference in the density and volume of the economic activities between affluent and developing countries, the energy demand is unequally distributed in our world. A North American (U.S. and Canada) requires on average the same energy amount as two Europeans or Japaneses, as three Chinese, ten Indians or fifty Eritrean [5] (see Figure 1.2). Moreover, the fossil fuel production is geographically concentrated, with Russia, Middle-East and North America playing a dominant role [2], causing frequent geopolitical crisis.

On the other hand, solar energy is abundant and fairly distributed on our planet, constituting the base for life prosperous evolution. Since solar energy presently provides a very limited share of the primary energy sources (few percentage points), in the public opinion it is considered just as an option rather than the possible solution for the global energy demand. Nevertheless, a recent study of the Joint Research Center of the European Commission showed clearly the huge potential of solar power considering existing technology. In particular it was proven that in the theoretical hypothesis of satisfying the total electric energy demand of the European countries through photovoltaic (PV) panels with existing commercial efficiency (1 kW over 9.5 m^2, updated to 2007), the land area covered by buildings would be more than enough to provide the required production [6]. In fact, the percentage of built-up areas in the EU accounts for 1.3% of the total area, while only about 0.6% of land covering with PV panels with optimal exposure would be necessary to provide the whole electrical power consumed by Europeans. More surprisingly, the same result can be obtained on a national basis with the only exception of Sweden, as shown in Figure 1.3. Thus, solar power is a more abundant source compared to the common belief, and it can be an effective solution toward a sustainable energetic system even for Central Europe countries as graphically shown by Fig. 1.3 and 1.4. Of course, this is just a hypothetical reasoning and it is not required, and neither sensible
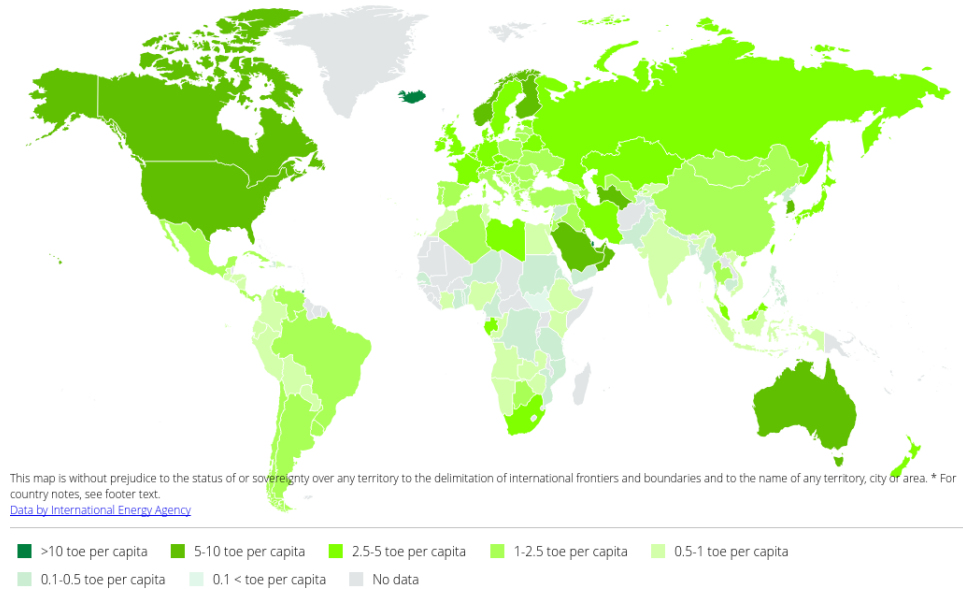
TPES/population (toe per capita) (2014)

This map is without prejudice to the status of or sovereignty over any territory to the delimitation of international frontiers and boundaries and to the name of any territory, city or area. * For country notes, see footer text.
Data by International Energy Agency

■ >10 toe per capita ■ 5-10 toe per capita ■ 2.5-5 toe per capita ■ 1-2.5 toe per capita ■ 0.5-1 toe per capita
■ 0.1-0.5 toe per capita ■ 0.1 < toe per capita ■ No data

Figure 1.2: Total primary energy sources (TPES) per capita by country (2014). Based on IEA data from [5] © OECD/IEA, 2016 www.iea.org/statistics, Licence: www.iea.org/t&c.

to base the whole electricity production on a single technology.

The previous discussion was just aimed to stress the fact that solar energy is an extremely abundant, democratic and easily accessible resource, which is not yet satisfactorily exploited. In the following, we would like to briefly discuss the possible strategies of solar energy, in the light of the strong and weak points of sunlight as an energy source.

The main drawbacks of solar energy technology are the quite poor power density of solar radiation and its intermittency. The average power density of solar radiation hitting the Earth's surface is of about 170 Wm^{-2}, that is the same order of magnitude of the power density required by human buildings [8]. As we already discussed, in order to use solar energy as the main energy source, we would need to deeply change the power generation system, with a significant portion of the built-up areas involved in solar power production. On the other hand, the intermittency of sunlight, due to the day–night cycle, raises the issue of energy storage. Basing the energy production on solar technology implies to adjust the production on demand, with the use of energy reservoirs such as batteries or artificial fuels.

Solar radiation at the Earth's surface has a wide spectrum, peaked in the visible region. As shown in Figure 1.5, it is mainly constituted by visible (VIS) and infrared (IR) radiation, with a rather small share of ultraviolet
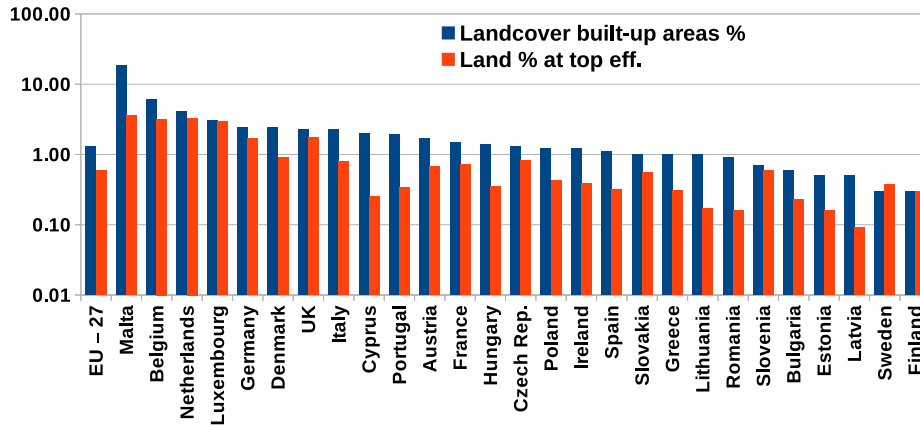
Figure 1.3: Percentage of built-up areas in EU countries [7] (blue) compared with the percentage area of PV panels that would be necessary to satisfy the whole electrical energy demand of EU countries [6] (red).
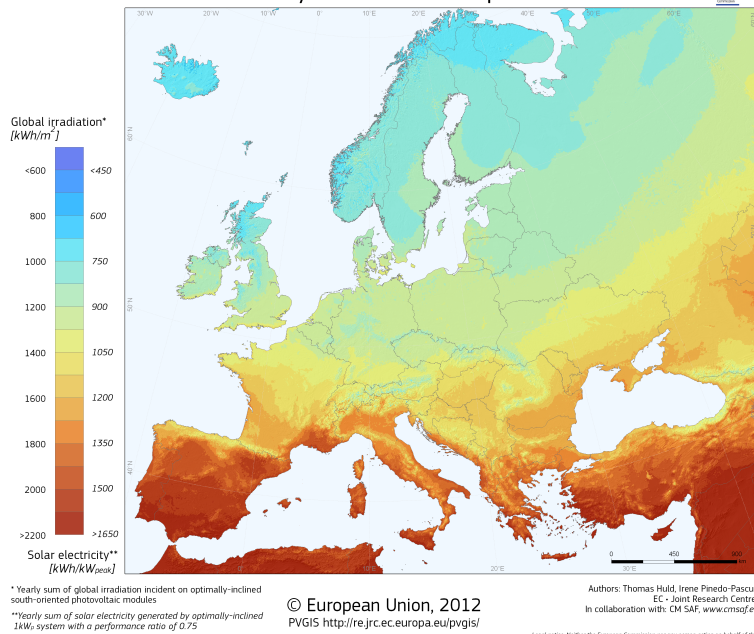

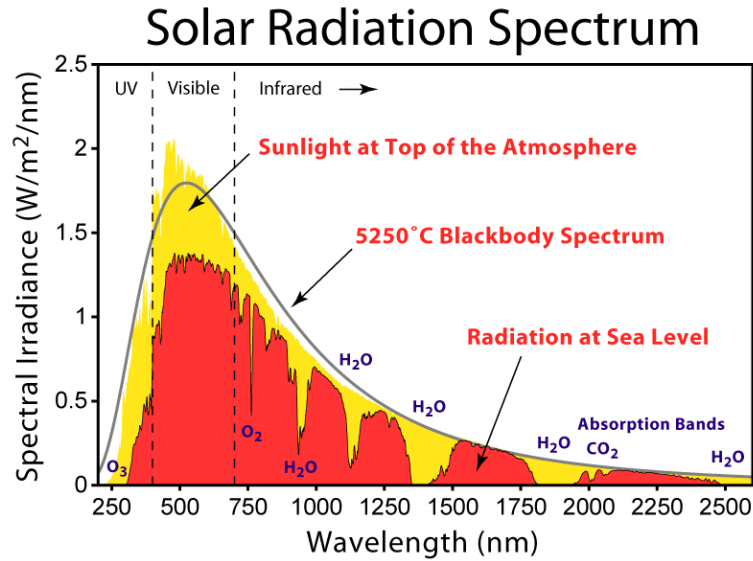Figure 1.4: Solar electricity potential of European regions [6].

Figure 1.5: Solar radiation spectrum for direct light at the top of the Earth's atmosphere (yellow area) and at sea level (red area) compared with the blackbody radiation spectrum from a 5250°C source. These curves are based on the standard published by the American Society for Testing and Materials (ASTM) [9] © ASTM, 2017.

(UV) radiation. There are several strategies to convert sunlight into forms of energy that are directly useful for human activities. In general, they include solar thermal technology, solar thermochemical conversion, photovoltaics and solar fuel technology.

Solar thermal conversion has the considerable advantage of exploiting non-concentrated IR solar radiation, through generally simple devices, such as solar thermal panels. This technology can be very helpful for several applications, such as heating, but also refrigeration and desalinization [10]. Solar water heating is a simple technology with a great potential, as proven by the 10% annual growth rate of the global installed capacity observed in the last decade [11]. This is seen as a strategical investment by some developing countries, such as China, Turkey, Brazil and India, but it is also helpful to EU countries to reach their green economy goals [12].

Solar thermal technology is not limited to small residential applications. On the contrary, there exist large solar thermal plants that use light concentration solutions to produce energy and, in many cases, electrical power. Depending on the land availability and on the specific needs, different solutions are adopted, such as parabolic-through solar concentrators, solar towers or dish-Stirling systems [13]. Of course, this technology is strongly dependent on the local insolation, and it particularly needs direct radiation exposure,

due to the directionality of the concentrating systems. Solar thermal electricity production is at present a cost effective technology, with optimal location plants providing energy at the competitive cost of 0.14 €kWh^{-1} [13]. More than 80% of the global electric power production through this technology is concentrated in Spain and United States. This, together with the limited total power production of 4.8 GW, tells us the great unexploited potential of this affordable technology [11].

Solar thermochemical conversion is a possible way to store solar energy in the form of fuels. As an example, a concentrated solar flux can be used to heat up a chemical reactor in which water is split into hydrogen and oxygen, thanks to the action of catalysts such as metal oxides. Alternatively, it is possible to reduce carbon dioxide to CO, which finds applications in the chemical industry. The technical constraints of this method of fuel synthesis, at the moment, keep it out from large-scale commercial application, mainly due to the big hurdles to obtain a competitive conversion efficiency [14].

On the other hand, photovoltaics is already a mature and commercial technology. The first commercial devices accessible to the private customers date to the mid-70s, when some large PV companies were founded in the United States and Japan [3]. From that time, the technological advances, the industrial scale effect, together with some geopolitical crisis, contributed to continuously accelerate the installation of PV systems. The global electric power produced through PV devices increased from 550 kW in 1977 to 9.3 MW in 1982, 100 MW in 1992, 2 GW in 2002 up to 227 GW in 2015 [11]. Now, the PV installed electrical power is mainly concentrated in China, Germany, Japan, United States, and Italy, but the cost reduction of this technology is leading to a more widespread market [11].

PV technology is historically based on crystalline silicon, which led to the first generation of PV panels. Single crystal silicon (sc-Si) solar cells were then replaced by less costly amorphous silicon (a-Si) thin film solar cells, with a higher absorbance that allows using thinner silicon layers and good module efficiency of about 6–10% [3]. More recently, the need to develop highly scalable PV devices posed new material requirements that necessitated finding some alternatives to silicon. Although silicon is an Earth-abundant element, the production of high purity, single crystal silicon slides has a high cost and material losses. Moreover, the competition with the electronics industry tends to maintain the high price of this material.

For this reason, the recent research on photovoltaics is focused on finding cheap, efficient alternatives, such as thin film solar cells and organic solar cells. Presently, cadmium telluride (CdTe) and copper indium gallium diselenide (CIGS) are leading materials in commercial thin film devices, with efficiency slightly higher than 10% [15]. It has been shown that CdTe production is less energy demanding than silicon manufacturing and that, even if it contains a toxic element as cadmium, over their production and life cycles, CdTe devices involve a cadmium release in the environment largely

lower than that produced by equivalent energy production from fossil fuels [16], without considering the other environmental effects of fossil fuels. Anyway, the issue of material scalability remains unsolved, and the replacement of rare elements like tellurium, indium or gallium is necessary in the close future.

On the other hand, organic solar cells (OSC) represent a promising future for PV materials. They could lead to a cheap technology that uses low energy intensive synthesis procedures. OSC technology is not yet ready for commercial production, because of the unsolved challenge of obtaining stable high performances. Anyway, the recent increasingly dynamic research in this area led to promising power efficiencies in the range 6.5–8.4% [17, 18].

Of course, in order to base the global energy production on sunlight as the main primary energy source, it will be necessary to tailor the solar energy conversion technology to the final uses in human activities. Thus, in view of a progressive energy transition, it will be needed to implement innovative approaches for the production of fuels. In other terms, there is the need to develop technologies for efficient solar to fuel conversion that can be provided to the existing network of fuel distribution and sale. This leads us to the last topic of this introduction chapter: the synthesis of solar fuels.

1.3 Solar fuel generation

More than a century ago, an Italian chemist, Giacomo Ciamician, predicted the possibility of producing fuels for human activities by applying controlled photochemical processes to mimic the natural photosynthesis, but with enhanced efficiency. Even in an age dominated by the optimism for the progress of human society, Ciamician was aware of the risks of basing our economy on the "relatively small reserves of coal that the past geological epoch have stored for us" [19]. He suggested solar fuel production as a possible way to meet the global energy demand:

> Yet the true solution consists in utilizing the radiations that pass through the entire atmosphere and reach the surface of the Earth in large amounts. [...] By using suitable catalyzers, it should be possible to transform the mixture of water and carbon dioxide into oxygen and methane, or to cause other endo-energetic processes. [19]

The fossil fuels that currently sustain the global energy demand were produced during the past geological times through natural photosynthesis [20]. Nevertheless, this natural photochemical process is not a good candidate for producing solar fuels, at least because of its low efficiency. The

average solar to chemical energy efficiency of natural photosynthesis was estimated to be less than 0.5% on a yearly basis [3], so that using biomass to produce artificial fuels would result in an unsustainable land consumption. For this reason, the energy policies that excessively stimulate biofuel production were criticized in the recent past [21].

Solar fuel production in photoelectrochemical cells (PECs) is one of the most promising routes to achieve efficient artificial photosynthesis. In particular, in the following, we will describe PEC technology based on sunlight absorbing semiconductors coupled with catalytic materials that allow efficient electrochemical reactions at the electrode–electrolyte interface. This approach takes advantage of the well sedimented knowledge in the fundamental and applied research on semiconductor thin films, which resulted in large-scale industrial applications, such as electronics and photovoltaic materials.

PEC technology can be adapted to the production of different solar fuels, such as hydrogen, methane or methanol. As in the Ciamician's intuition, to drive a specific electrochemical process, a central role is played by the choice of the catalyst material, which has to enhance the kinetics of the desired redox processes at the electrode–electrolyte interface.

The idea of using the water splitting process to produce hydrogen as a clean fuel was prophetically anticipated by the French novelist Jules Verne who wrote about hydrogen as an ideal energy source in *The Mysterious Island*, published in 1874:

> Yes, but water decomposed into its primitive elements [...] by electricity, which will then have become a powerful and manageable force, for all great discoveries, by some inexplicable laws, appear to agree and become complete at the same time. Yes, my friends, I believe that water will one day be employed as fuel, that hydrogen and oxygen which constitute it, used singly or together, will furnish an inexhaustible source of heat and light, of an intensity of which coal is not capable. [22]

Actually, hydrogen cannot be considered as an energy source, since it is not present in Earth's atmosphere, neither can be directly extracted in some form. Rather, it is an energy carrier, which can be used to provide energy to the final users or to store energy when required. In the past decades, hydrogen has been proposed as a possible fuel for vehicles, as a storage medium for electricity interconversion and also as an energy carrier embedded in a revolutionary electric grid [23], in the perspective of a future energy delivery system that became popular as the "hydrogen economy" [24].

The main issues regarding the use of hydrogen for energy purposes are its production through a clean and efficient technology, its safe and convenient storage and, finally, the risks related to its usage. The global hydrogen

production is dominated by fossil fuel based technologies: the most part of current hydrogen production is obtained from natural gas using steam methane reforming, while a minor share also comes from refinery off-gases and from coal gasification, while electrolysis is used only for niche applications [25, 26]. Presently, hydrogen is not used as an energy carrier: it is almost entirely used within the refining and chemical industries [5].

The main issue of hydrogen as a fuel consists in its low density. Hydrogen has a good energy density by weight ($33.3\ \mathrm{Whkg^{-1}}$), but a low energy density by volume ($2.5\ \mathrm{Whl^{-1}}$ in liquid form). Even in liquid phase, one liter of hydrogen contains less hydrogen mass than one liter of gasoline (about 71 g of H_2 in hydrogen, compared to 110 g in gasoline). Moreover, hydrogen has a low boiling point (20 K), requiring cryogenic technology and high energy losses to be achieved [3]. Anyway, hydrogen as a fuel for vehicles presents a high tank-to-wheel efficiency, relying on fuel cell technology combined with electrical engine, which have a significantly higher efficiency compared to internal combustion engine.

The primary hazard related to the use of hydrogen is its flammability in air, together with the difficulty to detect its leaks and flames, since hydrogen is colorless and odorless, while, when ignited in air, it releases most of its energy in the UV region [24].

On the other hand, hydrogen is a perfectly clean fuel, since its combustion only releases water steam, so that it would be a good candidate for a decarbonized economy. Its main strong point is the possibility of use it efficiently in electricity interconversion systems, since water electrolyzers have typical efficiency of 65–82%, while co-generation systems based on fuel cells have an energy efficiency up to 95% [27]. The open challenges related to hydrogen technology are mainly its production through carbon-free, cheap and scalable technology and the problem of an effective storage technology.

To date, it has not yet been proven the viability of a "hydrogen economy" and probably, due to the competitiveness of other energy storage media as batteries or other artificial fuels, a more realistic future for the energy delivery system will be a combined strategy, in which different solutions will be adopted depending on the specific application.

Another promising route for artificial photosynthesis comes from the conversion of carbon dioxide and water into fuels and chemicals. CO_2 is well known as a greenhouse gas and its concentration in the atmosphere has increased of about 20% in the last 50 years [28]. The role of human activities on the greenhouse gases increase has been worldwide recognized, since in the recent Paris Agreement approved by the United Nations Framework Convention on Climate Change it was noted that "much greater emission reduction efforts will be required than those associated with the intended nationally determined contributions in order to hold the increase in the global average temperature to below 2°C above pre-industrial levels by reducing emissions to 40 gigatonnes" [29].

Fuel	Reaction	n	E_{rev}^0 (V)
Hydrogen	$2H_2O \rightarrow 2H_2 + O_2$	4	1.23
Carbon monoxide	$2CO_2 \rightarrow 2CO + O_2$	4	1.34
Methane	$CO_2 + 2H_2O \rightarrow CH_4 + 2O_2$	8	1.06
Methanol	$2CO_2 + 4H_2O \rightarrow 2CH_3OH + 3O_2$	12	1.21
Formic acid	$2CO_2 + 2H_2O \rightarrow 2HCOOH + O_2$	4	1.48

Table 1.1: Overall reactions of water splitting and CO_2 conversion. The number of electrons involved in the process n and the theoretical reversible cell potentials E_{rev}^0 are indicated.

CO_2 conversion using clean technology could be an effective strategy to comply with the constraints of the recent climate agreements. Actually, CO_2 emissions are more concentrated than the common belief: it was shown that about 60% of the carbon dioxide emission comes from 8000 large industrial plants [30]. This tells us that finding a suitable strategy to convert highly concentrated CO_2 in industrial byproduct gases would allow to radically change the carbon footprint of our economy.

In the last few decades, there has been a growing research interest in the photochemical and photoelectrochemical reduction of CO_2. Indeed, it is possible to produce fuels like methane or methanol, or carbon monoxide as a combustion additive and also chemicals as formic acid in solar photo-electrochemical cells using carbon monoxide and water [31–33]. Moreover, there is an active research field in the development of fuel cells directly using these CO_2-derived substances, to efficiently generate electricity [34–36].

Of course, the complex redox reactions that allow CO_2 conversion result in kinetics limits, requiring suitable catalysts and device design to achieve high efficiency processes. The overall reactions involved in CO_2 conversion are summarized in Table 1.1. At present, the multiple electron and proton transfers necessary to produce more useful products such as methane or methanol have only been demonstrated with low efficiency.

Carbon dioxide has been shown to be reduced directly on metal surfaces [37], but the development of stable, efficient, low cost catalytic materials for CO_2 reduction is still a big open challenge. On the other hand, this research field has a great potential, since it could lead to liquid fuels to be used as energy carriers, overcoming the energy storage issue.

References for Chapter 1

[1] P. J. Crutzen. "Geology of mankind". In: *Nature* 415 (2002), p. 23. DOI: 10.1038/415023a.

12

[2]   British Petroleum. *BP Statistical Review of World Energy.* London: British Petroleum, 2016.

[3]   N. Armaroli and V. Balzani. *Energy for a sustainable world: From the oil age to a sun-powered future.* John Wiley & Sons, 2010.

[4]   J. S. Dukes. "Burning Buried Sunshine: Human Consumption of Ancient Solar Energy". In: *Climatic Change* 61 (2003), pp. 31–44. DOI: 10.1023/A:1026391317686.

[5]   IEA Statistics. *Key World Energy Statistics.* International Energy Agency, 2016.

[6]   M. Súri et al. "Potential of solar electricity generation in the European Union member states and candidate countries". In: *Solar Energy* 81 (2007), pp. 1295–1305. DOI: 10.1016/j.solener.2006.12.007.

[7]   Eurostat. *Land covered by artificial surfaces.* 2012.

[8]   V. Smil. *Energy at the crossroads. Global perspectives and uncertainties.* MIT Press, 2003.

[9]   ASTM Standard. "G173–03, Standard Tables for Reference Solar Spectral Irradiances: Direct Normal and Hemispherical on 37° Tilted Surface". In: *ASTM International, West Conshohocken, PA* (2012). DOI: 10.1520/G0173-03R12.

[10] S. A. Kalogirou. "Solar thermal collectors and applications". In: *Prog. Energy Combust. Sci.* 30 (2004), pp. 231–295. DOI: 10.1016/j.pecs.2004.02.001.

[11] REN 21. "Renewables 2016 global status report". In: *Renewable Energy Policy Network for the 21st Century* (2016).

[12] ESTIF. "Solar Thermal Markets in Europe. Trends and Market Statistics". In: *European Solar Thermal Industry Federation* (2016).

[13] R. Pitz-Paal. "How the Sun gets into the Power Plant". In: *Renewable Energy.* Ed. by R. Wengenmayr and a. Bührke. Wiley-VCH Verlag GmbH & Co. KGaA, 2012, pp. 28–35. DOI: 10.1002/9783527671342.ch4.

[14] R. S. Service. "Solar fuels. Sunlight in your tank". In: *Science* 326 (2009), pp. 1472–1475. DOI: 10.1126/science.326.5959.1472.

[15] D. Butler. "Thin films: Ready for their close-up?" In: *Nature* 454 (2008), pp. 558–559. DOI: 10.1038/454558a.

[16] V. Fthenakis, H. C. Kim, and E. Alsema. "Emissions from Photovoltaic Life Cycles". In: *Environ. Sci. Technol.* 42 (2008), pp. 2168–2174. DOI: 10.1021/es071763q.

[17] T. Ameri et al. "Organic tandem solar cells: A review". In: *Energy Environ. Sci.* 2 (2009), pp. 347–363. DOI: 10.1039/b817952b.

[18] K. Cnops et al. "8.4% Efficient fullerene-free organic solar cells exploiting long-range exciton energy transfer". In: *Nature Communications* 5 (2014), p. 3406. DOI: 10.1038/ncomms4406.

[19] G. Ciamician. "The Photochemistry of the Future". In: *Science* 36.926 (1912), pp. 385–394. DOI: 10.1126/science.36.926.385.

[20] V. Smil. *Oil A Beginner's Guide.* Oneworld Publications, 2008.

[21] A. Regalado. "Race for Cellulosic Fuels Spurs Brazilian Research Program". In: *Science* 327 (2010), pp. 928–929. DOI: 10.1126/science.327.5968.928.

[22] J. Verne. *The Mysterious Island.* August 24, 2008 [EBook no.1268]. Project Gutenberg, 1874.

[23] P. M. Grant, C. Starr, and T. J. Overbye. "A Power Grid for the Hydrogen Economy". In: *Scientific American* 295 (2006), pp. 76–83. DOI: 10.1038/scientificamerican0706-76.

[24] K. Rajeshwar et al. "Renewable Energy and the Hydrogen Economy". In: *Solar Hydrogen Generation: Toward a Renewable Energy Future.* Ed. by K. Rajeshwar, R. McConnell, and S. Licht. Springer, 2008.

[25] IEA OECD et al. *Energy and Air Pollution–World Energy Outlook 2016 Special Report.* International Energy Agency, Paris, France, 2016.

[26] IEA Essentials. *Hydrogen Production & Distribution.* Tech. rep. International Energy Agency, 2007.

[27] Alexander Körner et al. "Technology Roadmap Hydrogen and Fuel Cells". In: *International Energy Agency (IEA)* (2015).

[28] R. F. Keeling. "Recording Earth's Vital Signs". In: *Science* 319 (2008), pp. 1771–1772. DOI: 10.1126/science.1156761.

[29] Change FCoC UNFCCC. "Adoption of the Paris Agreement". In: *Proposal by the President (Draft Decision), United Nations Office, Geneva (Switzerland)* (2015).

[30] B. Hileman and J. Johnson. "Driving CO_2 underground". In: *Chem. Eng. News* 85.39 (2007), pp. 74–81.

[31] B. Kumar et al. "Photochemical and Photoelectrochemical Reduction of CO_2". In: *Annu. Rev. Phys. Chem.* 63 (2012), pp. 541–569. DOI: 10.1146/annurev-physchem-032511-143759.

[32] Q. Shen et al. "High-yield and Selective Photoelectrocatalytic Reduction of CO_2 to Formate by Metallic Copper Decorated Co_3O_4 Nanotube Arrays". In: *Environ. Sci. Technol.* 49 (2015), pp. 5828–5835. DOI: 10.1021/acs.est.5b00066.

[33] D. H. Won et al. "Photoelectrochemical production of formic acid and methanol from carbon dioxide on metal-decorated CuO/Cu_2O-layered thin films under visible light irradiation". In: *Appl. Catal., B* 158–159 (2014), pp. 217–223. DOI: 10.1016/j.apcatb.2014.04.021.

[34] G. A. Olah, A. Goeppert, and G. K. S. Prakash. *Beyond Oil and Gas: The Methanol Economy.* John Wiley & Sons, 2011.

[35] C. Rice et al. "Direct formic acid fuel cells". In: *J. Power Sources* 111 (2002), pp. 83–89. DOI: 10.1016/S0378-7753(02)00271-9.

[36] E. P. Murray, T. Tsai, and S. A. Barnett. "A direct-methane fuel cell with a ceria-based anode". In: *Nature* 400 (1999), pp. 649 –651. DOI: 10.1038/23220.

[37] P. Kedzierzawski and J. Augustynski. "Poisoning and Activation of the Gold Cathode during Electroreduction of CO_2". In: *J. Electrochem. Soc.* 141 (1994), pp. L58–L60. DOI: 10.1149/1.2054936.

Chapter 2

Photoelectrochemical water splitting

2.1 Introduction

In Chapter 1 we gave some motivations of the research in the field of solar fuel generation, toward a sustainable economy. In the present chapter, we will introduce the principles of photoelectrochemical fuel synthesis, one of the most promising routes to achieve high efficiency in the conversion of solar radiation to artificial fuels.

The photoelectrochemical route to artificial photosynthesis requires the design of scalable, efficient photoelectrochemical cells (PECs) suitable for industrial production. A PEC is an integrated system consisting of two electrodes (anode and cathode) capable of photo-generation of electric charges, driving them to the electrode surface, which is in contact with an electrolyte solution. At the electrode–electrolyte interface, redox reactions take place, while the electrolyte ions allow the charge transfer through the solution.

A successful strategy in the design of PECs is to decouple the role of solar light absorption and that of promoting the interfacial charge transfer. Thus, the research efforts are addressed to develop suitable photoactive materials that fulfill the thermodynamic requirements related to the redox processes of interest. Then, these materials can be functionalized with selective catalysts to improve the reaction kinetics at the electrode–electrolyte interface.

Semiconductor thin films are good candidates as solar absorbers in PECs. The knowledge of the fundamentals of optoelectronics, together with the industrial technology available in this field, represent a strong point toward the future commercialization of semiconductor-based PECs.

In the following sections, we will introduce the role of semiconductors in photoelectrochemistry, some possible PEC configurations and the state of the art in this research area.

2.2   Semiconductors in photoelectrochemistry

Semiconductors in photoelectrodes have the primary role of generating electron/hole (e^-/h^+) pairs though photo-excitation and to separate the opposite charges, avoiding recombination, so that they can be exploited in the electrochemical reactions at the electrode–electrolyte interface. This process presents deep analogies with the photocurrent generation in a photodiode, which is used in solar cells. It is interesting to discuss the solid-state p–n junction, which is more familiar to physicists, to introduce the more complicated topic of junctions in electrochemistry.

Solid-state junctions   A p–n junction can be obtained by coupling two regions of the same semiconductor, doped with different materials: doping with electron donors results in n-type semiconductors, while acceptors yield p-type behavior. The n-type semiconductor has an excess of free electrons and its Fermi level lies close to the conduction band. Conversely, a p-type semiconductor has an excess of holes and its Fermi level is close to the valence band.

When the junction is formed, the Fermi level has to equilibrate across the interface, resulting in the phenomenon of band bending. In other words, free electrons from the n-side migrate to the p-side, combining with the free holes. A depletion region, or space-charge region (SCR) forms across the junction, where the n-side results positively charged (electron depleted) and the p-side is negatively charged (electron enriched). In this way, a built-in electric field is formed, as an equilibrium condition of the free charge carrier distribution [1].

In a solid-state p–n junction, the built-in electric field is the mechanism that allows charge separation under illumination: the effect at the base of PV cells. The e^-/h^+ pairs generated through photoexcitation within the SCR, whose depth is generally of the order of one micron, are accelerated: the electrons toward the n-side and the holes to the p-side. In this way, under illumination a photocurrent can be obtained. The charges generated outside the SCR cannot be efficiently separated by the built-in electric field: they can migrate on a typical spatial scale fixed by the mean free path but they tend to recombine. In addition, impurities and defects in the semiconductor crystal lattice favor recombination and limit photovoltaic performance.

The electric potential difference measured across the p–n junction in open-circuit conditions is called V_{oc} (open-circuit potential) and it is limited by the built-in potential of the junction. In turn, the built-in potential is strictly limited by the semiconductor energy gap, since the Fermi level of both the n-type and p-type semiconductors lays inside the bandgap.

Under illumination, thermal equilibrium at the junction is perturbed, and a single Fermi level cannot be defined. Under non-equilibrium conditions, the statistics of electron and hole populations can be described within
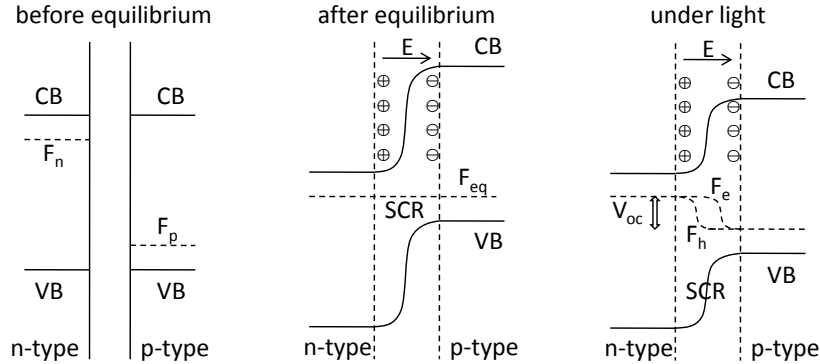
Figure 2.1: Formation of the p–n solid-state rectifying junction showing: (left) materials before contact; (center) band diagram of the p–n junction in equilibrium; (right) band diagram of the p–n junction under illumination, illustrating the development of usable photopotential (V_{oc}) through quasi-Fermi level separation. F_n, F_p and F_{eq} represent Fermi levels in the isolated n and p regions, and in equilibrium after contact, respectively. F_e and F_h indicate the quasi-Fermi level for electrons and holes, respectively. The arrow on the top indicates the direction of the built-in electric field.

the formalism of quasi-Fermi analysis. Within this framework, the open-circuit potential V_{oc}, represented by the Fermi level offset between the two bulk regions, is determined by the quasi-Fermi level separation in the device [2].

The real open circuit potential, V_{oc} represents the electric potential that is extracted from a solar cell, which is usually of about 50–75% of the semiconductor energy gap. As an example, single-junction silicon solar cells have typical V_{oc} of 0.6–0.7 V, while silicon bandgap is 1.1 eV.

In semiconductor photovoltaics, in order to obtain high output voltage, wide bandgap materials should be used. On the other hand, this poses the problem of solar spectrum harvesting, since a wide bandgap wastes a large fraction of the solar irradiance.

Semiconductor–liquid contacts The analogue of the p–n junction in the case of a semiconductor-based photoelectrochemical device is the contact between the semiconductor photoelectrode and the electrolyte solution. When a semiconductor is immersed in a liquid containing a redox couple, its Fermi level equilibrates with the electrochemical potential of the electrolyte. Charge transfer across the electrode–electrolyte interface occurs through reduction or oxidation processes: in the case of electrochemical water splitting, water reduction and oxidation occur.

As described for the p–n junction, the equilibration of the Fermi level requires charge transfer, so that, at equilibrium, an interfacial electric field is established. The space charge region is formed at the electrode surface, with a typical width of microns, while the electrolyte develops the double-layer structure at the nanoscale [3].

In the case of n-type semiconductor as a photoanodic material, the redox couple of interest is O_2/H_2O and water oxidation is expected to occur. On the other hand, p-type semiconductors can be used as photocatodic materials, where water reduction is promoted, involving the redox couple H^+/H_2 [2].

In order to obtain a properly oriented built-in electric field, which is useful to drive the photogenerated charges, the band edges of the semiconductor have to fulfill some requirements. On the anodic side, the n-type semiconductor has to drive holes to the solution. Holes in the valence band of the photoanode semiconductor need to have excess energy compared to the redox standard potential $E^0\left(O_2/H_2O\right) = 1.23$ V, so that the valence band edge has to be more positive. Conversely, when a p-type semiconductor is used as a photocathode material, its conduction band edge has to be more negative than the electrochemical potential $E^0\left(H^+/H_2\right) = 0$ V.

If a single semiconductor was used to drive the whole photoelectrochemical water splitting process, both the above conditions should be satisfied, thus its bandgap should be larger than the difference between the two electron energies corresponding to the two redox couples: $E_g > 1.23$ eV.

This condition, in real systems, is necessary, but not sufficient. As discussed above for the p–n junction, under illumination the system is no more in an equilibrium condition. When the semiconductor–liquid interface is illuminated and a photocurrent is produced, the energetics of charge carriers reaches a photostationary state, and the free energy that is produced is always lower than the unperturbed barrier height.

In the case of an n-type photoanode for water splitting, the maximum internal energy that can be extracted from the photogenerated e^-/h^+ pairs would be the difference between the conduction band edge E_c and the electrochemical potential of water oxidation $-qE\left(O_2/H_2O\right)$, that is the barrier height $q\Phi_b$ indicated in Fig. 2.2. On the other hand, the free energy associated to the photogenerated couples is given by the difference between the hole and electron quasi-Fermi levels under illumination [2].

This energy difference is directly linked to the open-circuit voltage (V_{oc}), defined as the energy splitting between the electron and hole quasi-Fermi levels under no net current flow [4]. The real photovoltage generated by the semiconductor–liquid junction under illumination determines the electrochemical reactions that can be driven by the photoelectrode. Finally, the correct requirement in the case of photoelectrochemical water splitting driven by a single semiconductor is that the photovoltage exceeds 1.23 V, with correct matching between band edge positions and the electrochemical
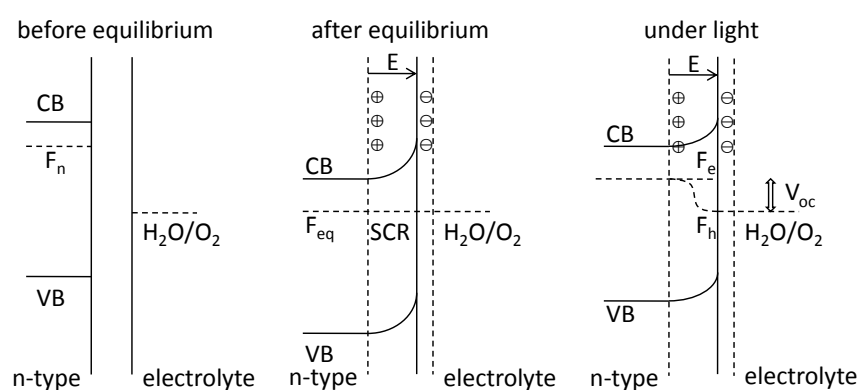
Figure 2.2: Formation of a semiconductor/electrolyte junction in the case of a n-type photoanode, showing: (left) semiconductor and electrolyte before contact; (center) band diagram of the junction in equilibrium; (right) band diagram of the junction under illumination, illustrating the development of sufficient photopotential (i.e., quasi-Fermi level split) to drive the water splitting process. The accumulation of positive charge in the semiconductor is schematically indicated, and the thin double-layer structure (Helmholtz layer) on the electrolyte side of the junction is represented by the negative charges. F_{eq} represents Fermi level in equilibrium after contact, while F_e and F_h indicate the quasi-Fermi level for electrons and holes, respectively. The arrow on the top indicates the direction of the built-in electric field.

potentials of water splitting half-reactions.

Fundamental processes in PECs for water splitting As a conclusion of the discussion about semiconductors in PECs for water splitting, we summarize the main steps that lead to hydrogen and oxygen evolution on the electrodes. The optimization of these steps poses various requirements that have to be considered in the choice of materials and configurations for photoanodes. In particular, here we focus on a single-junction photoelectrode system.

1. **Photon absorption and charge generation.** e^-/h^+ pairs are generated through photoexcitation. In the case of a single-junction device, photons with energy lower than the bandgap cannot be absorbed. On the other hand, photons with energy higher than the bandgap can be absorbed, but the energy exceeding the energy gap is wasted through thermal dissipation. High bandgap semiconductors only absorb a small fraction of the wavelengths in the solar spectrum, while small bandgap materials generally suffer from low conversion efficiency due to high thermalization losses.

2. **Charge separation and transport.** The photogenerated charge carriers must be spatially separated, avoiding recombination. The SCR is the active region of the photoanode, since the couples generated inside it can be separated. The diffusion length of electrons and holes need to be considered in the design of the photoactive layer, so that the photogenerated charges can reach the electrolyte or the back contact. The charge transport is limited by defects and impurities in the crystal lattice.

3. **Charge extraction and electrochemical product formation.** Electrons and holes that reach the photoelectrode–electrolyte interface can be transfered to the electrolyte solution, driving the water splitting redox reaction. This process requires a correct band edge alignment with the electrochemical potential of the half reaction to be driven: water oxidation on the anode and water reduction on the cathode. Moreover, parasitic or corrosion reactions competing with the water splitting reactions can result in substantial loss. A possible solution to selectively favor the desired electrochemical process is to couple the photoactive semiconductor with a suitable catalyst. In order to avoid high surface recombination, the texture of crystalline materials and the surface nanostructuring have to be engineered.

4. **Electrochemical product management.** The products of the re-
dox processes (hydrogen and oxygen gas bubbles) must be removed
from the electrode surface in order to favor efficient mass transport
and to avoid adverse optical effects. Depending on the device design,
a gas-separating membrane may be required. The cell design is criti-
cal to optimize the product collection without introducing significant
losses. In particular, the choice of the electrolyte solution and eventual
additives, photoelectrode geometry and counter electrode proximity
are the main parameters that can be arranged.

2.3 Defining the photoelectrochemical cell efficiency

The performance of PECs can be evaluated as the efficiency in converting
the incoming irradiation into chemical products. In the case of solar water
splitting PECs, this concept is named solar-to-hydrogen (STH) efficiency
[5],

$$\eta_{STH} = \frac{P_{electrical}^{out} - P_{electrical}^{in}}{P_{light}} = \frac{j_{photo}\left(V_{redox} - V_{bias}\right)}{P_{light}},\qquad(2.1)$$

where P_{light} is the input solar power, j_{photo} is the working point photocur-
rent, while V_{redox} is usually taken as 1.23 V, that is the Gibbs free energy
change for water splitting ($G_{f,H_2}^0 = 237$ kJ/mol) converted into potential
units. Equation (2.1) is written in the general form of photoassisted PECs,
since V_{bias} is the potential difference externally applied between the two
electrodes. Of course, a true solar-to-hydrogen system has only sunlight
and water as inputs, so that $V_{bias} = 0$ V.

Assuming input solar irradiation at AM1.5G (100 mW/cm^2) and short-
circuit conditions ($V_{bias} = 0$ V), a photocurrent of 8 mA/cm^2 is required to
obtain $\eta_{STH} = 10\%$, which is typically indicated as an efficiency target for
economically viable PECs [6].

The STH efficiency can be expressed more directly on the base of the
amount of the evolved hydrogen, which can be experimentally measured
through mass spectroscopy or gas chromatography [7]:

$$\eta_{STH} = \frac{\Phi_{H_2} G_{f,H_2}^0}{P_{light}},\qquad(2.2)$$

where Φ_{H_2} is the hydrogen production rate, expressed in mol/m^{2}s, while
$G_{f,H_2}^0 = 2.37 \times 10^5$ J/mol and $P_{light} = 1000$ W/m^2 in the standard condi-
tions.

Of course, in the experimental assessment of photoelectrode and PEC
performance, the experimental setup plays an important role. For practical
needs, artificial light is almost always used, and thus a proper solar light

simulator is needed to reproduce the solar spectrum (see Fig. 1.5). In general, AM1.5G spectrum is used, since it reproduces the effect of atmospheric light attenuation at mid-latitudes.

Then, in the photoelectrochemical measurements, the absence of competing reactions should be proved, so that the observed current can be attributed to water splitting. Moreover, a heat dissipation system is usually required, so that the temperature of the PEC can be kept constant during the measurements.

More detailed information about the spectral response of the photoelectrodes is usually expressed as the incident photon-to-current efficiency (IPCE), which is the fraction of photons of a given wavelength that generated a photocurrent response. This quantity can be experimentally evaluated through illumination of the photoelectrode with a monochromatic source (of wavelength λ), of power density $P(\lambda)$:

$$\text{IPCE}(\lambda) = \frac{hc}{e}\left(\frac{j_{\text{photo}}(\lambda)}{\lambda P(\lambda)}\right). \tag{2.3}$$

An estimation of the intrinsic quantum efficiency of a photoelectrode material can be expressed as the absorbed photon-to-current efficiency (APCE), considering the absorbed radiation only:

$$\text{APCE}(\lambda) = \frac{\text{IPCE}(\lambda)}{A(\lambda)} = \frac{\text{IPCE}(\lambda)}{1 - R(\lambda) - T(\lambda)}, \tag{2.4}$$

where A, R and T represent the optical absorption, reflection and transmission, respectively. IPCE and APCE experimental measurements of iron oxide based photoanodes are reported in Chapter 7 (see also [8]).

In Chapter 1, we already mentioned electrochemical production as one of the present commercial technologies for hydrogen synthesis. Since the development of water splitting catalysts for electrolyzers, with some adaptations, can find applications also in the photoelectrochemical devices, here we introduce the concept of current-to-hydrogen conversion efficiency. In the case of electrocatalytic water splitting by using an externally applied bias, the system efficiency can be expressed as:

$$\eta_{\text{LHV}} = \frac{P_{\text{out}}}{P_{\text{in}}} = \frac{V_{\text{redox}}}{V_{\text{bias}}}, \tag{2.5}$$

named lower heating value (LHV) efficiency. In particular, using the LHV corresponds to considering the Gibbs free energy change as discussed above, so that $V_{\text{redox}} = 1.23$ V for water splitting. The bias potential exceeding V_{redox} constitutes the total overpotential at a given working current density. A nonzero overpotential is unavoidable for thermodynamic and kinetic reasons, but it has to be minimized in order to obtain high hydrogen production efficiency. This crucial topic will be addressed more in depth in the next paragraph.

Of course, the discussion presented here about the efficiency of photoelectrochemical and electrochemical hydrogen production can be easily adapted to the synthesis of different artificial fuels, by choosing the correct quantities related to the molecule of interest (such as V_{redox} and G_f^0).

Overpotentials In electrochemical processes, overpotential can be simply defined as the excess electric potential, compared to the electrochemical potential of the process of interest, to be applied to an electrode in order to obtain a desired current. The need of this excess potential limits the efficiency of photoelectrochemical or electrochemical processes, as it is clear from Eqs. (2.1) and (2.5). The origin of this phenomenon involves different mechanisms, of thermodynamic and kinetic nature.

1. **Activation overpotential.** The chemical equilibrium is a state in which the rates of the forward and backward reactions are balanced, a state also known as dynamic equilibrium. In open-circuit conditions, when an electrode is immersed in an electrolyte, in equilibrium no net current flows through the solid–liquid interface, but the reduction and oxidation reactions occur with equal and opposite rate. The two balanced dynamic currents are a fundamental characteristic of the electrode and are named exchange currents. The exchange current density is related to the ability of the electrode to exchange charge carriers. Interestingly, the activation energy barrier to the reduction or oxidation reactions is due to the charge transfer between the electronic and the ionic carriers, so that a large exchange current results in a low activation energy [3].

   The anode or cathode activation overpotentials (η_A and η_C, respectively) are related to the electrode exchange current. Since the cathode exchange current density is typically some orders of magnitude greater than the anode exchange current density, the activation overpotential is dominated by η_A [9].

2. **Ohmic losses.** When current increases, the resistance of the electrode material to the electronic current and the resistance of the electrolyte to the ionic current contribute to increase the overpotential with respect to the theoretical activation energy [10]. The relevance of ohmic losses depends on the working current density and, obviously, on the electrolyte used and cell geometry. The resistivity of electrical connections of the cell also lead to an overpotential increase.

2.4 Photoanodes and photocathodes for solar water splitting

In § 2.2 we referred to a simple cell configuration that employs a single semiconductor material to drive the water splitting process. Indeed, a simple solar water splitting device could be obtained, for example, by coupling a proper n-type photoanode with a metal counter electrode. Nevertheless, in the view of developing economically viable, efficient devices for the global energy market, it is of crucial importance to meet all the requirements posed by the complex physical chemistry of the photoelectrochemical water splitting process described above. For this reason, here we briefly present some possible PEC configurations that are commonly adopted in solar water splitting prototypes.

The simplest PEC configurations are obtained through a single semiconductor/liquid junction as illustrated in Figures 2.3(a) and 2.3(b). Photoanode-based unassisted water splitting has been proved with n-type semiconductors as $SrTiO_3$ and $KTaO_3$ [4], but with insufficient STH efficiency of about 1% [11]. Several p-type semiconductor materials were studied to build single bandgap photocathodes coupled with metal counter electrodes. Promising η_{STH} values of about 10% were obtained by employing rare and precious metals, such as InP semiconductor functionalized with rhodium or rhenium based catalysts [12]. On the other hand, by using scalable materials, as Cu_2O or SiC, stable and high performances are still not reached [5, 13].

Figure 2.3(c) shows a photoanode biased with a PV layer, coupled with a metallic cathode. This solution, or the analogous configuration based on a photocathode, presents a double advantage. Firstly, it allows using cheap semiconductors with relatively small bandgap or that with non-optimal band edge alignment, by biasing them with a proper PV material. Secondly, by coupling two junctions with a different spectral response, it is possible to optimize the solar spectrum harvesting. Usually, a semiconductor thin film, like a low-cost and stable metal oxide, is deposited onto a thicker PV layer, which has a smaller band gap. In this way, when the PV–photoelectrode is illuminated from the front side, the semiconductor layer absorbs in the blue–UV range, while transmits the red–NIR wavelengths toward the PV layer.

PV–photoanode PECs were tested for solar hydrogen generation. One of the earlier attempts was carried out by depositing TiO_2 on top of a p–n junction Si PV cell [14]. More recently, a similar solution was proposed by Grätzel, by depositing photoanodic materials as WO_3 or Fe_2O_3 on dye-sensitized solar cells (DSSCs) [15, 16]. In this configuration, the DSSC plays the role of the p–n junction reported in Fig. 2.3(c). An even simpler but effective solution was that of depositing a stable, efficient water oxidation catalyst (WOC) as $NiFe_yO_x$ on triple junction a-Si PV cells. This solu-
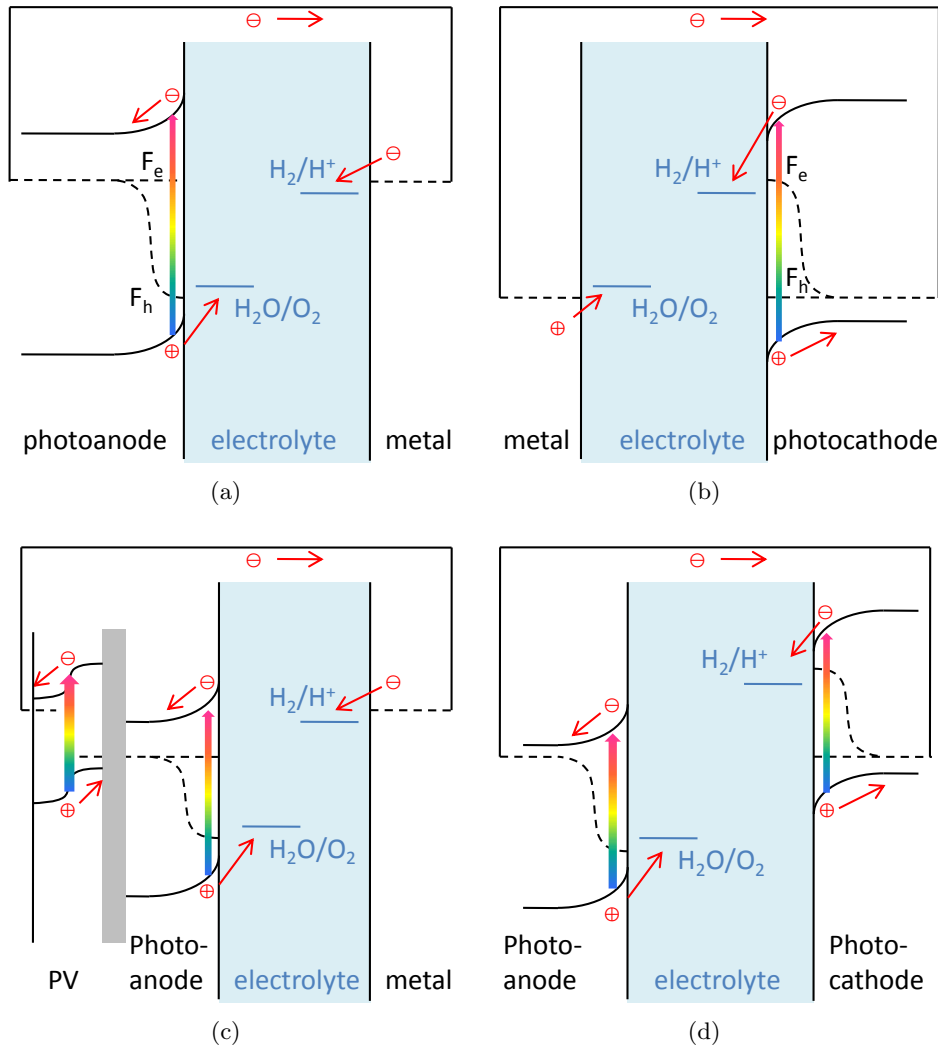
Figure 2.3: Examples of possible PEC configurations under illumination. (a) Standard single semiconductor device based on a n-type photoanode with a metal counter electrode; (b) p-type photocathode with metal counter anode; (c) monolithic device based on a photoanode biased with an integrated p–n junction (photovoltaic material); (d) Tandem cell obtained with a n-type photoanode and a p-type photocathode.

tion, together with a CoMo hydrogen evolution catalyst, resulted in a STH efficiency of 7.5% [17].

To date, one of the higher η_{STH} values (12.4%) was obtained through a PV–photocathode configuration, by using a p–n GaAs junction, connected in series to a p-GaInP$_2$ photocathode [18]. On the other hand, this remarkable result is of no practical use, since the stability issues and the limited large-scale feasibility make it unsuitable for industrial purpose.

The configuration shown in Fig. 2.3(d) is studied since several decades. A tandem device was proposed by Nozik in the mid-70s, by using a p-GaP photocathode together with a TiO$_2$ photoanode [19, 20]. This early attempt led to a low STH efficiency ($< 1\%$) and was limited by stability issues, but opened a promising route to photoelectrochemical fuel synthesis. Indeed, a decade later, the promising efficiency of 8.2% was achieved by Kainthla et al., through a InP photocathode functionalized with platinum islands and a MnO$_2$-protected GaAs photoanode [21, 22]. The great drawback of this cell was the high cost and scarcity of the employed elements, such as Pt and In, together with the necessity of double-side illumination [4].

Catalyst materials for oxygen and hydrogen evolution In the above discussion, it emerged the fundamental role of interface electrochemistry in order to obtain high performance artificial photosynthesis. Efficient and stable materials that can optimize the interfacial charge transfer are needed in PECs, in order to exploit the produced photocurrent and, in some cases, to stabilize semiconductors toward corrosion processes.

Efficient water oxidation catalysts (WOCs) and water reduction catalysts (WRCs) are thus needed to develop high efficiency artificial photosynthesis devices, with small overpotentials as discussed in § 2.3. Moreover, low cost and scalable WOCs and WRCs are needed to replace expensive materials such as Pt, RuO$_2$ and IrO$_2$ that are presently employed as catalysts in commercial electrolyzers.

Target values of the overpotentials for low current density (milliamperes) are of about 200 mV on the anodic side, and less than 100 mV on the cathodic side. As an example, by applying Eq. (2.5), we obtain 80% LHV efficiency with 300 mV total overpotential.

Historically, the reference materials as WOC are RuO$_2$ and IrO$_2$ [23, 24] stabilized by inert, inexpensive metal oxides, for use in acidic media. In the case of electrolyzers that operate with hot alkaline solutions, metallic nickel is an usual choice [4]. On the other hand, the optimal catalyst for water reduction in acidic solution is metallic platinum, while nickel-based metallic alloys (Ni–Mo and others) are used in basic environment [4].

Recent research is focused in developing low cost, non-toxic, scalable materials that can be successfully coupled with cheap, Earth-abundant solar absorbers. In particular, pure and mixed metal oxides are intensively studied

as WOCs to be used in alkaline environment [25–27]. The recent impulse on this topic motivated our experimental study, presented in Chapter 8, in which physical vapor deposition techniques are proposed to deposit thin films of efficient, innovative catalysts.

Moreover, a recent challenge on this field lays in the understanding of the energetics and charge transfer processes that occur between the photoactive semiconductor and the electrocatalyst. An example of advantageous engineering of the semiconductor/catalyst interplay was obtained through adaptive junctions [28], a strategy that we reproduced in our recent work presented in Chapter 7.

Final remarks: scalability requirements As we mentioned in § 1.1, the global power consumption is larger than 10 TW and it is expected to increase in the short-medium term. For this reason, the innovative solutions to replace fossil fuels need to satisfy strict scalability requirements to the aim of producing a significant impact on the global energy consumption.

In the present chapter, we examined some alternative routes to produce artificial fuels using solar irradiation as the energy source, and easily available reactants as water and carbon dioxide. In particular, we focused on solar water splitting and we reported that a target solar-to-hydrogen efficiency for photoelectrochemical devices is of about 10%. In other words, a power capacity of 10 TW of solar fuel production (intended as chemical energy production rate) would require to cover an area as large as 10^5 km^2, equivalent to the entire area of the State of Virginia, with 10% efficiency water splitting panels.

It is evident that a problem of this scale poses serious requirements to the materials to be used. The materials used in the synthesis of semiconductors, catalysts and transparent oxide layers (often used for ohmic contacts in multiple junction PECs) should be relatively Earth-abundant and economically viable.

In recent years, growing attention has been addressed to the depletion of mineral resources, with the aim of finding sustainable routes for the future guidelines of industrial production. A crucial aspect in the economic assessment of mineral extraction is the concentration of the mineral ores, since abundant but highly dispersed resources may have a poor economic return. A recent study, which considered the exergy and Hubbert peak analysis of mineral resources, showed that some metals with large industrial use, such as mercury, lead, tin, silver and gold, are the most depleted commodities [30]. Vesborg and Jaramillo directly addressed the critical discussion of the material scalability issue in view of the development of innovative solutions for renewable energy sources [29] (see Figure 2.4).
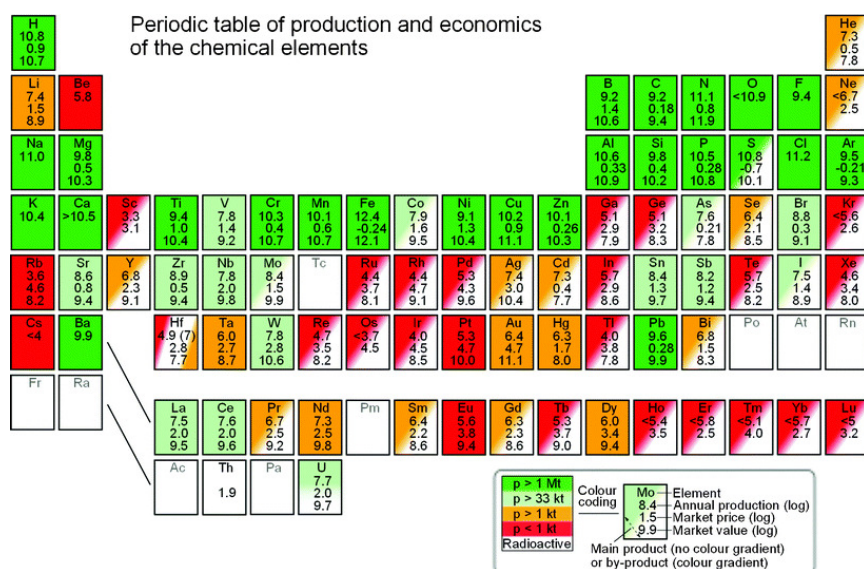
Figure 2.4: Periodic table of the elements with data for production, price and implied value for the year 2010. The color coding (green, light-green, orange and red) corresponds to overall production level (medium to high, low, very low and extremely low, respectively). Solid color is used for elements which are chiefly main economic products of their respective ores while a diagonal gradient in color is used for elements that are mostly byproducts of other elements. Reprinted with permission from [29] © The Royal Society of Chemistry, 2012.

References for Chapter 2

[1] S. M. Sze and K. K. Ng. *Physics of Semiconductor Devices*. 3rd Edition. Wiley, 2007.

[2] E. L. Miller. "Solar Hydrogen Production by Photoelectrochemical Water Splitting: The Promise and Challenge". In: *On Solar Hydrogen & Nanotechnology*. Ed. by L. Vayssieres. John Wiley & Sons, Ltd, 2010, pp. 1–35. DOI: 10.1002/9780470823996.ch1.

[3] A. J. Bard and L. R. Faulkner. *Electrochemical methods. Fundamentals and applications*. Wiley, 2001.

[4] M. G. Walter et al. "Solar Water Splitting Cells". In: *Chem. Rev.* 110 (2010), pp. 6446–6473. DOI: 10.1021/cr1002326.

[5] R. van de Krol. "Principles of Photoelectrochemical Cells". In: *Photoelectrochemical Hydrogen Production*. Ed. by R. van de Krol and M. Grätzel. Boston, MA: Springer US, 2012, pp. 13–67. DOI: 10.1007/978-1-4614-1380-6_2.

[6] J. Keable and B. Holcroft. "Economic and Business Perspectives". In: *Photoelectrochemical Hydrogen Production*. Ed. by R. van de Krol and M. Grätzel. Boston, MA: Springer, 2012, pp. 277–292. DOI: 10.1007/978-1-4614-1380-6_8.

[7] A. Kudo and Y. Miseki. "Heterogeneous photocatalyst materials for water splitting". In: *Chem. Soc. Rev.* 38 (2009), pp. 253–278. DOI: 10.1039/B800489G.

[8] M. Orlandi et al. "Porous versus Compact Nanosized Fe(III)-Based Water Oxidation Catalyst for Photoanodes Functionalization". In: *ACS Appl. Mater. Interfaces* 8 (2016), pp. 20003–20011. DOI: 10.1021/acsami.6b05135.

[9] P. Choi, D. G. Bessarabov, and R. Datta. "A simple model for solid polymer electrolyte (SPE) water electrolysis". In: *Solid State Ionics* 175 (2004), pp. 535–539. DOI: 10.1016/j.ssi.2004.01.076.

[10] K. Harrison and J. I. Levene. "Electrolysis of Water". In: *Solar Hydrogen Generation: Toward a Renewable Energy Future*. Ed. by K. Rajeshwar, R. McConnell, and S. Licht. New York, NY: Springer, 2008, pp. 41–63. DOI: 10.1007/978-0-387-72810-0_3.

[11] J. G. Mavroides, J. A. Kafalas, and D. F. Kolesar. "Photoelectrolysis of water in cells with SrTiO$_3$ anodes". In: *Appl. Phys. Lett.* 28 (1976), p. 241. DOI: 10.1063/1.88723.

[12] E. Aharon-Shalom and A. Heller. "Efficient p-InP(Rh-H alloy) and p-InP(Re-H alloy) Hydrogen Evolving Photocathodes". In: *J. Electrochem. Soc.* 129 (1982), pp. 2865–2866. DOI: 10.1149/1.2123695.

[13] D. H. van Dorp et al. "SiC: A Photocathode for Water Splitting and Hydrogen Storage". In: *Angew. Chem. Int. Ed.* 48 (2009), pp. 6085–6088. DOI: 10.1002/anie.200900796.

[14] H. Morisaki et al. "Photoelectrolysis of water with TiO_2-covered solar-cell electrodes". In: *Appl. Phys. Lett.* 29 (1976), p. 338. DOI: 10.1063/1.89088.

[15] M. Grätzel. "Photoelectrochemical cells". In: *Nature* 414 (2001), pp. 338–344. DOI: 10.1038/35104607.

[16] M. Grätzel. "Mesoscopic Solar Cells for Electricity and Hydrogen Production from Sunlight". In: *Chem. Lett.* 34 (2005), pp. 8–13. DOI: 10.1246/cl.2005.8.

[17] R. E. Rocheleau, E. L. Miller, and A. Misra. "High-Efficiency Photoelectrochemical Hydrogen Production Using Multijunction Amorphous Silicon Photoelectrodes". In: *Energy Fuels* 12 (1998), pp. 3–10. DOI: 10.1021/ef9701347.

[18] O. Khaselev and J. A. Turner. "A Monolithic Photovoltaic-Photoelectrochemical Device for Hydrogen Production via Water Splitting". In: *Science* 280 (1998), p. 425. DOI: 10.1126/science.280.5362.425.

[19] A. J. Nozik. "p–n photoelectrolysis cells". In: *Appl. Phys. Lett.* 29 (1976), p. 150. DOI: 10.1063/1.89004.

[20] A. J. Nozik. "Photochemical diodes". In: *Appl. Phys. Lett.* 30 (1977), p. 567. DOI: 10.1063/1.89262.

[21] R. C. Kainthla, S. U. M. Khans, and J. O. Bockris. "The theory of electrode matching in photoelectrochemical cells for the production of hydrogen". In: *Int. J. Hydrogen Energy* 12.6 (1987), pp. 381–392. DOI: 10.1016/0360-3199(87)90157-1.

[22] R. C. Kainthla, B. Zelenay, and J. O. Bockris. "Significant Efficiency Increase in Self-Driven Photoelectrochemical Cell for Water Photoelectrolysis". In: *J. Electrochem. Soc.* 134 (1987), pp. 841–845. DOI: 10.1149/1.2100583.

[23] S. Trasatti. "Electrocatalysis in the anodic evolution of oxygen and chlorine". In: *Electrochim. Acta* 29 (1984), pp. 1503–1512. DOI: 10.1016/0013-4686(84)85004-5.

[24] S. Trasatti. "Electrocatalysis: Understanding the success of DSA". In: *Electrochim. Acta* 45 (2000), pp. 2377–2385. DOI: 10.1016/s0013-4686(00)00338-8.

[25] C. C. L. McCrory et al. "Benchmarking Heterogeneous Electrocatalysts for the Oxygen Evolution Reaction". In: *J. Am. Chem. Soc.* 135 (2013), pp. 16977–16987. DOI: 10.1021/ja407115p.

[26] L. Trotochaud et al. "Solution-Cast Metal Oxide Thin Film Electrocatalysts for Oxygen Evolution". In: *J. Am. Chem. Soc.* 134 (2012), pp. 17253–17261. DOI: 10.1021/ja307507a.

[27] R. D. L. Smith et al. "Water Oxidation Catalysis: Electrocatalytic Response to Metal Stoichiometry in Amorphous Metal Oxide Films Containing Iron, Cobalt, and Nickel". In: *J. Am. Chem. Soc.* 135 (2013), pp. 11580–11586. DOI: 10.1021/ja403102j.

[28] F. Lin and S. W. Boettcher. "Adaptive semiconductor/electrocatalyst junctions in water-splitting photoanodes". In: *Nature Materials* 13 (2013), pp. 81–86. DOI: 10.1038/nmat3811.

[29] P. C. K. Vesborg and T. F. Jaramillo. "Addressing the terawatt challenge: scalability in the supply of chemical elements for renewable energy". In: *RSC Advances* 2 (2012), pp. 7933–7947. DOI: 10.1039/c2ra20839c.

[30] A. Valero and A. Valero. "Physical geonomics: Combining the exergy and Hubbert peak analysis for predicting mineral resources depletion". In: *Resour. Conserv. Recycl.* 54 (2010), pp. 1074–1083. DOI: 10.1016/j.resconrec.2010.02.010.

Chapter 3

Physical vapor deposition techniques

3.1 Introduction

The aim of this chapter is to introduce the physical vapor deposition (PVD) techniques that were used in the experimental work discussed in the present thesis (pulsed laser deposition, electron-beam deposition and RF-magnetron sputtering). We will leave aside the technical details of the deposition apparatuses, which will be described in the experimental sections of Chapters 8, 7 and 6, and we will focus on the technique fundamentals. We will try to elucidate the specific features of PVD techniques, by discussing the peculiarities that make them useful for both research and applications purposes.

Moreover, here we will briefly analyze some basic aspects of pulsed laser ablation and deposition, to lay the groundwork for the computational study on laser ablation mechanisms that will be given in Chapters 4 and 5.

PVD techniques are usually classified into two classes: thermal evaporative and sputtering processes [1]. Thermal evaporative techniques are based on ablation from the target surface, produced by heating the target. They include electron-beam deposition (EBD) and pulsed laser deposition (PLD). On the other hand, sputtering is obtained when the momentum transfer from particles that collide with the target is sufficient to remove atoms or molecules from the target. An example is RF-magnetron sputtering, performed by using an inert or reactive plasma glow discharge [2].

In principle, material ejection from a target due to particle–surface or laser–surface interactions can be studied through the same approach, since both charged particles and photons can interact with both electrons and lattice of the target material. Nevertheless, the relevance of the different interaction mechanisms varies significantly depending on the nature of the particle that irradiates the target and on its energy. In this way, a broad

spectrum of material ejection phenomena can be obtained.

In 1997, Kelly and Miotello systematically reviewed the relevant mechanisms of interaction of accelerated ions or laser pulses with a target surface [3]. Through an extensive review of the available literature, they proved that, in the case of ion sputtering, collisional processes at the target surface are the main mechanism of particle ejection, while thermal processes play a minor role. On the contrary, in the case of pulsed laser ablation, collisional sputtering is limited to the eventual backscattering of the emitted particles, but it is very less significant compared to the thermal-spike processes.

Depending on the environment in which laser irradiation is performed, the secondary interaction mechanisms that occur within the region of the ablated material may become very significant. The ejected material forms an ablation plume, which can develop complex gas-dynamic effects [4]. Especially in the case of PLD with relatively high ambient pressure, the spatial distribution of the laser-ablated material and nanoparticle formation may depend essentially on the secondary processes taking place in the plume, rather than on the primary ejection mechanisms (see as an example the work presented in Chapter 7). This aspect at the same time complicates and enriches the process of PLD, which can produce an extraordinary variety of film structures.

By contrast, RF-magnetron sputtering and EBD, which are commonly operated at medium vacuum (about 10^{-3} mbar) and high vacuum (about 10^{-7} mbar) [1, 5], respectively, occur in a low-collisional regime, so that the mechanism of film growth is mainly governed by deposition rate and substrate temperature.

3.2   RF-magnetron sputtering

Deposition techniques based on ion sputtering are generally obtained by exploiting the kinetic energy of accelerated ions generated within a plasma. The deposition process is performed in a vacuum chamber that is preventively evacuated up to high vacuum (10^{-7} mbar) to avoid contaminations. Then, the working gas (generally argon) is fluxed into the chamber, obtaining an equilibrium pressure of the order of 10^{-3} mbar. The plasma glow discharge is then switched on by applying a sufficiently intense electric field. This occurs through acceleration of the residual free electrons in the neutral gas (produced by random events as cosmic rays or thermal collisions) that can eventually ionize neutral atoms. When ionization events are more frequent than recombination ones, an avalanche effect is produced, so that the plasma discharge is self-sustained [6].

In a simple sputtering system, the plasma discharge can be produced between two parallel plates: the substrate (anode) and the target (cathode). The ion collisions with the target can give rise to a ballistic process that leads
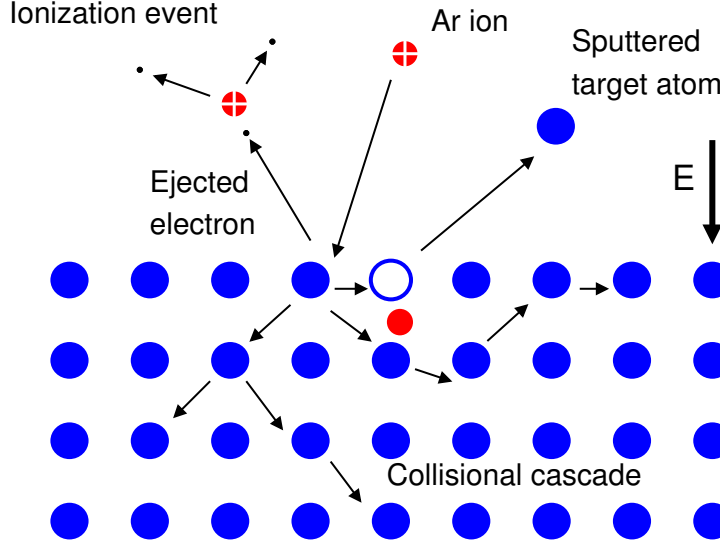
Figure 3.1: Schematic picture of the sputtering mechanism. The vector $\vec{E}$ indicates the applied electric field.

to the ejection of atoms (see the schematic picture of Figure 3.1).

The sputtering yield (Y) is defined as the average number of atoms removed from the target surface per incident ion. This quantity can be estimated on the base of the energy of the colliding ions and on the nature of the projectile and target atoms. Reliable semiempirical models were developed in the last decades in the framework of the linear cascade collision theory [7]. Within this theory, the sputtering yield depends on the energy transfer mass factor $\gamma = \frac{4m_p m_r}{(m_p + m_r)^2}$ and on the surface binding energy U_{sb} that is of few eV for common metals. A classical formula is that of Sigmund's model, formulated for ion energy $E < 1$ keV [7]:

$$Y \propto \frac{\gamma E}{U_{\mathrm{sb}}}. \tag{3.1}$$

From this simple expression, as we could expect, it is clear that, at a fixed energy and fixed target material, the sputtering yield is optimized if $m_p \approx m_r$. This is the reason why argon is used as the working gas in the case of fourth period metals as Ti, Fe and their oxides.

The ejected atoms diffuse in the vacuum chamber and can reach the substrate. The sputtered material generally has a wide energy distribution, generally up to tens of eV (10^5 K). The relatively high kinetic energy of the sputtered atoms results in a good adhesion on the substrate. The deposition rate and the substrate temperature are the main parameters that determine the structural features of the growing film.

Sputtering systems are widely used in industrial applications [1] and different setups are available. The plasma discharge can be operated either
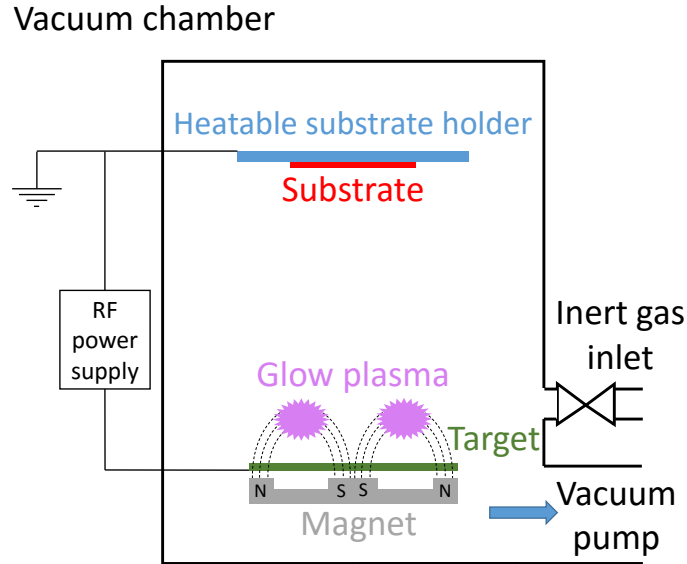
Vacuum chamber

Figure 3.2: Schematic diagram of a RF-magnetron sputtering system.

in direct current (DC) or radio frequency (RF) mode. The former is typically used in the case of conductive materials, which prevent the accumulation of electric charge, while the latter can be successfully used for conducting, semiconductor and ceramic materials (as TiO_2, Fe_2O_3, SiO_2, transparent conducting oxides, etc.).

In RF-magnetron sputtering (see Fig. 3.2), a magnetic field is used to confine the plasma in the region close to the target. This strategy results in a higher deposition rate and minimizes impurities, by reducing unwanted material erosion from other surfaces. The circular symmetry of the magnetic field produces the typical toroidal shape of the confined plasma region (see also Chapter 6).

3.3 Deposition by evaporative condensation

Evaporative deposition methods are the simplest PVD techniques, since they just rely on heating the precursor material up to high temperature, when vaporization occurs at a suitably high rate. Evaporation is performed in a large vacuum chamber, in a pressure regime at which the mean free path of ejected atoms is comparable or greater than the chamber dimension (typically $10^{-6} \div 10^{-7}$ mbar) [5].

The evaporant (normally a pure metallic element) is heated in a refrac-
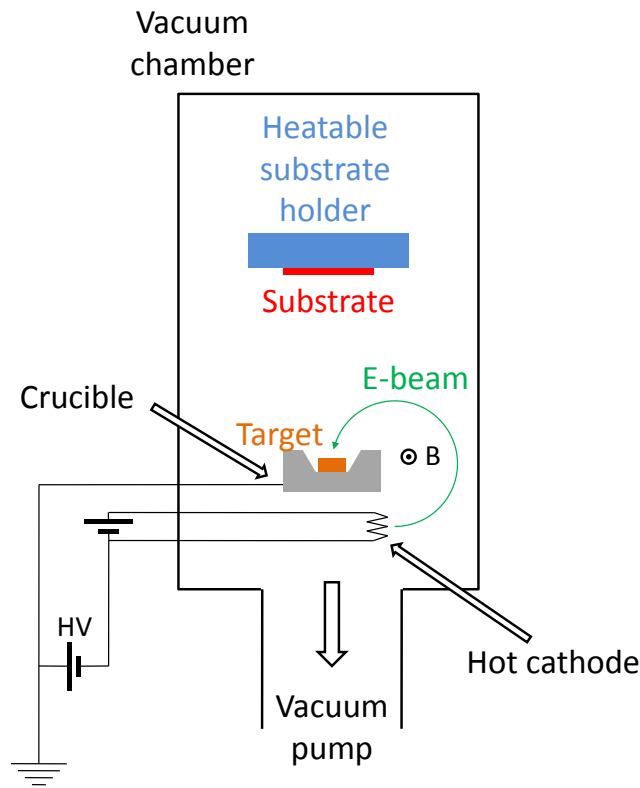
Figure 3.3:   Schematic diagram of an electron-beam deposition system.

tory crucible, usually at a temperature between the melting point and the boiling point. The deposition rate is monitored during operations (for example by using a quartz crystal microbalance) and the conditions are adjusted so that the vaporization rate is sufficiently rapid to coat the interior of the vacuum chamber, including the substrates, with a film of the evaporated material.

The vaporized material typically do not undergo collisions during the flight toward the substrate, thus condensation only occurs on the substrate. In this way, compact films are produced, with a surface morphology that depends on the substrate temperature and on the interfacial interactions between substrate and film materials.

The need of a high vacuum apparatus tends to limit this deposition method to relatively high value products, such as uniform reflective coatings or electrically conductive thin films [1].

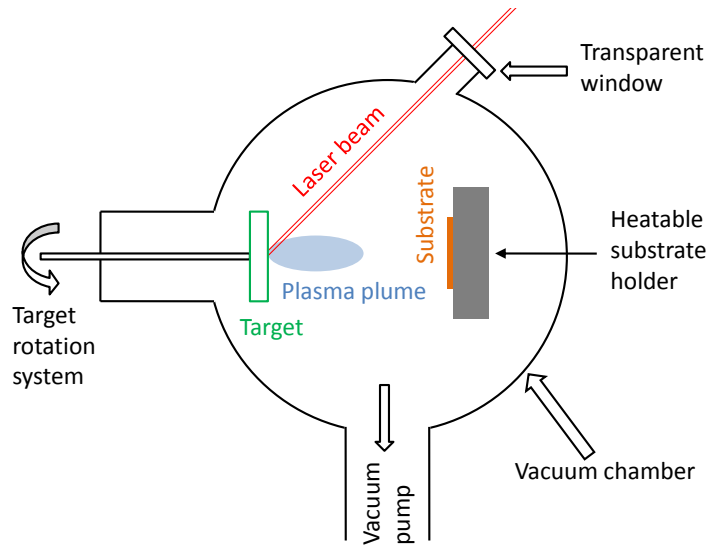In the case of electron-beam deposition, the material to be evaporated is

Figure 3.4: Schematic diagram of a PLD system.

heated by an energetic electron beam (some keV) emitted by a hot cathode (usually a tungsten filament) below the crucible. A magnetic field produced by electromagnets drives the electrons through a curved 270° trajectory as shown in Figure 3.3. This configuration is designed to avoid contaminations coming from the hot filament, since only electrons are driven by the electromagnetic field to the crucible.

The potential difference of some kV is applied between the hot cathode and the crucible holder, which is at ground potential. EBD technique is largely used in industrial applications, especially for surface metalization [1] and it is also employed for research purposes, including the deposition of metal oxides [8, 9].

3.4 Pulsed laser deposition

Pulsed laser deposition, to some extent, can be included in the thermal evaporative deposition techniques but, on closer inspection, it reveals a complex nature, which results in its unique features. PLD is obtained by focusing a high power, short pulse laser inside a vacuum chamber on a target. If the energy density is high enough, the target material is ablated, forming a plasma plume, which expands along the direction normal to the target surface. Usually, the laser beam strikes the target at an angle of 45°, so that the substrate can be placed in front of the target, parallel to it (see Figure 3.4).

The energy deposition from the laser radiation to the target material

occurs through the increase of the electron energy [10]. Then, this energy is transfered to the target lattice, through electron–phonon interactions. This process is successfully described in the framework of the two-temperature model (TTM) formulated by Anisimov [11]:

$$C_e(T_e)\frac{\partial T_e}{\partial t} = \nabla\left[K_e(T_e)\nabla T_e\right] - G(T_e - T_l) + C_e(T_e)S(t) \qquad (3.2)$$

$$C_l(T_l)\frac{\partial T_l}{\partial t} = \nabla\left[K_l(T_l)\nabla T_l\right] + G(T_e - T_l), \qquad (3.3)$$

where C and K are the heat capacity and the thermal conductivity of electrons (subscript e) and lattice (subscript l), respectively. G is the electron–phonon coupling factor, while S is the source term, accounting for the energy transfered from photons to electrons. The electron energy distribution is equilibrated by electron–phonon interactions at a typical timescale of few picoseconds [12, 13].

PLD is usually performed with lasers pulses of very different time duration, mainly from nanoseconds (e.g. Nd:YAG or excimer lasers) to femtoseconds (e.g. Ti:sapphire laser) [14]. In this way, a different phenomenology is observed depending on the timescale of the laser pulse.

In the present thesis, we will deal with nanosecond laser pulses. In particular, a KrF excimer laser (25 ns pulse duration) was used in the experimental work, see Chapter 7, while 20 ns FWHM Gaussian pulses were considered in the computational simulations of Chapter 5. In the case of nanosecond laser heating, it is permitted to consider local thermal equilibrium. In particular, our computational approach describes nanosecond laser ablation of metals through a continuum model, based on thermodynamics [15].

On the other hand, in the case of ultrashort laser pulses, strong electron–phonon nonequilibrium conditions can be obtained [16]. As an example, in molecular dynamics simulations of pulsed laser ablation of aluminum with 100 fs laser pulses, thermal processes develop on the scale of picoseconds [17], and the TTM formalism is necessarily taken into account.

The usual energy densities employed in the PLD of metallic materials are sufficient to raise the temperature of the target's external layers well above the melting point. The heating rate is so high (about $10^{11} \div 10^{12}$ K/s) that normal boiling due to heterogeneous nucleation cannot occur because vapor bubble diffusion is a too much slow process [18]. In this way, the target surface can be heated well above the boiling temperature, becoming a metastable liquid. In metastable liquids when the temperature comes close to the thermodynamic critical point T_c, homogeneous nucleation occurs with an extremely fast kinetics driven by thermal density fluctuations. If the energy fluence is high enough, the target surface can break into a mixture of vapor and liquid droplets [19].

This phenomenon is known as phase explosion, and it was predicted for

target temperatures of about $0.9T_c$ [20]. Of course, at high temperature also normal vaporization takes place at a high rate, so that the main mechanisms of the nanosecond laser ablation of metals are vaporization and phase explosion.

Plasma plume dynamics   The mixture of vapor and liquid nanodroplets ejected from the target surface expand adiabatically and form a plasma plume, since a certain fraction of the vapor is ionized due to the high temperature and to laser irradiation.

If the expansion takes place in vacuum, the ejected material undergoes an approximately free adiabatic expansion, with a self-similar plume shape [21]. If the ablation takes place in a background gas, depending on the background pressure and on the nature of the two elements, the plume expansion may be slowed down by collisions. The vapor phase can be broken up into components, or scattering orders, whose particles undergo 0, 1, 2,... collisions with the background [22].

The ambient gas type and pressure have significant influence on the deposited material properties. Firstly, by promoting vapor cooling and condensation, the ambient gas can be useful for example to control the morphology and the compressive strain of the deposited film. Secondly, background gas may participate actively in the chemistry of the deposited film. This is the case of reactive ablation where, as an example, a metallic target is irradiated in an oxygen atmosphere, by depositing a metal oxide on the substrate. Both these effects were used in the experimental work presented in Chapter 7. By using inert gases (e.g. argon) as the background atmosphere, it is possible to control film morphology without altering the stoichiometry of the ablated material [23].

Film formation   The nucleation and growth of the film on the substrate depend on many tunable parameters such as the ablation mechanism, substrate temperature, background gas type and pressure. One of the features that make PLD particularly attractive is the possibility of depositing composite materials directly obtained from multicomponent targets irradiated in vacuum or in an inert atmosphere. Indeed, unlike thermal evaporation, the non-equilibrium nature of phase explosion makes the ablation process independent from the saturated vapor pressure of the target constituents, and nanoclusters can be directly ejected from the surface.

Pulsed laser deposition can be used for the deposition of compact or porous films. Film thickness can be adjusted by varying the number of laser pulses. The deposited material per laser pulse depends on several factors, including target to substrate distance, background gas pressure, laser spot area and laser energy fluence. In usual PLD experimental conditions, the deposition rate per laser pulse can range from 0.001 to 1 Å per pulse. In

this way, when suitable diagnostic equipment is installed, PLD enables shot-to-shot control of the deposition process, which is ideal for multilayer and interface formation where submonolayer control is needed [24].

In order to meet the needs of industrial applications, a crucial aspect is the possibility of adapting PLD to cover large area substrates with a sufficiently uniform film. Indeed, the dynamics of the ablated material generally results in a highly focused angular distribution, leading to a significant variation in deposition rate over distances of about a few centimeters. Nevertheless, uniform coatings can be obtained through a proper manipulation of the substrate positioning and by employing a suitable rotating target support for a uniform target erosion [25].

Large area PLD systems are nowadays available. In the last decade, many PLD equipments for industrial production purposes have been commercialized, usually with integrated robotic wafer handlers, some of them capable of depositing uniform films on 300 mm diameter substrates or to run a single deposition process to cover a 10 m^2 active area tape [26]. It is clear that the challenge of designing large area industrial apparatuses is just a matter of time, mainly regarding mechanics and vacuum technology, while the complex issue on the scientific side is that of deeply understanding the physics of laser ablation and film formation processes.

References for Chapter 3

[1] J. R. Roth. "Applications to Nonthermal Plasma Processing". In: *Industrial Plasma Engineering*. Vol. 2. Institute of Physics, 2001.

[2] K. Wasa, M. Kitabatake, and H. Adachi. *Thin Film Materials Technology. Sputtering of compound materials*. Springer, 2004.

[3] R. Kelly and A. Miotello. "On the mechanisms of target modification by ion beams and laser pulses". In: *Nucl. Instr. and Meth. in Phys. B* 122 (1997). DOI: 10.1016/S0168-583X(96)00765-3.

[4] R. Kelly. "On the dual role of the Knudsen layer and unsteady, adiabatic expansion in pulse sputtering phenomena". In: *J. Chem. Phys.* 92 (1990), p. 5047. DOI: 10.1063/1.458540.

[5] R. V. Stuart. *Vacuum Technology, Thin Films, and Sputtering. An Introduction*. New York, NY: Academic Press, 1983.

[6] J. R. Roth. "Principles". In: *Industrial Plasma Engineering*. Vol. 1. Institute of Physics, 1995.

[7] J. E. Mahan and A. Vantomme. "A simplified collisional model of sputtering in the linear cascade regime". In: *J. Vac. Sci. Technol., A* 15 (1997), p. 1976. DOI: 10.1116/1.580668.

[8]   T. Warang et al. "Co$_3$O$_4$ nanoparticles assembled coatings synthesized by different techniques for photo-degradation of methylene blue dye". In: *Appl. Catal., B* 132–133 (2013), pp. 204–211. DOI: 10.1016/j.apcatb.2012.11.040.

[9]   R. E. Marvel et al. "Electron-beam deposition of vanadium dioxide thin films". In: *Appl. Phys. A* 111 (2013), pp. 975–981. DOI: 10.1007/s00339-012-7324-5.

[10] J. Reif. "Material Response to Laser Energy Deposition (Thermal and Hyperthermal Processes)". In: *Lasers in Materials Science.* Ed. by M. Castillejo, P. M. Ossi, and L. Zhigilei. Springer Series in Materials Science. Springer, 2014. Chap. 2. DOI: 10.1007/978-3-319-02898-9_2.

[11] S. I. Anisimov, B. L. Kapeliovich, and T. L. Perel'man. "Electron emission from metal surfaces exposed to ultrashort laser pulses". In: *Sov. Phys. JETP* 39 (1974), pp. 375–377.

[12] R. W. Schoenlein et al. "Femtosecond studies of nonequilibrium electronic processes in metals". In: *Phys. Rev. Lett.* 58.16 (1987), pp. 1680–1683. DOI: 10.1103/PhysRevLett.58.1680.

[13] P. B. Allen. "Theory of thermal relaxation of electrons in metals". In: *Phys. Rev. Lett.* 59.13 (1987), pp. 1460–1463. DOI: 10.1103/PhysRevLett.59.1460.

[14] R. F. Haglund. "Laser Physics for Materials Scientists: A Primer". In: *Lasers in Materials Science.* Ed. by M. Castillejo, P. M. Ossi, and L. Zhigilei. Springer, 2014, pp. 1–28. DOI: 10.1007/978-3-319-02898-9_1.

[15] A. Mazzi, F. Gorrini, and A. Miotello. "Liquid nanodroplet formation through phase explosion mechanism in laser-irradiated metal targets". In: *Phys. Rev. E* 92 (2015), 031301–R. DOI: 10.1103/PhysRevE.92.031301.

[16] Z. Lin, L. V. Zhigilei, and V. Celli. "Electron-phonon coupling and electron heat capacity of metals under conditions of strong electron-phonon nonequilibrium". In: *Phys. Rev. B* 77 (2008), p. 075133. DOI: 10.1103/PhysRevB.77.075133.

[17] C. Wu and L. V. Zhigilei. "Microscopic mechanisms of laser spallation and ablation of metal targets from large-scale molecular dynamics simulations". In: *Appl. Phys. A* 114 (2014), p. 11. DOI: 10.1007/s00339-013-8086-4.

[18] R. Kelly and A. Miotello. "Contribution of vaporization and boiling to thermal-spike sputtering by ions or laser pulses". In: *Phys. Rev. E* 60.3 (1999), pp. 2616–2625. DOI: 10.1103/PhysRevE.60.2616.

[19] A. Miotello and R. Kelly. "Critical assessment of thermal models for laser sputtering at high fluences". In: *Appl. Phys. Lett.* 67 (1995), pp. 3535–3537. DOI: 10.1063/1.114912.

[20] M. M. Martynyuk. "Phase explosion of a metastable fluid". In: *Comb. Exp. Shock Waves* 13.2 (1977), pp. 178–191. DOI: 10.1007/BF00754998.

[21] T. E. Itina et al. "Laser-generated plasma plume expansion: Combined continuous-microscopic modeling". In: *Phys. Rev. E* 66 (2002), p. 066406. DOI: 10.1103/PhysRevE.66.066406.

[22] R. F. Wood et al. "Dynamics of plume propagation and splitting during pulsed-laser ablation of Si in He and Ar". In: *Phys. Rev. B* 58.3 (1998). DOI: 10.1103/PhysRevB.58.1533.

[23] M. Schenato et al. "Effect of annealing and nanostructuring on pulsed laser deposited WS_2 for HER catalysis". In: *Appl. Catal., A* 510 (2016), pp. 156–160. DOI: 10.1016/j.apcata.2015.11.009.

[24] D. P. Norton. "Pulsed Laser Deposition of Complex Materials: Progress Toward Applications". In: *Pulsed Laser Deposition of Thin Films*. Wiley, 2006, pp. 1–31. DOI: 10.1002/9780470052129.ch1.

[25] M. Bonelli, C. Cestari, and A. Miotello. "Pulsed laser deposition apparatus for applied research". In: *Meas. Sci. Technol.* 10 (1999), pp. 97752–97754. DOI: 10.1088/0957-0233/10/3/024.

[26] J. A. Greer. "History and current status of commercial pulsed laser deposition equipment". In: *J. Phys. D: Appl. Phys.* 47 (2014), p. 034005. DOI: 10.1088/0022-3727/47/3/034005.

44

Chapter 4

Modeling of metal nanoparticle formation in PLD

Preview The present chapter, together with the following Chapter 5, describe an original modeling in the fundamentals of laser ablation of metals using nanosecond laser pulses. Through a continuum approach, we study quantitative aspects of the phase explosion mechanism, leading to liquid nanoparticle generation and ejection from the target.

Our model is developed on a wide set of pure metals commonly used in PLD (Al, Fe, Co, Ni, Cu, Ag and Au), while in Chapter 5 more detailed space–time resolved simulations are performed on aluminum. Although our present approach is currently limited to the thermal mechanisms occurring close to the laser-irradiated target surface, the present study could be extended in order to describe a more complex phenomenology, such as PLD in a reactive atmosphere.

The content of this chapter was adapted from:
A. Mazzi, F. Gorrini and A. Miotello, Phys. Rev. E 92 (2015), 031301(R).
© American Physical Society, 2015.

4.1 Introduction

The pulsed laser ablation of metals in vacuum and liquids allows the synthesis and deposition of small size nanoparticles (NPs) with useful peculiar features as compared with conventional techniques, especially the possibility of obtaining a large variety of complex nanostructures just by varying a few deposition parameters [1–3].

The material ejection in the laser ablation of pure metals proceeds through thermal mechanisms, mainly vaporization, spallation and phase explosion [4, 5] followed by some slower processes leading to the expulsion of liquid particles, usually observed in fast imaging experiments [6].

Phase explosion was found to be the most efficient mechanism in the pulsed laser ablation of metals when looking at thermal processes for sufficiently short timescales (in the nanosecond to femtosecond range) [4]. This phenomenon is predicted to occur in metastable liquids at temperatures of about 90% of the thermodynamic critical temperature T_c [7], when a so dense distribution of vapor bubbles is generated through homogeneous nucleation that the liquid phase is broken into a mixture of vapor and small scale liquid droplets, leaving the target [8].

In the modeling of phase explosion conditions, continuum approaches based on thermodynamics are led to the limits of their validity. On the other hand continuum models are very handy and accessible [9], and it is worthwhile to compare their predictions and extrapolations with the results coming from experiments and atomistic simulations.

The goal of this chapter is to describe the phase explosion process in a metal target through a continuum approach. The starting point of our study is the description of the thermodynamic properties of metastable liquid metals up to temperatures close to T_c (§ 4.2). Then, the theory of homogeneous nucleation is briefly considered (§ 4.3) with the goal of designing a 3D Monte Carlo (MC) simulation of homogeneous nucleation (§ 4.4). In particular we will use the known nucleation theory to evaluate the critical radius r_c of vapor bubbles, generated in phase explosion and to be used in the simulation.

The MC simulation aims to generate a dense and connected distribution of supercritical vapor bubbles, which causes the breaking of the liquid phase giving rise to a distribution of liquid nanodroplets and vapor atoms. The solidification of liquid nanodroplets, during flight from target to substrate, and also on substrate, generates nanoparticles if ablation occurs in vacuum conditions. In presence of an external atmosphere, other mechanisms are present, especially collisional cooling leading to condensation of expelled atoms.

The liquid vs vapor composition of the bulk material in phase explosion conditions as well as the size distribution of the expelled liquid nanodroplets are calculated (§ 4.5). Our results, regarding a set of seven metals (Al, Fe, Co, Ni, Cu, Ag and Au) commonly used as pure targets in laser ablation experiments, are compared with the available literature data, regarding both experimental data and molecular dynamics simulations. While designing the MC simulation we focused it on nanosecond irradiation regime in order to be able to make some simplifying assumptions.

4.2 Thermodynamic properties of metastable liquid metals

Since our study aims to describe liquid nanodroplet expulsion from laser irradiated targets leading to nanoparticle production in phase explosion process, we are particularly interested in those models that relate the thermodynamic critical point to surface tension, which is the fundamental quantity which allows us to describe the homogeneous nucleation of vapor bubbles in the superheated liquid.

Quite recently, Blairs et al. [10] derived a method to calculate T_c using surface tension and liquid density values at the melting point, T_m. The approach is based on the Lennard–Jones potential for liquid metals. Their study is based on experimental fitting of semiempirical laws with data regarding 18 different metals. As a result, their work provides an equation to predict T_c for pure metals, looking at the experimental measurements of surface tension and molar volume (σ_m and v_m) both given at T_m:

$$T_c = \sigma_m \left(\frac{v_m \cdot m}{(C \cdot v_m)^{5/6} - q} \right)^4,$$ (4.1)

where $m = 8.9733 \times 10^{-19}$, $q = -1.0459 \times 10^{-25}$ and $C = 1.484 \pm 0.025$ are empirical fit parameters. In Table 4.1 we show the estimations of T_c for the metallic elements examined in our study. Details about the data for σ_m and v_m are given in Table 4.2.

Metal	T_c (K)	ρ_c (kg/m^3)	P_c (10^8 Pa)
Al	6319	634	3.2
Fe	8059	1467	5.4
Co	7710	1350	5.4
Ni	7241	2159	6.5
Cu	5741	2363	4.6
Ag	5851	2718	3.3
Au	7003	5066	3.9

Table 4.1: Critical parameters estimated in this work.

While studying liquid–vapor phase transition of a pure substance, the fundamental thermodynamic quantities describing the two coexisting phases (temperature, saturated vapor pressure p_s, vapor and liquid molar volumes v_v and v_l) obey to the Clausius–Clapeyron equation:

$$\frac{dp_s}{dT} = \frac{\Delta h_v(T)}{T[v_v(T) - v_l(T)]},$$ (4.2)

where Δh_v is the molar enthalpy of vaporization. In the present study we will consider semi-empirical models for the functions $\Delta h_v(T)$, $v_v(T)$ and

Metal	M [11] (g/mol)	T_m [11] (K)	T_b [11] (K)	ρ_m [11] (kg/m^3)	σ_m [12] (N/m)	$\Delta h_v (T_b)$ (kJ/mol)
Al	26.982	933	2792	2375	1.05	294[11]
Fe	55.845	1811	3134	6980	1.909	355[13]
Co	58.933	1768	3200	7750	1.928	375[13]
Ni	58.693	1728	3186	7810	1.834	378[13]
Cu	63.546	1358	2835	8020	1.374	300[13]
Ag	107.868	1235	2435	9320	0.955	255[13]
Au	196.867	1337	3129	17310	1.162	324[11]

Table 4.2: Parameters used for the thermodynamic modeling with corresponding references: molar mass M, melting temperature T_m, boiling temperature T_b, liquid density at melting point ρ_m, surface tension at melting point σ_m and enthalpy of vaporization at boiling point $\Delta h_v (T_b)$.

$v_l (T)$ and we will integrate the Clausius–Clapeyron differential equation to compute $p_s (T)$, similarly to the approach proposed by Hornung [14].

According to theoretical and computational studies, together with experimental observations [15–18] the liquid and vapor densities, ρ_l and ρ_v, at phase coexistence can be modeled as two power series, with universal exponents and four material-dependent coefficients:

$$\begin{cases} \frac{\rho_l(T)}{\rho_c} = & 1 + D_0 \Delta T + C_1 (\Delta T)^{\beta_c} + D_1 (\Delta T)^{1-\alpha} + C_2 (\Delta T)^{\beta_c + \Delta} \\ \frac{\rho_v(T)}{\rho_c} = & 1 + D_0 \Delta T - C_1 (\Delta T)^{\beta_c} + D_1 (\Delta T)^{1-\alpha} - C_2 (\Delta T)^{\beta_c + \Delta} , \end{cases} \quad (4.3)$$

where $\Delta T = \frac{T_c - T}{T_c}$, $\alpha \approx 0.109$, $\beta_c = 0.325$ and $\Delta = 0.51$. Equation (4.3), independently from the choice of the coefficients, is consistent with the fact that the densities of both the phases tend to the critical density ρ_c at the critical point.

In the present work, we give estimations of ρ_c and of the coefficients D_0, D_1, C_1 and C_2, obtained through a least square fit of Eq. (4.3) with available experimental data for ρ_l in the range $T_m < T < T_b$ where T_m and T_b are the temperatures at the melting point and at the normal boiling point. Near T_b we assume an ideal gas behavior, which provides $\rho_v (T_b) = \frac{m P_\text{atm}}{k_B T}$ and $\frac{d\rho_v}{dT} (T_b) = \frac{m P_\text{atm}}{k_B T} \frac{\frac{\Delta h_v}{R T_b} - 1}{T_b}$. Final results are reported in Table 4.3.

The predicted coexistence curve, shown in Figure 4.1(a), is similar to the results of recent papers [17, 18].

Concerning the enthalpy of vaporization, we refer to the well known formula proposed by Watson in 1943 [23], which can be applied to the entire liquid range from T_m to T_c:

$$\Delta h_v (T) = \Delta h_{v0} \left(\frac{\Delta T}{\Delta T_0} \right)^{0.38} . \quad (4.4)$$

Metal	ρ_c (kg/m^3)	D_0	C_1	D_1	C_2
Al [19]	634 ± 5	1.1 ± 0.2	1.75 ± 0.04	-0.17	0.08
Fe [20]	1467 ± 53	1.8 ± 0.5	1.51 ± 0.08	-0.24	1.02
Co [11, 21]	≈ 1350	≈ 3.1	≈ 1.3	-0.70	2.01
Ni [20]	2159 ± 45	1.1 ± 0.3	1.75 ± 0.04	-0.15	0.10
Cu [19]	2363 ± 23	1.2 ± 0.2	1.82 ± 0.03	-0.27	-0.02
Ag [11, 22]	2718 ± 55	1.4 ± 0.3	1.68 ± 0.04	-0.57	0.06
Au [22]	5066 ± 5	1.4 ± 0.1	1.73 ± 0.01	-0.64	-0.07

Table 4.3: Results of the density interpolations. In the first column, the references for the experimental measurements of the liquid density used in the calculation.

(a) (b)
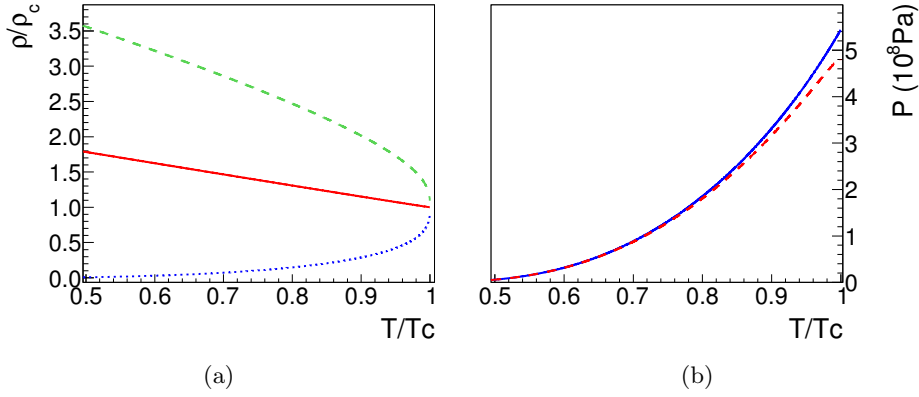
Figure 4.1: (a) Coexistence curve. ρ_l/ρ_c (dashed green curve), ρ_v/ρ_c (dotted blue) and average density (solid red). (b) Saturated pressure (solid blue) and vapor pressure (dashed red), calculated for iron.

It is an empirical law, where T_0 and Δh_{v0} are data generally associated to the normal boiling point, say T_b and $\Delta h_v(T_b)$. Equation (4.4) was proved to be a reliable estimation for many organic and inorganic pure substances [24] and also for transition metals [25].

Finally, for the temperature dependence of surface tension, we employ the empirical formula proposed in 1945 by Guggenheim [26]:

$$
\sigma\left(T\right) = \sigma_0 \left(1 - \frac{T}{T_c}\right)^{\frac{11}{9}} = \sigma_m \left(\frac{\Delta T}{\Delta T_m}\right)^{\frac{11}{9}}, \tag{4.5}
$$

with $\Delta T_m = \frac{T_c - T_m}{T_c}$ This formula is still well considered, and has been applied to various chemical compounds [24] and recently also to metallic elements [27].

4.3 Homogeneous nucleation modeling

Here we will briefly look at the theory of homogeneous nucleation of vapor bubbles in a metastable liquid in order to estimate the typical values of the critical radius r_c of vapor bubbles, which is the only physical parameter to be given as an input to our computational simulation. At the end of this analysis we fix the time duration of phase explosion (below precisely defined) at $\tau_{\mathrm{pe}} = 1$ ns. This choice, operated in the framework of the nucleation theory, will allow us to consistently calculate the thermodynamic and kinetic quantities to characterize phase explosion and, furthermore, to estimate the critical radius as required by the MC method.

The appearance of a gas bubble in a bulk liquid phase is microscopically determined by the presence of a vapor-like density fluctuation staying in labile thermodynamic equilibrium with the liquid [28] (homogeneous nucleation). This fluctuation will generate a critical nucleus if, by acquiring even a single additional molecule, it starts growing spontaneously.

In classical nucleation theory, assuming the liquid to be incompressible and the vapor to behave ideally, the vapor pressure inside critical spherical nuclei (p_v) is given by [29]:

$$p_v = p_s \exp\left[(p_l - p_s)\, \frac{v_l}{RT} \right], \tag{4.6}$$

where p_l and v_l are the pressure and the molar volume of the liquid phase, respectively. Since the saturated vapor pressure can be obtained through integration of the Clausius–Clapeyron equation (4.2), we only need an estimation of p_l in order to calculate p_v from Eq. (4.6). In the case of pulsed laser ablation of metals in vacuum, p_l is determined by the pressure exerted on the molten target surface by the vaporized material. To our purpose we can consider the surface temperature T_s to be of the order of $0.90 T_c$ and the environment gas pressure negligible compared to the saturated vapor pressure $p_s(T_s)$. An idealized solution was proposed by Anisimov [30] and further developed by Knight [31], with the final outcome $p_l = 0.55 p_s(T_s)$. This means that, under pulsed laser ablation of metals in vacuum, the metastable liquid reaches pressures of the order of 10^8 Pa due to the recoil pressure.

The radius of the critical nuclei can be described by:

$$r_c = \frac{2\sigma}{p_v - p_l}. \tag{4.7}$$

The nucleation of such critical nuclei requires to overcome the energy barrier given by the free energy of formation W_c, for which we can obtain the following Gibbs classical expression:

$$W_c = \frac{4}{3}\pi r_c^2 \sigma = \frac{16\pi\sigma^3}{3\left(p_v - p_l\right)^2}. \tag{4.8}$$
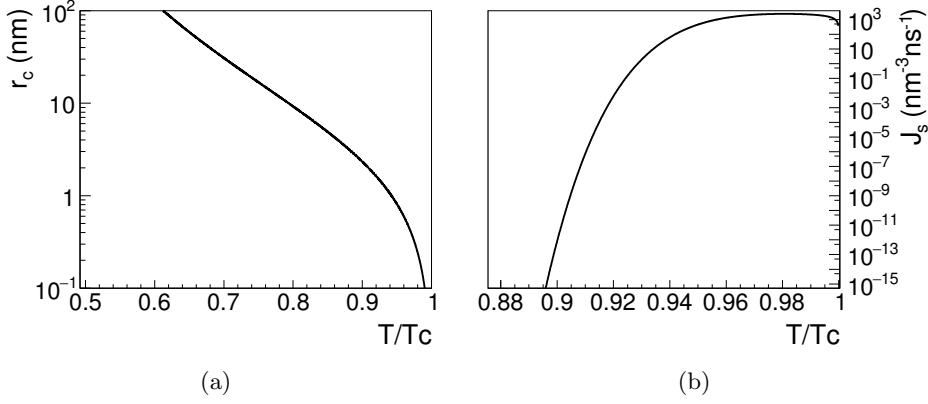
Figure 4.2: (a) Critical radius of vapor bubbles in the metastable liquid. (b) Nucleation rate of supercritical bubbles, calculated for iron.

Finally, the nucleation rate J_s of near-critical vapor nuclei per unit volume in the case of a steady nucleation process can be expressed, thanks to a theoretical result obtained by Döring [32] and Volmer [33], in the form reported by Skripov [34]:

$$J_s = n_l \sqrt{\frac{6\sigma}{(3-b)\pi m}} e^{-\frac{\Delta h_v}{RT}} e^{-\frac{W_c}{k_B T}}, \qquad (4.9)$$

where $b = 1 - \frac{p_l}{p_v}$, Δh_v is the molar enthalpy, R is the gas constant, the factor n_l is the number density for the metastable liquid and W_c can be obtained from Equation (4.8). In this chapter, since we assume the target temperature to be constant over time, we will calculate the nucleation rate as in the steady-state expression of Eq. (4.9). In Chapter 5, while considering time resolved simulations, we will discuss a more elaborated model of unsteady homogeneous nucleation.

By neglecting both spatial gradients and temporal variations of the temperature in the material, we are able to estimate the phase explosion time $\tau_{\mathrm{pe}}(T)$ as a function of the temperature, defined as the time interval between the appearance of the first critical vapor bubble and phase explosion, at a given temperature T_{pe}, which occurs when the distribution of critical bubbles will saturate the liquid volume. The vapor bubble packing fraction can be expressed by the ratio $\eta = \frac{V_v}{V_{\mathrm{tot}}}$ and the maximum packing fraction results to be $\eta_{\max} = 0.30$ according to MC simulation reported below. With these assumptions, $\tau_{\mathrm{pe}}(T)$ results to have the following analytic expression:

$$\tau_{\mathrm{pe}} = \frac{\alpha}{J_s V_c} \ln\left(1 + \frac{\eta_{\max}}{1-\eta_{\max}} \frac{1}{\alpha}\right), \qquad (4.10)$$

where $\alpha = \frac{\rho_l}{\rho_v}$ and V_c is the volume of a critical vapor bubble. In the following

MC simulation, we chose $\tau_{\mathrm{pe}} = 1$ns, as indicative example, with a consistent choice of the other quantities, in particular a constant temperature T_{pe} defined by $\tau_{\mathrm{pe}}(T_{\mathrm{pe}}) = 1$ ns: looking at the temperature dependence of J_s in Figure 4.2(b), the contribution of nucleation at temperatures lower than that of the stationary regime results to be ineffective, due to the negligible kinetics.

4.4   3D Monte Carlo simulation for phase explosion

In our MC simulation, we suppose phase explosion to occur, according to [35], when supercritical vapor bubbles, generated in a metastable liquid volume through random homogeneous nucleation, are in contact with each other forming a kind of percolation cluster in the considered volume. At that moment, liquid nanodroplets and vapor are expelled and we are able to study the final composition of the vapor/liquid mixture and to evaluate the size distribution of the generated nanodroplets leading to nanoparticles.

The critical radius of the vapor bubbles r_c is calculated through Eq. (4.7) at T_{pe}. The observed portion of target is a 3D cubic volume with size L. If we consider r_c of aluminum at T_{pe} ($r_c = 1.76$ nm), the largest system that was studied is a cubic box with side $L = 250$ nm, where about 30 thousands liquid droplets have been identified.

Our adopted MC method randomly generates N *nucleation sites* (i.e. bubble centers with first-neighbor distance larger than $2r_c$) with uniform distribution in order to saturate the available volume. Then, for each site, a bubble radius $r \gtrsim r_c$ is assigned on the base of the algorithm here described. The array of nucleation sites is arranged in ascending order according to first-neighbor distance so that the radius assignment proceeds with the following rule: if the i-th bubble is the first-neighbor of its first-neighbor with distance d in this random distribution, both of them will have radius $r = d/2$. Otherwise the first-neighbor of the i-th bubble, let's say the j-th bubble, has to be already developed, with radius $r_j < d/2$. In this latter case, $r_i = d - r_j$. In this way, the bubbles get in touch with their neighbors, with no overlap. A spherical shape is assumed for the nucleated vapor volumes: this is a simplifying assumption but note that the spherical shape is associated to the minimization of the free energy of the system.

In our case, with a random packing of non-monodispersed spheres we obtained a maximum packing fraction of about $\eta_{\max} = \frac{V_{\mathrm{bubbles}}}{V_{\mathrm{tot}}} \approx 0.30$. This value, which represents the intrinsic saturation of our bubble nucleation algorithm, has been taken as a reference for the definition of a dense and connected distribution of supercritical bubbles, as discussed above.

The final step is to study the breaking of the remaining intervolume into liquid nanodroplets. In particular, the remaining liquid phase is still

connected, but saturated of vapor bubbles that are in touch with each other along many directions. This 3D problem is rather complex and the adopted algorithm described below is the choice we made after testing of different solutions.

In order to separate the intervolumes, a fixed quantity of probe sites is randomly generated in the liquid volume and for each site the distance from the first liquid–vapor surface is evaluated along 40 randomly generated directions. Through a weighted average procedure, a radius is associated to each site and overlapping liquid spheres are considered as parts of the same liquid cluster. In this way, a distribution of disconnected liquid clusters is identified.

In particular, the 3D adopted algorithm, as described above, when transferred to 2D, gives results easily viewable and checkable as reported in Figure 4.3.
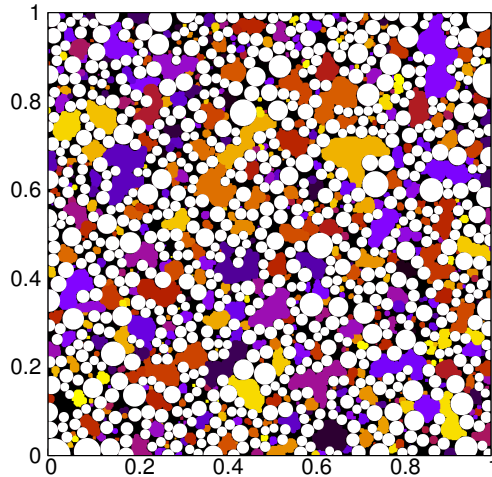
Figure 4.3: 2D simulation: supercritical bubbles in white and liquid intervolumes with different colors.

4.5   Results and discussion

In Figure 4.4(a), we show the resulting size distributions of bubbles and droplets, where the physical parameters of silver have been considered ($r_c = 1.67$ nm). We can compare our result with some recent experimental observation of silver nanoparticles as deposited in vacuum on a substrate and detected by transmission electron microscopy (TEM) [36], Figure 4.4(b). The peak in the diameter distribution observed with our simulation is predicted at about 2.00 nm (1.63 nm if we consider the thermal contraction from T_{pe} to room temperature). The experimental histogram shows a peak diameter of about 5 nm. Some modifications of the distribution are expected

54
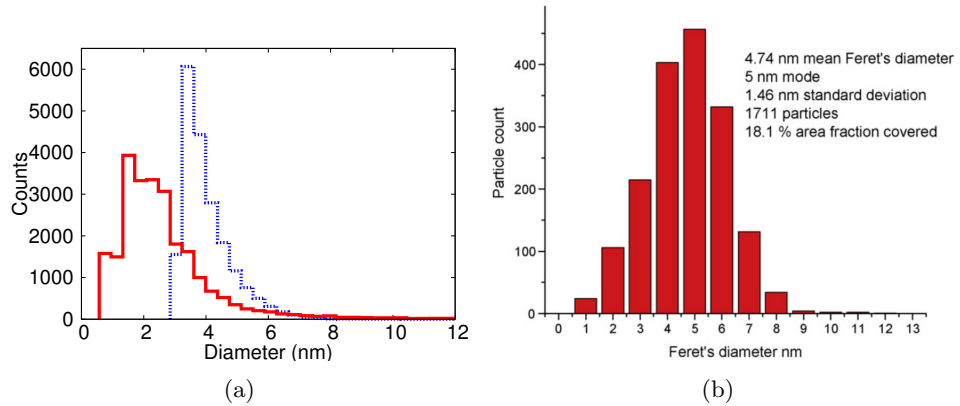
Figure 4.4:   (a) Diameter distribution for Ag ($r_c = 1.67$nm): bubbles in blue (dashed) and droplets in red (solid). (b) Experimental diameter distribution of pure metallic Ag nanoparticles, reprinted with permission from [36] © 2008 Elsevier B.V. All rights reserved.

due to in-flight interactions and shape arrangement after attachment on the substrate, but the general outcome of this measurement is the observation of a large relative abundance of nanometer-sized particles, in line with our simulation.

A more interesting result can be shown if the volume distribution of the liquid nanodroplets is displayed in a log–log histogram. The 3D liquid droplet size distribution obtained through our algorithm (see Figure 4.5(a)) is in good agreement with a power law $f(N) \propto N^{-a}$ where N is the number of atoms per nanodroplet and the exponent a has been estimated as 1.9. The power law has been observed in a quite wide range, between 300 and 10000 atoms per droplet. Very recently, a molecular dynamics (MD) simulation of an aluminum target irradiated with a 100 fs laser pulse has obtained a detailed result of the size distribution of the ablated atomic clusters [37]. A power law behavior is observed, with different slopes in different size ranges: in particular, in the same range studied by our MC method, the exponent emerging from the MD simulation is $a \approx 1.43$, not much different from ours.

In Table 4.4 we summarize some significant results of our model, in a nanosecond timescale: the estimated temperature ratio for phase explosion, the critical radius calculated at T_{pe}, the number of atoms per nanodroplet for peak-size clusters (r_{peak}) and the vapor/liquid atomic ratio N_v/N_l, which expresses the final relative composition of the ablated material. Here we can see that, for the studied metals, N_v/N_l falls between 30% and 45%. These estimations are in qualitative agreement with experimental measurements: a recent paper [38], which deals with femtosecond laser ablation of copper and gold pure targets in vacuum, reports experimental measurements of
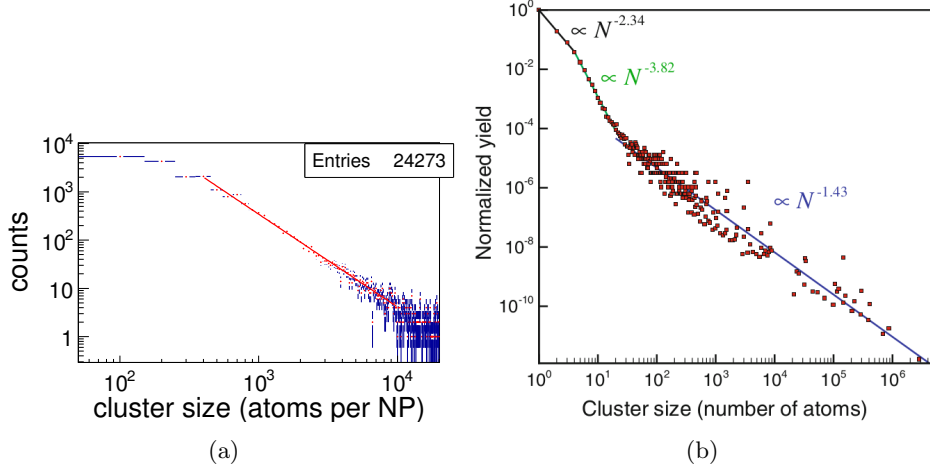
Figure 4.5: Volume distribution of the nanodroplets: (a) our method, liquid Al NPs; (b) MD simulation on Al, reprinted with permission from [37] © Springer–Verlag, 2013. Horizontal blue lines in panel (a) indicate the bin width, while vertical blue lines are error bars, taken as the square root of the count.

Metal	T_{pe}/T_c	r_c (nm)	N_{atom}/clust.	N_v/N_l
Al	0.91	1.76	145	0.29
Fe	0.92	1.57	114	0.38
Co	0.93	1.54	97	0.41
Ni	0.92	1.42	118	0.33
Cu	0.92	1.49	135	0.31
Ag	0.91	1.67	128	0.32
Au	0.91	1.66	127	0.31

Table 4.4: Parameters estimated at T_{pe}.

the vapor/total number ratio in the ablated plume. The measurement is based on emission intensities integrated over all the plume volume and were performed at different laser fluences. In particular, at high laser fluences (some J/cm^2) the estimation of $\frac{N_v}{N_{\mathrm{tot}}} \approx \frac{I_{\mathrm{atoms}}}{I_{\mathrm{tot}}}$ is almost constant, with values of about 40% for copper and 8% for gold. These values correspond to $\frac{N_v}{N_l} \approx$ 0.69 for copper and $\frac{N_v}{N_l} \approx 0.09$ for gold. It has to be noted that our presented algorithm is specifically designed to give information only about the phase explosion mechanism, while of course the experimental values may be the product of several concurrent phenomena, such as vaporization alone or spallation.

4.6 Conclusions

In this chapter, we showed the first promising results of a thermodynamic modeling of the phase explosion process in metastable liquid metals. We performed our calculations for seven different transition metals that are frequently used in laser ablation experiments, to show the generality of our results. The phase explosion conditions have been discussed, in particular focusing on nanosecond pulse regime.

Our model was able to describe many aspects of the liquid nanodroplets directly produced in the external layers of the target through phase explosion mechanism. In particular, we studied the size distribution of the produced liquid nanodroplets, which give rise to a significant fraction of the ablated material. The size distribution function of nanodroplets was found to fit with a power law in the range between 300 and 10000 atoms per nanodroplet. Moreover, the experimental observation of nanometer-sized particles in laser ablation of pure metals can be attributed to solidification of liquid nanodroplets formed through phase explosion mechanism.

The study presented in this chapter was the starting point for further developments. In particular, in the following Chapter 5, the description of the nucleation process will be improved by introducing more complicated aspects of the growth dynamics of vapor bubbles. Moreover, we will consider more realistic assumptions in our simulations, taking into account a temperature gradient inside the target and a time dependence.

References for Chapter 4

[1] A. Miotello and N. Patel. "Nano-cluster Assembled Films, Produced by Pulsed Laser Deposition, for Catalysis and the Photocatalysis". In: *Lasers in Materials Science*. Ed. by M. Castillejo, P. M. Ossi, and L. Zhigilei. Springer, 2014, pp. 213–225. DOI: 10.1007/978-3-319-02898-9_9.

[2] V. Amendola and M. Meneghetti. "What controls the composition and the structure of nanomaterials generated by laser ablation in liquid solution?" In: *Phys. Chem. Chem. Phys.* 15 (2013), p. 3027. DOI: 10.1039/C2CP42895D.

[3] V. Amendola and S. Barcikowski. "A quarter-century of nanoparticle generation by lasers in liquids: Where are we now, and what's next?" In: *J. Colloid Interface Sci.* 489 (2017), pp. 1–2. DOI: 10.1016/j.jcis.2016.12.016.

[4] R. Kelly and A. Miotello. "Contribution of vaporization and boiling to thermal-spike sputtering by ions or laser pulses". In: *Phys. Rev. E* 60.3 (1999), pp. 2616–2625. DOI: 10.1103/PhysRevE.60.2616.

[5]   L. V. Zhigilei, Z. Lin, and D. S. Ivanov. "Atomistic Modeling of Short Pulse Laser Ablation of Metals: Connections between Melting, Spallation, and Phase Explosion". In: *J. Phys. Chem. C* 113 (2009), pp. 11892–11906. DOI: 10.1021/jp902294m.

[6]   C. Porneala and D. A. Willis. "Time-resolved dynamics of nanosecond laser-induced phase explosion". In: *J. Phys. D: Appl. Phys.* 42 (2009), p. 155503. DOI: 10.1088/0022-3727/42/15/155503.

[7]   M. M. Martynyuk. "Phase explosion of a metastable fluid". In: *Comb. Exp. Shock Waves* 13.2 (1977), pp. 178–191. DOI: 10.1007/BF00754998.

[8]   R. Kelly and A. Miotello. "Comments on explosive mechanisms of laser sputtering". In: *Appl. Surf. Sci.* 96–98 (1996), pp. 205–215. DOI: 10.1016/0169-4332(95)00481-5.

[9]   N. M. Bulgakova and A. V. Bulgakov. "Pulsed laser ablation of solids: Transition from normal vaporization to phase explosion". In: *Appl. Phys. A* 73 (2001), pp. 199–208. DOI: 10.1007/s003390000686.

[10]   S. Blairs and M. H. Abbasi. "Correlation between surface tension and critical temperatures of liquid metals". In: *J. Colloid Interface Sci.* 304 (2006), pp. 549–553. DOI: 10.1016/j.jcis.2006.07.072.

[11]   D. R. Lide, ed. *CRC Handbook of Chemistry and Physics.* 90Th. Taylor and Francis, 2010.

[12]   B. J. Keene. "Review of data for the surface tension of pure metals". In: *Int. Mater. Rev.* 38.4 (1993), p. 157. DOI: 10.1179/imr.1993.38.4.157.

[13]   H. M. Lu and Q. Jiang. "Surface Tension and Its Temperature Coefficient for Liquid Metals". In: *J. Phys. Chem. B* 109 (2005), pp. 15463–15468. DOI: 10.1021/jp0516341.

[14]   K. Hornung. "Liquid metal coexistence properties from corresponding states and third law". In: *J. Appl. Phys.* 46 (1975), p. 2548. DOI: 10.1063/1.321932.

[15]   J. Wang and M. A. Anisimov. "Nature of vapor-liquid asymmetry in fluid criticality". In: *Phys. Rev. E* 75 (2007), p. 051107. DOI: 10.1103/PhysRevE.75.051107.

[16]   S. Jungst, B. Knuth, and F. Hensel. "Observation of Singular Diameters in the Coexistence Curves of Metals". In: *Phys. Rev. Lett.* 55.20 (1985), p. 2160. DOI: 10.1103/PhysRevLett.55.2160.

[17]   J. K. Singh, J. Adhikari, and S. K. Kwak. "Vapor-liquid phase coexistence curves for Morse fluids". In: *Fluid Phase Equilib.* 248 (2006), pp. 1–6. DOI: 10.1016/j.fluid.2006.07.010.

[18] E. M. Apfelbaum. "The calculation of vapor-liquid coexistence curve of Morse fluid: Application to iron". In: *J. Chem. Phys.* 134 (2011), p. 194506. DOI: 10.1063/1.3590201.

[19] G. R. Gathers. "Thermophysical properties of liquid copper and aluminum". In: *Int. J. Thermophys.* 4.3 (1983), p. 209. DOI: 10.1007/BF00502353.

[20] R. S. Hixson, M. A. Winkler, and M. L. Hodgdon. "Sound speed and thermophysical properties of liquid iron and nickel". In: *Phys. Rev. B* 42.10 (1990), p. 6485. DOI: 10.1103/PhysRevB.42.6485.

[21] H. Hess, E. Kaschnitz, and G. Pottlacher. "Thermophysical properties of liquid cobalt". In: *High Pressure Research* 12.1 (1994), pp. 29–42. DOI: 10.1080/08957959408201653.

[22] M. H. Mousazadeh and M. G. Marageh. "A perturbed Lennard-Jones chain equation of state for liquid metals". In: *J. Phys.: Condens. Matter* 18 (2006), p. 4793. DOI: 10.1088/0953-8984/18/20/003.

[23] K. M. Watson. "Thermodynamics of the Liquid State". In: *Ind. Eng. Chem.* 35 (1943), p. 398. DOI: 10.1021/ie50400a004.

[24] D. S. Viswanath and N. R. Kuloor. "On Latent Heat of Vaporization, Surface Tension, and Temperature". In: *J. Chem. Eng. Data* 11.1 (1966), p. 69. DOI: 10.1021/je60028a020.

[25] S. Velasco et al. "Prediction of the enthalpy of vaporization of metals and metalloids". In: *Fluid Phase Equilib.* 244 (2006), pp. 11–15. DOI: 10.1016/j.fluid.2006.03.017.

[26] E. A. Guggenheim. "The Principle of Corresponding States". In: *J. Chem. Phys.* 13 (1945), p. 253. DOI: 10.1063/1.1724033.

[27] A. Grossman, R. P. Doerner, and S. Luckhardt. "Surface tension enhancement of TRIM sputtering yields for liquid metal targets". In: *J. Nucl. Mater.* 290–293 (2001), pp. 80–84. DOI: 10.1016/S0022-3115(00)00616-4.

[28] D. Kashchiev. "Thermodynamically consistent description of the work to form a nucleus of any size". In: *J. Chem. Phys.* 118 (2003), p. 1837. DOI: 10.1063/1.1531614.

[29] P. G. Debenedetti. *Metastable Liquids Concepts and Principles*. Princeton University Press, 1996.

[30] S. I. Anisimov. "Vaporization of metal absorbing laser radiation". In: *Sov. Phys. JETP* 27.1 (1968), pp. 182–183.

[31] C. J. Knight. "Theoretical Modeling of Rapid Surface Vaporization with Back Pressure". In: *AIAA JOURNAL* 17.5 (1979), p. 519. DOI: 10.2514/3.61164.

[32] W. Döring. "Die Ueberhitzungsgrenze und Zereissfestigkeit von Fluessigkeiten". In: *Z. Phys. Chem.* 36 (1937), p. 371.

[33] M. Volmer. *Kinetics of phase formation.* Air Force Cambridge Reasarch Center, Geophysics Research Division, Atmospheric Physics Laboratory, 1940.

[34] V. P. Skripov. *Metastable liquids.* Wiley, 1974.

[35] R. D. Torres et al. "Mechanisms of Resonant Infrared Matrix-Assisted Pulsed Laser Evaporation". In: *Crit. Rev. Solid State Mater. Sci.* 36 (2011), pp. 16–45. DOI: 10.1080/10408436.2011.547761.

[36] J. C. Alonso et al. "Thin films of silver nanoparticles deposited in vacuum by pulsed laser ablation using a YAG:Nd laser". In: *Appl. Surf. Sci.* 255 (2009), pp. 4933–4937. DOI: 10.1016/j.apsusc.2008.12.040.

[37] C. Wu and L. V. Zhigilei. "Microscopic mechanisms of laser spallation and ablation of metal targets from large-scale molecular dynamics simulations". In: *Appl. Phys. A* 114 (2014), p. 11. DOI: 10.1007/s00339-013-8086-4.

[38] J. Hermann et al. "Correlation between Ablation Efficiency and Nanoparticle Generation during the Short-Pulse Laser Ablation of Metals". In: *Laser Physics* 18.4 (2008), pp. 374–379. DOI: 10.1134/s11490-008-4002-6.

60

Chapter 5

Dynamic simulation of liquid nanodroplet formation in PLD

Preview   The model presented in Chapter 4 directly links the theory of homogeneous nucleation to the size distribution of the liquid nanodroplets that are formed in the phase explosion of metals. To that aim, we considered a simplified computational method which assumed a constant temperature of the target.

Here, we discuss an improved computational approach that removed some of the previous simplifying assumptions. In particular, in § 5.1 we face the issue of single spherical vapor bubble growth as function of time in a uniform superheated metal. Moreover, in § 5.2 we consider thermal processes occurring at the target surface under nanosecond laser irradiation.

Our improved computational approach allows us to describe the formation of liquid nanodroplets through the phase explosion mechanism, with temporal and spatial resolution. In § 5.3 we present the results of dynamic simulations of phase explosion performed on aluminum. The phase composition of the ejected material is studied as a function of time during a laser pulse and the size distribution of the produced aluminum nanodroplets is reported.

The content of this chapter was adapted from:

1. A. Mazzi, F. Gorrini and A. Miotello, Appl. Surf. Sci. (2016),
   http://dx.doi.org/10.1016/j.apsusc.2016.09.006
   © 2016 Elsevier B.V. All rights reserved.

2. A. Mazzi and A. Miotello, J. Colloid Interface Sci. 489 (2017) 126–130.
   © 2016 Elsevier Inc. All rights reserved.

5.1 Dynamics of vapor bubble nucleation

Remarks on the thermodynamics of liquid metals

The main thermodynamic quantities of liquid metals in the deep metastable regime were estimated by using semi-empirical scaling laws consistent with the theory of critical exponents, as discussed in detail in § 4.2. Here, in addition to the thermodynamic quantities already considered, we also need a quantitative estimation of the thermal conductivity K and isobaric specific heat capacity $c_{p,l}$, both of which depend on the temperature of the liquid metal.

To find a reliable temperature-dependent expression for the thermal conductivity of metastable liquid metals, we first considered the Wiedemann–Franz law, which establishes the relation between the thermal conductivity and the electrical conductivity and which was proven to be valid for Fermi liquids up to the metal–insulator transition [1]:

$$\frac{K_e}{\sigma_{\mathrm{el}}T} = \frac{\pi^2 k_B^2}{3e^2} = L,\tag{5.1}$$

where K_e is the electron contribution to the thermal conductivity, σ_{el} is the electrical conductivity, and $L = 2.44 \times 10^{-8}$ WΩK^{-2} is known as the Lorentz number. Then, we adopted the model proposed by Korobenko et al. [2] for the electrical conductivity of liquid metals at high temperatures, based on the Drude–Sommerfeld free electron model. Finally, we assumed the thermal conductivity of liquid metals to be entirely due to the electron contribution, so that $K \approx LT\sigma_{\mathrm{el}}$. The effective valence z_{ion}, used in this model to relate the electron and ion number density ($n_e = z_{\mathrm{ion}}n_i$), was taken as reported in Table 5.1.

Provided that the critical behavior of the specific heat capacity at constant volume c_v is described by the universal law with the critical exponent $\alpha \approx 0.1$, the temperature dependence of the isobaric specific heat capacity of the liquid phase $c_{p,l}$ was approximated by a semi-empirical rule [3]:

$$c_{p,l}(T) = c_{p,l}(T_m) \left(\frac{\Delta T}{\Delta T_m} \right)^{-0.24}.\tag{5.2}$$

The main parameters used for the estimation of the thermophysical quantities are summarized in Table 5.1.

Homogeneous vapor bubble nucleation

If we assume that the vapor bubbles nucleated in the metastable liquid are spherical, we can calculate the critical radius of the vapor bubbles r_c (i.e. the vapor bubbles that are in labile equilibrium with the liquid phase) through the classical expression of Eq. (4.7).

Metal	T_c	ρ_c	p_c	σ_m	$\Delta h_v\,(T_b)$	z_{ion}	$c_{p,l}\,(T_m)$
	(K)	(kg/m^3)	(10^8 Pa)	(N/m)	(kJ/mol)		(J/kgK)
Al	6319	634	3.2	1.05	294	3.0	1070
Fe	8059	1467	5.4	1.909	355	1.21	815
Co	7710	1350	5.4	1.928	375	0.99	780
Ni	7241	2159	6.5	1.834	378	0.95	723
Cu	5741	2363	4.6	1.374	300	1.21	532
Ag	5851	2718	3.3	0.955	255	1.0	260
Au	7003	5066	3.9	1.162	324	1.0	157

Table 5.1: Parameters used for the thermodynamic modeling: temperature, density and pressure at the thermodynamic critical point [4] (T_c, ρ_c and p_c), surface tension at the melting point σ_m [5], enthalpy of vaporization at the boiling point $\Delta h_v\,(T_b)$ [6, 7], effective valence z_{ion} [8] and isobaric specific heat capacity of the liquid phase at the melting point $c_{p,l}\,(T_m)$ [9–13].

In the following, we will consider the temperature time evolution of the laser-irradiated metal. In this context, in principle, we cannot assume a steady homogeneous nucleation process, since the nucleation rate calculated as in Eq. (4.9) can only be attained asymptotically. Under the fast thermal processes that occur in the pulsed laser heating of metals, in general, the characteristic time lag of attainment of the steady-state nucleation should be taken into account. This time lag is usually expressed as [14]:

$$\tau_{\text{lag}} = \sqrt{\frac{2\pi m}{k_B T}} \frac{4\pi\sigma p_v}{\left(p_v - p_l\right)^2}. \tag{5.3}$$

The effective nucleation frequency, J^*, can be found by solving the following differential equation [15] for a given time evolution of the liquid temperature:

$$\frac{dJ^*}{dt} + \tau_{\text{lag}}^{-1} J^* = \tau_{\text{lag}}^{-1} J_s. \tag{5.4}$$

If we assume as a simplifying hypothesis that the liquid temperature is constantly increasing, with an arbitrary time derivative dT/dt, we can solve numerically Eq. (5.4) as shown in Figure 5.1.

Single bubble expansion in superheated liquid metal

The dynamics of a single vapor bubble in a homogeneous liquid metal was studied by adopting the model developed by Lee and Merte [16] for water, sodium and other low T_b substances. This approach includes the influences of surface tension, liquid inertia and heat diffusion and consists of the following
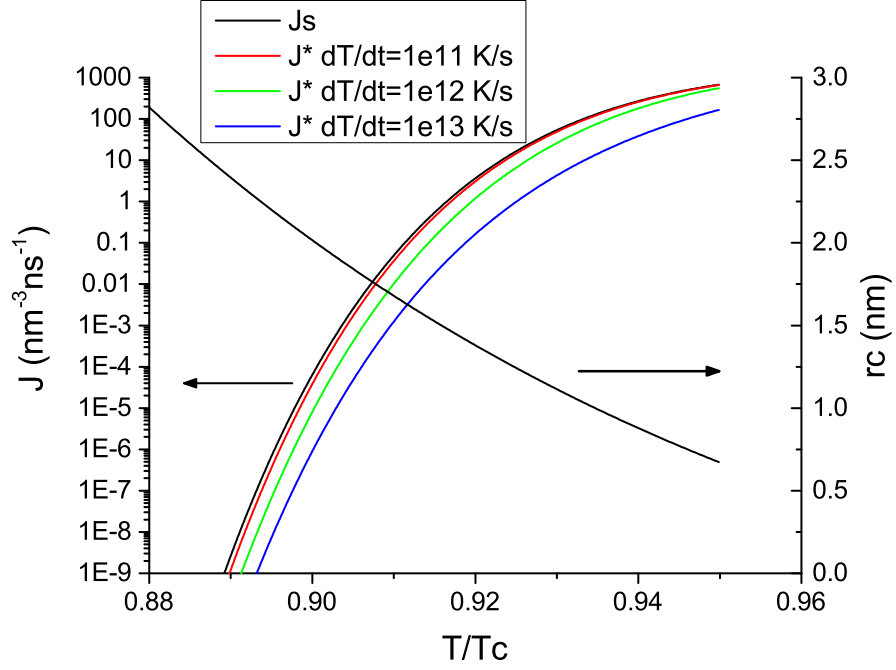
Figure 5.1: Vapor bubble nucleation frequency in both steady and unsteady cases for aluminum. Three different constant heating rates were considered. On the right axis, the critical radius is reported in the same temperature range.

coupled equations:

$$\begin{cases} R\dfrac{d^2R}{dt^2} + \dfrac{3}{2}\left(\dfrac{dR}{dt}\right)^2 = \\[2ex] \qquad = \dfrac{P_v(T) - P_\infty}{\epsilon\rho_l} - \dfrac{2\sigma(T)}{\epsilon\rho_l R} - 4\dfrac{\mu}{\epsilon\rho_l R}\dfrac{dR}{dt} \hspace{2em} (5.5\text{a}) \\[3ex] \dfrac{\partial T}{\partial t} + \epsilon\dfrac{R^2}{r^2}\dfrac{dR}{dt}\dfrac{\partial T}{\partial r} = \dfrac{K}{\rho_l c_{p,l}}\left(\dfrac{\partial^2 T}{\partial r^2} + \dfrac{2}{r}\dfrac{\partial T}{\partial r}\right). \hspace{1.5em} (5.5\text{b}) \end{cases}$$

Eq. (5.5a) is the equation of expansion, where R is the bubble radius, $\epsilon = 1 - \rho_v/\rho_l$ and μ is the dynamic viscosity defined as:

$$\mu = \frac{1}{3}\left(\frac{2\sigma K}{\pi\rho_l c_{p,l}}\right)^{\frac{1}{2}} \rho_v \frac{\Delta h_v}{K}(T_\infty - T_{\text{sat}})^{-1}$$
$$\times \{\rho_v[p_v(T_\infty) - p_\infty]\}^{-\frac{1}{4}}. \hspace{2em} (5.6)$$

Here T_∞ and p_∞ are referred to the far field, while T_{sat} is the saturation temperature corresponding to p_∞. On the other hand, Eq. (5.5b) is the

heat diffusion equation expressed in spherical coordinates and r is intended as the radial variable, in principle ranging from R to ∞.

The initial conditions are $R(t=0) = R_c$, $\dot{R}(t=0) = 0$ and $T(r,0) = T_\infty$. The boundary conditions are fixed by $T(\infty,t) = T_\infty(t)$ for the far field and by

$$\left(\frac{\partial T}{\partial r}\right)_R = \frac{\Delta h_v}{3K}\frac{1}{R^2}\frac{d}{dt}\left(R^3\rho_v\right) \tag{5.7}$$

at the bubble boundary.

Eq. (5.5a) is solved by means of a fourth order Runge–Kutta method (see [17] for reference) whose steps are alternated with the solution of the energy equation, which proceeds through the Forward Time Centered Space algorithm (FTCS). In our case, Eq. (5.5b) is a nonlinear equation, since the thermal diffusivity $\alpha_{\mathrm{th}} = K/\left(\rho_l c_{p,l}\right)$ depends on the temperature. The problem was solved with a regular spatial discretization (spatial index j) and a variable time step, which was chosen to satisfy the following requirement for the convergence of the FTCS algorithm [17]:

$$dt \leq \min_j \frac{dr^2}{2\alpha_{\mathrm{th},j}}. \tag{5.8}$$

While in the original work of Lee and Merte an arbitrary disturbance was imposed to initiate the bubble growth, in our study we assumed a constant heating rate, so that the nucleated bubble spontaneously exits from the metastability, since the critical radius monotonically decreases with the temperature. This problem was solved for the seven metals considered in this chapter, by assuming a constant heating rate of either 10^{11} K/s or 10^{12} K/s and an initial temperature at bubble nucleation in the range $[0.88, 0.93]\,T_c$. A typical solution obtained for aluminum is reported in Figure 5.2.

We can see in Figure 5.2 that the bubble expansion with heating at 10^{12} K/s becomes effective between 50 and 100 ps. This characteristic time has to be compared with the time duration of the phase explosion process, which is of about 80 ps at the same heating rate (see Figure 5.3). Figure 5.2 reports the mathematical solution of the system of equations describing single vapor bubble expansion in a homogeneous liquid, but it is physically meaningful only when bubble–bubble interactions are negligible and in any case within the metastable liquid lifetime.

Time resolved homogeneous nucleation

In order to study the relevance of τ_{lag} in the time regime of our interest, we simulated the homogeneous nucleation of vapor bubbles in a liquid metal whose temperature is increasing with an arbitrary constant heating rate $dT/dt = 10^{11}$ K/s or $dT/dt = 10^{12}$ K/s. These values were selected as the typical orders of magnitude in the case of nanosecond laser heating of metals.
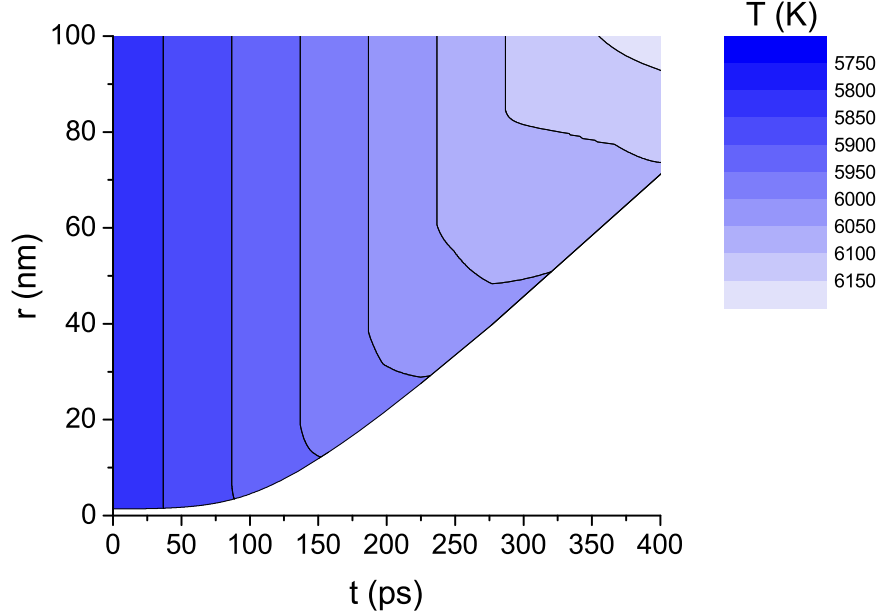
Figure 5.2: Single vapor bubble expansion in Al. The edge of the white region represents the time evolution of the bubble radius $R(t)$. The contour plot shows $T(r, t)$ in the liquid phase in the bubble neighborhood.

We developed a time-discretized Monte Carlo (MC) algorithm to simulate vapor bubble nucleation in a homogeneous metallic cubic system of volume $V = (100 \text{ nm})^3$. The system volume is fixed during the simulation, while vapor bubble nucleation/expansion cause a concentric distancing of the other bubbles away from the center of the nucleated/expanded bubble, according to the difference between the liquid and vapor density; in this way some peripheral bubbles can leave the cubic system and they are neglected in the following.

No temperature gradients were considered, to simplify the computation. An analytical approximation of the solutions of single vapor bubble expansion, obtained as discussed above, was included in the nucleation method in order to model the bubble dynamics. In this way, at each time step dt (of the order of 1 ps), a number $dN = J^*V_l dt$ of new bubbles is randomly generated in the residual liquid volume V_l and all the existing bubbles expand. When two bubbles get in touch, their growth is arrested. The nucleation continues up to a maximum vapor volume fraction $\eta_{\max} = V_v/V_{\text{tot}}$, which was of about 0.30, a value that corresponds to a highly connected random bubble distribution, giving rise to percolation paths of connected bubbles in the liquid.

The time scale was arbitrarily arranged so that $T(t)/t = dT/dt$ to allow
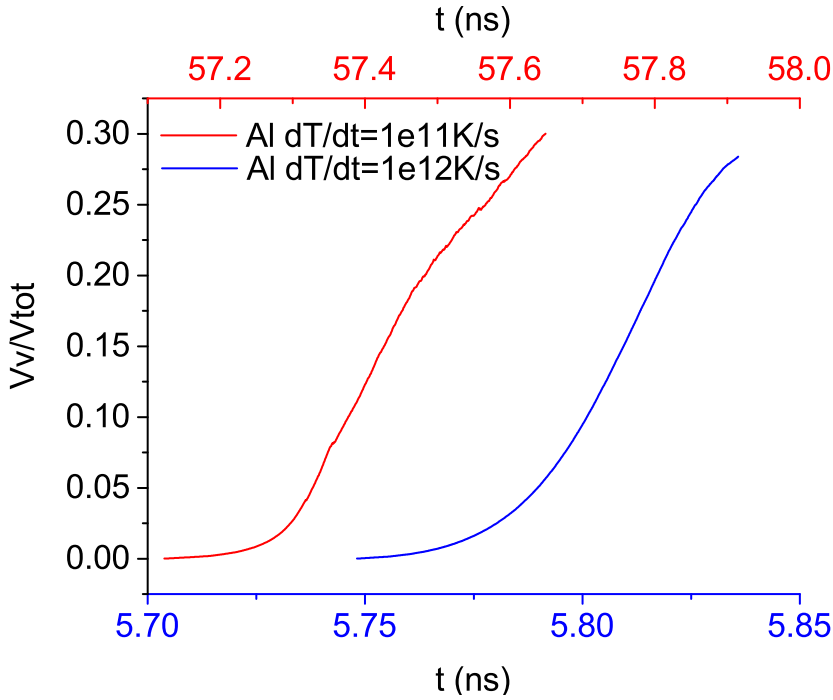
Figure 5.3: Vapor volume fraction in aluminum under constant heating at $dT/dt = 10^{11}$ K/s (red curve, top axis) and $dT/dt = 10^{12}$ K/s (blue curve, bottom axis).

an intuitive time–temperature relation. The MC algorithm of bubble nucleation starts at the melting point T_m of the substance (at $t_0 = T_m dt/dT$) and continues up to a vapor volume fraction of about 0.30, which is usually reached at $T \approx 0.92T_c$.

In Figure 5.3 we show the time dependence of the vapor volume fraction in case of homogeneous nucleation under constant heating. This plot proves that homogeneous nucleation occurs in a very small time interval, of the order of 80÷500 ps, which corresponds to a temperature interval of 50÷80 K. This fast nucleation process takes place without a significant time delay, even if an unsteady nucleation model was chosen. In particular we can observe that by increasing the heating rate of an order of magnitude, the initiation of bubble generation is anticipated by an order of magnitude as it is expected without considering τ_{lag}.

The results presented in this section constitute two important elements in the design of the dynamic simulation described in the following. In particular, the single vapor bubble dynamics studied above was included in the simulation of phase explosion, providing a more realistic description of the generation of a dense vapor bubble distribution. Moreover, the study of the timing of homogeneous nucleation allowed us to consider a steady-state

nucleation model in the simulation of nanosecond laser ablation.

5.2 Thermal processes in the nanosecond laser ablation of aluminum

Heat diffusion problem

In this chapter, we consider as sample target a rectangular cuboid, with a square section of 100 nm side and an extension of 10 μm along the z axis, normal to the target surface. We assume the lateral size of the system to be small compared to the lateral temperature gradients, so that the temperature only depends on the distance from the outer surface. The space–time resolved simulations were performed on aluminum.

With this hypothesis, we numerically solved the 1D heat diffusion problem expressed by the nonlinear partial differential equation:

$$\frac{\partial T}{\partial t} = \frac{\partial T}{\partial z}\left(\alpha_{\text{th}}\frac{\partial T}{\partial z}\right) + S(z,t), \tag{5.9}$$

where α_{th} is the thermal diffusivity and $S(z,t)$ represents the heat source term. Since our interest was just to study the ablation dynamics in a time evolving medium with physically reasonable spatial gradients, we considered the following simplifying assumptions: (1) the initial temperature is the melting point $T_0 = T_m$, (2) the heat source term has Gaussian time-dependence and an exponential spatial dependence following the Beer–Lambert law with a fixed absorption depth $\delta = 20$ nm[18]. The pulse duration was taken as 20 ns FWHM.

Eq. (5.9) was solved using the boundary conditions $T_\infty = T_m$ for the far field and $K\left.\frac{\partial T}{\partial z}\right|_{z=z_0} = \rho c_{p,l}S(z_0)\delta - \rho u_l \Delta h_v$ at the liquid free surface z_0, which was taken as the origin of z axis. Here, u_l is the surface recession velocity due to vaporization, calculated as described in the following paragraph.

The heat equation was numerically solved through a Forward Time Centered Space (FTCS)[17] algorithm using a non-uniform 1D grid with 140 spatial elements with size increasing with the cubic power, while moving inwards. The size of the time increments was determined step by step in order to satisfy the convergence of the FTCS algorithm:

$$dt \leq \min_j \frac{dz_j^2}{2\alpha_j}, \tag{5.10}$$

where j is the spatial index. The typical temperature evolution during a laser pulse is presented in Figure 5.4 in the case of laser fluence $F = 3$ J/cm^2.

Vaporization

The vaporization process was modeled according to the work of Kelly [19], by considering the evolution of the vaporized material from the Knudsen layer (KL), where the vapor atoms thermalize, to the UAE that leads the sputtered material away from the target. That method assumes the flow velocity at the boundary of the KL to be equal to the speed of sound:

$$u_K \approx \left(\frac{\gamma k_B T_K}{m} \right)^{1/2} = \left(\frac{5 k_B T_K}{3m} \right)^{1/2}, \qquad (5.11)$$

where the subscript K refers to the KL outer boundary and the heat capacity ratio is assumed to be $\gamma = 5/3$. Moreover, the temperature and density jump across the KL is given by:

$$T_K = 0.669 T_s, \quad \rho_K = 0.308 \rho_s, \qquad (5.12)$$

where T_s is the liquid surface temperature while ρ_s indicates the saturated vapor density at T_s. This model of vaporization is consistent with the numerical results of Knight [20] and allows an estimate of the surface recession velocity of the liquid surface u_l by simply applying the conservation relation $\rho_l u_l = \rho_K u_K$.

Finally, we assumed the recoil pressure on the liquid exerted by the vaporized material to be $p_l = 0.55 p_s(T_s)$ in the case of intense vaporization [20, 21] as we did in Chapter 4.

Computational framework and phase explosion

The temperature and the thermodynamic quantities were considered uniform within each discrete layer. The solution of the heat equation proceeded together with the calculation of the vaporization rate from the surface, given by the surface recession velocity discussed above. In the light of the discussion of § 5.1, here we assumed steady homogeneous nucleation. In particular, the nucleation rate was calculated in each layer at any time through the steady nucleation formula of Eq. (4.9) and, when it was not zero in the considered layer volume, the bubbles were randomly generated, initially with the critical size [4].

When the full depth of a layer was vaporized or when the volume fraction occupied by the vapor bubbles reached the maximum value $\eta_{\max}$, the layer was removed and the relative amount of vapor and liquid was computed as atomic percentage. As a result, we can estimate the relative ablation rate of vapor and liquid nanodroplets as a function of time, during a laser pulse.

At the end of the simulations, the distribution of the nucleated vapor bubbles over all the target depth was taken as a whole and the residual liquid inter-volumes were identified through the MC algorithm described in Chapter 4.
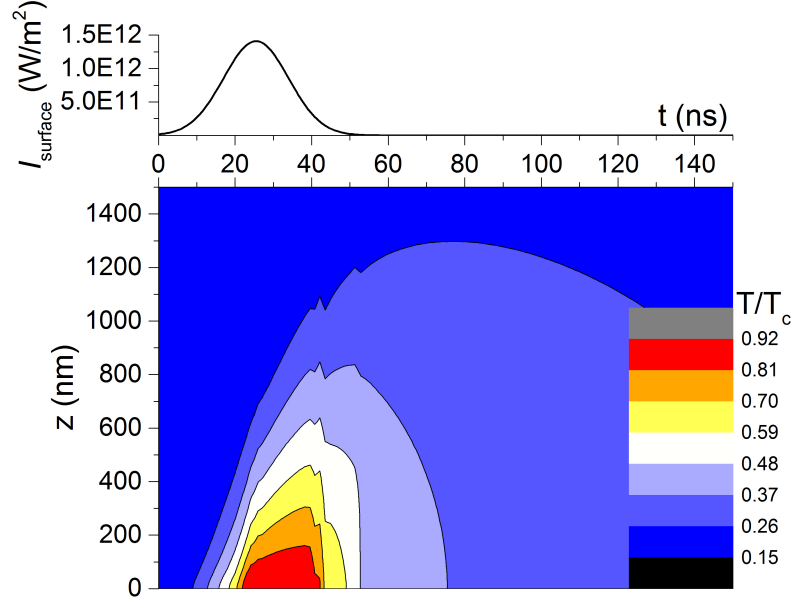
Figure 5.4:   Time dependence of the incoming power density and contour plot of the temperature of liquid Al as a function of time and depth obtained in the case of laser fluence of 3 J/cm^2.

5.3   Results and discussion

The laser ablation simulation described above was executed with different energy fluences, ranging from 1.5 J/cm^2 to 4 J/cm^2, with the thermophysical parameters of aluminum.

In order to give the relevant orders of magnitude that emerge from our numerical solution of the heat diffusion equation (5.9), here we report the maximum space and time derivatives of the temperature. In the case of $F = 4$ J/cm^2, which gives the most extreme heating among our simulations, we found $\partial_z T \lesssim 10^{10}$ K/m and $\partial_t T \lesssim 4 \times 10^{11}$ K/s evaluated at the target surface. In particular, the order of magnitude of the time derivative allows us to consider the steady-state nucleation model discussed above.

Homogeneous nucleation was found to be detectable at temperature larger than $0.90 T_c$, as it is widely accepted in literature. In this way, we can have an idea of the space–time evolution of the nucleation process by looking at the temperature color map reported in Figure 5.4.

The nucleation–vaporization method described in § 5.2 was used to calculate the total ablation yield, which was reported in the inset of Figure 5.5 as a function of the energy density absorbed by the target.

From Figure 5.5 we can observe how the vapor–nanoparticle mixture
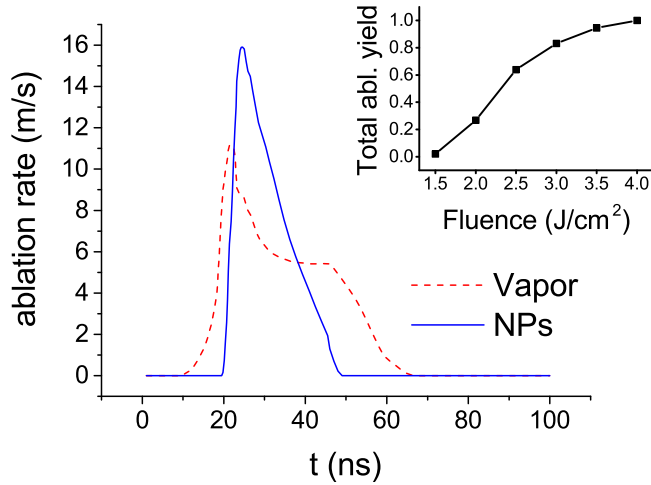
Figure 5.5: Ablation rate calculated for vapor (dashed, red) and nanodroplets (solid, blue), expressed as surface recession velocity. The data obtained at $F = 3.5$ J/cm^2 are reported as a function of time. Inset: total ablation yield normalized to the value obtained at the maximum investigated fluence (4 J/cm^2).

is generated as a function of time in our simulation. As we can expect, homogeneous nucleation occurs promptly during the laser pulse and in this way the liquid NPs are emitted through the phase explosion process. Indeed, as discussed in § 5.1, the phase explosion process only takes a fraction of nanosecond in a liquid metal that is led at $T \gtrsim 0.90 T_c$ through a nanosecond heating process.

In the case shown in Figure 5.5 ($F = 3.5$ J/cm^2) the nanodroplet formation process continues for several nanoseconds, during flattop surface heating, and in this way some surface layers are sequentially removed. On the other hand, the vaporization process occurs in a significantly broader temperature range, and correspondingly in a larger time interval.

As in Chapter 4, the size distribution of the liquid nanodroplets formed in the phase explosion process was derived. Only the liquid layers with fully established nucleation ($\eta \approx \eta_{max}$) were taken into account in this plot. Here we can see the droplet size histogram in a log–log plot (Fig. 5.6), which shows a power scaling law for particles containing $10^3 \div 10^4$ atoms. The power law distribution in this case can be expressed as $f(N) \propto N^{-2.05}$, where N is the number of atoms per cluster. Interestingly, the exponent seems to be quite independent on the laser fluence, since the result was the same both in the case of $F = 3.0$ J/cm^2 and $F = 4.0$ J/cm^2.

This rule is consistent with our recent results obtained in the absence of spatial gradients [4] and also with the results of a molecular dynamics
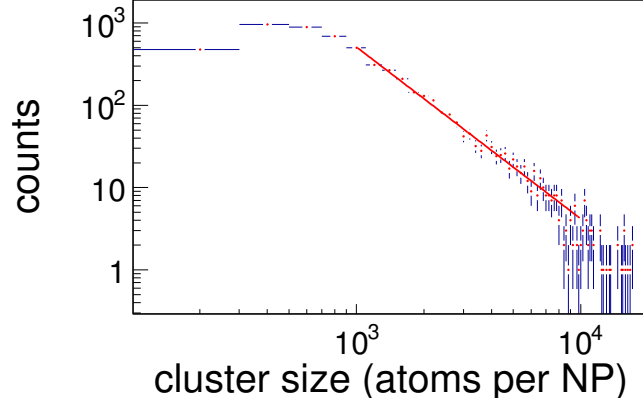
Figure 5.6: Size distribution of the liquid nanodroplets identified in the simulation at $F = 3.0$ J/cm^2. Horizontal blue lines indicate the bin width, while vertical blue lines are error bars, taken as the square root of the count.

approach that described femtosecond laser ablation of aluminum [22].

To our knowledge, there have been some attempts to find an analogous scaling law for the size distribution of the metal NPs deposited through femtosecond laser ablation [23], although with poor statistics. On the other hand, these studies are missing in the case of nanosecond lasers.

In the size distribution of aluminum NPs, both in the case of $F = 3.0$ J/cm^2 and $F = 4.0$ J/cm^2, the average number of atoms per cluster was of about $\bar{N} = 450$ atoms, while the average particle size, calculated as the diameter of a spherical equivalent particle at room temperature[1] was of about $\bar{d} = 3.2$ nm.

This average size of the liquid nanodroplets directly ejected from the target is consistent with the experimental observations of pure metal NPs synthesized by pulsed laser deposition in high vacuum using nanosecond laser pulses [24, 25].

In order to graphically show the spatial 3D distribution of the identified liquid nanodroplets, we report two scatter plots in Figure 5.7 representing the liquid NPs found in the simulations at $F = 2.5$ J/cm^2 and $F = 3$ J/cm^2. In our MC method for liquid inter-volume identification the nanodroplets are reconstructed as clusters of spherical liquid volumes trapped between the nucleated vapor bubbles. Here the spheres belonging to the same cluster are plotted in the same color that depends on the cluster size, calculated as the diameter of an equivalent spherical nanoparticle.

In the frame reported in Figure 5.7 the z axis points outwards from the target surface, which was moved in the negative direction during the simulation due to vaporization and phase explosion. In this way, the droplets

---

[1]solid density of Al at room temperature $\rho_s = 2.7$ kg/m^3.
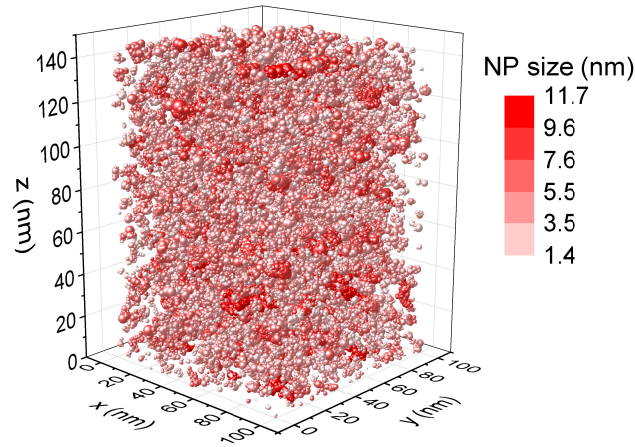
Figure 5.7: Liquid nanodroplets 3D distribution obtained in the simulation at $F = 3$ J/cm^2. The nanodroplets are reported as clusters of spheres. The droplet color depends on the cluster size.

observed at larger z were formed before that at smaller z.

We can see that the larger clusters are formed as non-spherical agglomerates that will eventually evolve to spherical NPs, to minimize the Gibbs free energy, during their flight away from the target or on the substrate.

5.4   Conclusions

In this chapter, we have shown the potentiality of a computational model based on a continuum approach to describe the laser ablation dynamics of metals, focusing on phase explosion. The continuum approximation is allowed in the local thermal equilibrium conditions that are obtained through nanosecond pulse laser heating. On the other hand, in the case of ultrafast laser pulses, the molecular dynamics approach is able to reach very refined results [26].

Our computational method simulates the laser heating of a bulk aluminum target with a 20 ns FWHM laser pulse. By assuming a large spot size compared to the depth involved in the thermal processes, we neglected the temperature gradients in the plane of the target surface and we applied a standard numerical procedure to solve the 1D heat diffusion equation, which provides us the space–time temperature dependence (see Figure 5.4).

Vaporization from the target surface was evaluated through the model of UAE developed by Kelly [19], while the homogeneous nucleation of vapor bubbles in the metastable liquid aluminum was simulated in the framework

of the classical nucleation theory.

The size distribution of the liquid NPs formed in the phase explosion process was found to obey a power law in the range between $10^3 \div 10^4$ atoms per NP. This is essentially in agreement with the results of Chapter 4, although the target inhomogeneity that was considered in the present chapter caused a broader dispersion of the vapor bubble size, thus producing relatively larger liquid nanoclusters, a result more close to the experimental data.

The present study proves that the homogeneous nucleation process leading to phase explosion occurs promptly during nanosecond laser irradiation, without significant time delay (see Figure 5.5). Thus, even if the ablation plume expansion and nanoparticle ejection is sometimes observed with a time delay in the experiments [27, 28], this should be ascribed to hydrodynamic mechanisms rather than to the phase explosion phenomenon itself.

In the future, we would like to study the ejection of larger liquid clusters from the target surface at the late stages of the thermal relaxation [29], by considering the hydrodynamic mechanisms that can occur with significant time delay respect to the laser pulse. Moreover, we want to find a physical criterion for choosing the maximum vapor bubble packing fraction $\eta_{\max}$, which is an important trigger parameter for our simulation of phase explosion.

References for Chapter 5

[1]   Norman Henry March. "Proof of Wiedemann-Franz law up to metal-insulator transition for Fermi liquid model". In: *Liquid Metals*. Cambridge University Press, 1990, pp. 398–400.

[2]   V. N. Korobenko and A. D. Rakhel. "Transition of Expanded Liquid Iron to the Nonmetallic State under Supercritical Pressure". In: *Sov. Phys. JETP* 112.4 (2011), pp. 649–655. DOI: 10.1134/S1063776111020178.

[3]   G. A. Pinhasi, A. Ullmann, and A. Dayan. "1D plane numerical model for boiling liquid expanding vapor explosion (BLEVE)". In: *Int. J. Heat Mass Transfer* 50 (2007), pp. 4780–4795. DOI: 10.1016/j.ijheatmasstransfer.2007.03.016.

[4]   A. Mazzi, F. Gorrini, and A. Miotello. "Liquid nanodroplet formation through phase explosion mechanism in laser-irradiated metal targets". In: *Phys. Rev. E* 92 (2015), 031301–R. DOI: 10.1103/PhysRevE.92.031301.

[5]   B. J. Keene. "Review of data for the surface tension of pure metals". In: *Int. Mater. Rev.* 38.4 (1993), p. 157. DOI: 10.1179/imr.1993.38.4.157.

[6]   D. R. Lide, ed. *CRC Handbook of Chemistry and Physics*. 90Th. Taylor and Francis, 2010.

[7]   H. M. Lu and Q. Jiang. "Surface Tension and Its Temperature Coefficient for Liquid Metals". In: *J. Phys. Chem. B* 109 (2005), pp. 15463–15468. DOI: 10.1021/jp0516341.

[8]   E. Esposito, H. Ehrenreich, and C. D. Gelatt Jr. "Electrical transport in transition-metal liquids and metallic glasses". In: *Phys. Rev. B* 18.8 (1978), pp. 3913–3920. DOI: 10.1103/PhysRevB.18.3913.

[9]   G. R. Gathers. "Thermophysical properties of liquid copper and aluminum". In: *Int. J. Thermophys.* 4.3 (1983), p. 209. DOI: 10.1007/BF00502353.

[10]   R. S. Hixson, M. A. Winkler, and M. L. Hodgdon. "Sound speed and thermophysical properties of liquid iron and nickel". In: *Phys. Rev. B* 42.10 (1990), p. 6485. DOI: 10.1103/PhysRevB.42.6485.

[11]   H. Hess, E. Kaschnitz, and G. Pottlacher. "Thermophysical properties of liquid cobalt". In: *High Pressure Research* 12.1 (1994), pp. 29–42. DOI: 10.1080/08957959408201653.

[12]   C. Cagran, B. Wilthan, and G. Pottlacher. "Enthalpy, heat of fusion and specific electrical resistivity of pure silver, pure copper and the binary Ag-28Cu alloy". In: *Thermochim. Acta* 445 (2006), pp. 104–110. DOI: 10.1016/j.tca.2005.08.014.

[13]   K. Boboridis, G. Pottlacher, and H. Jager. "Determination of the Critical Point of Gold". In: *Int. J. Thermophys.* 20.4 (1999). DOI: 10.1023/A:1022687811410.

[14]   V. P. Skripov. *Metastable liquids*. Wiley, 1974.

[15]   P. G. Debenedetti. *Metastable Liquids Concepts and Principles*. Princeton University Press, 1996.

[16]   H. S. Lee and H. Merte. "Spherical vapor bubble growth in uniformly superheated liquids". In: *Int. J. Heat Mass Transfer* 39.12 (1996), pp. 2427–2447. DOI: 10.1016/0017-9310(95)00342-8.

[17]   William H Press. *Numerical recipes: The art of scientific computing*. 3rd edition. Cambridge University Press, 2007.

[18]   A. Peterlongo, A. Miotello, and R. Kelly. "Laser-pulse sputtering of aluminum: Vaporization, boiling, superheating, and gas-dynamic effects". In: *Phys. Rev. E* 50.6 (1994). DOI: 10.1103/PhysRevE.50.4716.

[19]   R. Kelly. "On the dual role of the Knudsen layer and unsteady, adiabatic expansion in pulse sputtering phenomena". In: *J. Chem. Phys.* 92 (1990), p. 5047. DOI: 10.1063/1.458540.

76

[20] C. J. Knight. "Theoretical Modeling of Rapid Surface Vaporization with Back Pressure". In: *AIAA JOURNAL* 17.5 (1979), p. 519. DOI: 10.2514/3.61164.

[21] S. I. Anisimov. "Vaporization of metal absorbing laser radiation". In: *Sov. Phys. JETP* 27.1 (1968), pp. 182–183.

[22] C. Wu and L. V. Zhigilei. "Microscopic mechanisms of laser spallation and ablation of metal targets from large-scale molecular dynamics simulations". In: *Appl. Phys. A* 114 (2014), p. 11. DOI: 10.1007/s00339-013-8086-4.

[23] S. Noël, J. Hermann, and T. Itina. "Investigation of nanoparticle generation during femtosecond laser ablation of metals". In: *Appl. Surf. Sci.* 253 (2007), pp. 6310–6315. DOI: 10.1016/j.apsusc.2007.01.081.

[24] P. T. Murray and E. Shin. "Formation of silver nanoparticles by through thin film ablation". In: *Mater. Lett.* 62 (2008), pp. 4336–4338. DOI: 10.1016/j.matlet.2008.07.017.

[25] J. C. Alonso et al. "Thin films of silver nanoparticles deposited in vacuum by pulsed laser ablation using a YAG:Nd laser". In: *Appl. Surf. Sci.* 255 (2009), pp. 4933–4937. DOI: 10.1016/j.apsusc.2008.12.040.

[26] C. Wu et al. "Atomic Movies of Laser-Induced Structural and Phase Transformations from Molecular Dynamics Simulations". In: *Lasers in Materials Science*. Ed. by M. Castillejo, P. M. Ossi, and L. Zhigilei. Springer, 2014, pp. 67–100. DOI: 10.1007/978-3-319-02898-9_4.

[27] X. Xu. "Phase explosion and its time lag in nanosecond laser ablation". In: *Appl. Surf. Sci.* 198 (2002), pp. 61–66. DOI: 10.1016/S0169-4332(02)00304-5.

[28] C. Porneala and D. A. Willis. "Time-resolved dynamics of nanosecond laser-induced phase explosion". In: *J. Phys. D: Appl. Phys.* 42 (2009), p. 155503. DOI: 10.1088/0022-3727/42/15/155503.

[29] A. V. Pakhomov, M. S. Thompson, and D. A. Gregory. "Laser-induced phase explosions in lead, tin and other elements: Microsecond regime and UV-emission". In: *J. Phys. D: Appl. Phys.* 36 (2003), pp. 2067–2075. DOI: 10.1088/0022-3727/36/17/308.

Chapter 6

Sputtering deposition of Sn-doped hematite anodes for water oxidation

Preview   Hematite as anodic material in electrocatalysis and photoelectrochemical cells has currently limited applications because of its poor electric properties. To overcome this issue, doping has been applied with some success and high-temperature (800°C) treatment on fluorine doped tin oxide substrates, leading to tin-doping, is now a widely employed procedure to activate hematite anodes.

In this chapter, we present a procedure for the synthesis of tin doped crystalline hematite through radiofrequency magnetron sputtering performed at room temperature. Our method is able to isolate the effect of doping from those of morphology and crystallinity, thus allowing a systematic study of the effects of tin doping on the structural, optical and electrochemical properties of hematite thin films. In our case, tin doping leads to improved conductivity and to a decreased (up to 1 order of magnitude) interfacial charge transfer resistance, as revealed by electrochemical impedance spectroscopy.

6.1   Introduction

In recent years iron oxides, conjugating Earth-abundance and high market availability with their non-toxic and environmentally friendly nature, have attracted considerable attention for applications in catalysis where scalability [1, 2], is a central goal. Iron(III) oxide, in particular amorphous iron oxide (a-Fe_2O_3) and hematite (α-Fe_2O_3), has shown promising results as anodic material in electrochemical and photoelectrochemical water splitting cells [3–8], where it performs the oxygen evolution reaction (OER).

Hematite electrical properties are however far from ideal and severely limit its application as anodic material: in bulk form it is a Mott insulator, with resistivity of up to 10^{12} Ωcm and poor carrier mobility, especially for the hole minority carriers, for which it has a diffusion length of about $2 \div 4$ nm and a recombination lifetime in the ps range [9]. Among the strategies adopted to tackle these issues, nanostructuring features prominently [10–12]. In the past, doping by a variety of metals (Ti, Zr, Hf, V, Nb, W, Tl, Pb, Ge, Ce, Pt) has also been explored with mixed results [13]. The notable exception has been doping with a noble metal (Pt) which, along with surface modification with a cobalt phosphate co-catalyst, registered the highest photocurrents at now for a hematite based photoanode [14].

Recently, high temperature (800°C) thermal treatment of hematite photoanodes on fluorine doped tin oxide (FTO) substrates has been observed to greatly improve photocurrents and the effect has been attributed, among other factors, to tin doping by diffusion from the substrate [3, 4]. Tin is in itself a cheap, Earth-abundant and non-hazardous metal, which would be a viable choice as a dopant. Although the tin doping procedure by annealing has become a widely employed method to activate hematite photoanodes [3, 15, 16], the current high temperature approaches are not ideal to investigate the nature and role of tin doping since the conditions required for incorporating tin into the crystalline hematite affect simultaneously various properties, such as the surface morphology and crystallinity of the hematite film as well as the conductivity of the FTO substrate, which play a critical role in determining the overall electrode performance in photoelectrochemical and electrochemical reactions. Additionally, the FTO resistivity has been reported to significantly increase above $600 \div 700$°C and most glass supports will undergo softening and warping with loss of their mechanical properties [17, 18]. The high temperature treatment is also not convenient in view of the scale-up to an industrial fabrication process, since it is energy-intensive and can damage both the electrode supports and substrates.

In this chapter, we discuss the systematic study of the effects of tin doping on hematite thin films, with respect to structural, optical and electrochemical properties, investigating the catalytic performance towards the OER in a water splitting cell. The method chosen for the hematite synthesis is RF-magnetron sputtering (RF-MS), a physical vapor deposition

technique that allows to carefully control the amount of introduced dopant. Using RF-MS we developed a fabrication process to obtain hematite films with a Sn content in the range $1 \div 12$ atomic %, as estimated by energy dispersive X-ray spectroscopy (EDS), which are already crystalline at room temperature, thus eliminating the need for a post-deposition thermal treatment. Therefore, we could study the effect of increasing tin content without changing morphology and crystalline phase, thus decoupling the influence of surface modification and recrystallization, which normally take place at high temperature. While surface morphology remains substantially unaltered, as revealed by scanning electron microscopy, a hematite lattice distortion resulting in an increasing cell volume, roughly linear with the tin content, is revealed by X-ray diffraction, μ-Raman and XPS spectroscopy.

Optical properties are deeply affected as well, with absorption spectra systematically extended in the UV–VIS range, following a decrease of the optical bandgap of up to 0.45 eV for the highest tin content. The electrode metrics with respect to water oxidation are also influenced by tin doping, leading to less positive overpotentials, shifted by as much as 60 mV, and halved Tafel slopes, yielding values that are comparable with those of state-of-the-art amorphous metal oxides and mixed-metal oxides or cobalt phosphates (Co-Pi) [5, 19]. In this case, the effect of tin doping is substantially an improvement of the film conductivity, which reflects in a decreased charge transfer resistance, as revealed by electrochemical impedance spectroscopy (EIS).

6.2 Experimental section

Synthesis

Pure and Sn-doped α-Fe$_2$O$_3$ thin films were synthesized through RF-MS. The vacuum chamber was evacuated to a pressure lower than 4×10^{-7} mbar before deposition and a working pressure of 8×10^{-3} mbar was then obtained through an argon (99.99% purity) flux. An iron oxide disk was used as target (Sematrade, 99.5% purity Fe$_2$O$_3$, 10 cm diameter). The argon plasma was maintained through a RF power source working at 90 W, 13.56 MHz. Substrates to target distance was fixed at 6.0 cm and the substrate holder was kept swinging in front of the target in order to improve film homogeneity.

Crystalline hematite deposition was achieved without applying external substrate heating and without post-deposition treatments. The substrate temperature was monitored using a thermocouple in contact with the metallic substrate holder: during deposition, substrate temperature was weakly increasing and it reached approximately 60°C after 90 min deposition. In order to remove surface contaminations from the target, a 20 min pre-sputtering treatment was performed before deposition at slightly higher argon pressure (1×10^{-2} mbar). This simple and quick way to synthesize
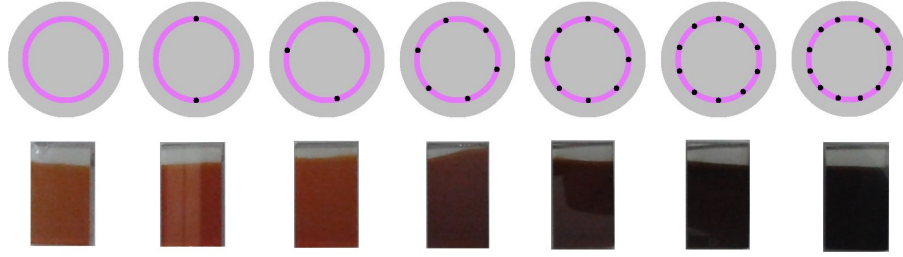
Figure 6.1: Target arrangement and picture of the FTO/hematite electrodes with variable Sn amount. The light purple circle represents the plasma track. The black dots correspond to Sn spheres positions. These target configurations resulted in 0, 1.9, 3.0, 6.2, 7.7, 9.5, 12.4 Sn nominal atomic percentage, respectively.

crystalline hematite was chosen after systematic variation of the sputtering parameters (RF power, pre-sputtering, argon pressure, substrate temperature).

The same deposition parameters and procedure were employed to obtain tin-doped hematite: in that case, a variable number of metallic Sn spheres were placed on the iron oxide target, close to the circular erosion profile (see Figure 6.1).

Compact crystalline hematite films were deposited on 99.99% pure p-Si (100) slides and on fluorine doped tin oxide (FTO) coated glass electrodes. FTO-coated glass samples were cut as 15×25 mm slides and during sputtering deposition a small portion of the FTO area was hidden by an aluminum foil in order to preserve a free FTO contact. In order to perform structural and crystallographic characterization, thick films were grown on Si (about 1 μm, through 155 min deposition process), while 200 nm thick hematite films were deposited on FTO electrodes through 31 min sputtering.

Material characterization

Pure and tin-doped hematite films deposited on Si slides were analyzed through scanning electron microscopy (SEM-FEG, JSM 7001F, JEOL) at 20 keV electron beam energy. In order to evaluate dopant amount, energy dispersive X-ray spectroscopy was employed (EDS, INCA PentaFET-x3).

The vibrational modes and short-range order of films deposited on FTO substrates were studied via Raman spectroscopy, using a Labram Aramis Jobin–Yvon Horiba μ-Raman apparatus equipped with a He–Ne laser source ($\lambda = 632.8$ nm). Furthermore we studied prevalent crystallite orientation and long range order of thick films deposited on Si substrates through X-ray diffraction (XRD) in Bragg–Brentano $\theta - 2\theta$ configuration, exploring the $10° \div 100°$ 2θ range with a step size of $0.05°$ and a scan rate of $0.01°/$s.
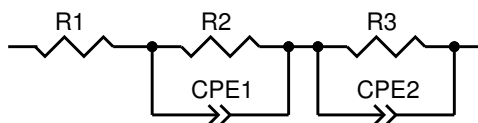
Figure 6.2: Electrical model used to fit EIS data.

As X-ray source for XRD analysis we employed the monochromatic Cu K_α emission ($\lambda = 1.5414$ Å).

X-ray photoelectron spectroscopy (XPS) was acquired by our collaborators at the University of Mumbai using a PHI 5000 VersaProbe II equipped with a monochromatic Al K_α (1486.6 eV) X-ray source and a hemispherical analyzer. Electrical charge compensation was required to perform the XPS analysis. The sample was analyzed at the surface (without pre-sputtering), after sputtering for 2 min with a 1 kV Ar beam and after sputtering for 8 min to reach the bulk of the samples. All the binding energies (BE) were referenced to the C1 s peak at 284.8 eV and reference BE are reported as the average value of all references included in the NIST X-ray Photoelectron Spectroscopy Database [20].

The effect of doping on optical properties of hematite was investigated through a UV-VIS-NIR absorption spectrophotometer (Varian Cary 5000 UV-VIS-NIR absorption spectrometer).

Electrochemical measurements

Electrochemical and photoelectrochemical measurements were performed with an Eco Chemie Autolab PGSTAT 302/N apparatus in a three-electrode cell composed of a saturated calomel electrode (SCE, 0.244 V versus standard hydrogen electrode SHE) as reference, platinum counter electrode and a 1 M KOH electrolyte solution (pH 14). Glass/FTO/hematite samples were used as working electrodes (1 cm^2 active area). Copper tape was applied to the bare portion of FTO in order to optimize electrical connection with the electrode holder. Linear sweep voltammetry (LSV) measurements were collected with scan rate of 10 mV/s in static solution, with applied iR compensation. For photoelectrochemical measurements the illumination source was an ABET solar simulator (AM1.5G, 100 mW/cm^2).

Electrochemical impedance spectroscopy (EIS) measurements were carried out in aqueous 2 M KOH in the dark, by applying a sinusoidal 10 mV perturbation in the frequency range between 10^5 and 10^{-2} Hz. In order to address the kinetics of the faradaic processes, experiments were carried out by sampling the rising part ($0.6 \div 1$ V vs SCE) of the $j-V$ curves at 50 mV intervals.

A good fit of the impedance data was achieved with the model reported in Figure 6.2 where R1 accounts for the ohmic contribution of the electro-

Sn/(Sn+Fe) at.% (± 0.1)	1.2	1.9	3.0	6.2	7.7	9.5	12.4

Table 6.1: EDS Results.

chemical cell (contact and solution resistance) the R3/CPE2 mesh models the electrolyte/hematite interface and R2/CPE1 describes the depletion layer, which should develop in the relatively compact micrometric hematite layers under study. CPE is the constant phase element modeling the non ideal electrochemical capacitance. In our case, the CPE exponent was always comprised between 0.85 and 0.98. EIS experiments were carried out by our collaborators at the University of Ferrara.

6.3   Results and discussion

Film deposition and morphology

Pure and tin-doped hematite was deposited on Si and FTO-coated glass slides. Tin doping in the percentage range $1 \div 12\%$ (expressed as Sn/(Sn+Fe) atomic ratio) was obtained by placing on the Fe_2O_3 target a variable number of metallic Sn small spheres (of about 50 mg weight and of the same size) as shown in Fig. 6.1.

While Sn spheres were usually placed on the plasma erosion profile, 1.2 at.% Sn-doped samples were obtained by placing two Sn spheres about 5 mm outside the plasma track. The picture of a set of samples with increasing dopant loading (Fig. 6.1) clearly shows the color change due to tin doping. Tin percentage was evaluated by EDS measurements and the results are summarized in Table 6.1.

α-Fe_2O_3 and Sn-doped α-Fe_2O_3 films about 1.2 μm thick were deposited on Si slides. The deposited film showed a compact structure with jagged surface morphology (Fig. 6.3). The nearly constant film morphology, together with its compactness, allows us to study the role of dopant loading on electrochemical and optical properties decoupled from morphology effects. It is worth noting that usual experimental procedures to synthesize Sn-doped hematite such as chemical preparation routes and the annealing of pure hematite films on tin-containing substrates generally cause significant morphological modifications [3, 4, 21, 22].

Raman spectroscopy

Thin films with variable Sn loading deposited on glass–FTO substrates showed the presence of hematite Raman response (Fig. 6.4). The spectra showed the vibrational modes of hematite, in particular two A_{1g} modes (219.6 and 492.3 cm^{-1}) and five E_g modes (236.5, 282.7, 295.2, 395.9 and 596.0 cm^{-1}). A peak was also detected at 660 cm^{-1} and it can be explained
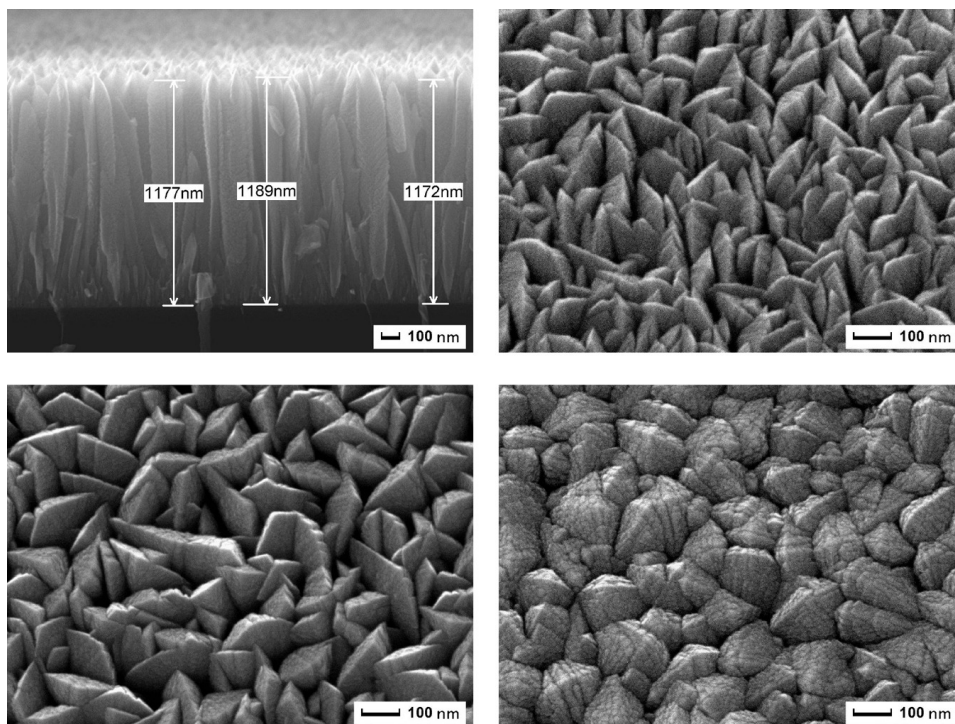
Figure 6.3: (top) Cross section and top view SEM images of pure α-Fe$_2$O$_3$ deposited on silicon; (bottom) Top view SEM images of 6 at.% and 12 at.% tin-doped α-Fe$_2$O$_3$.
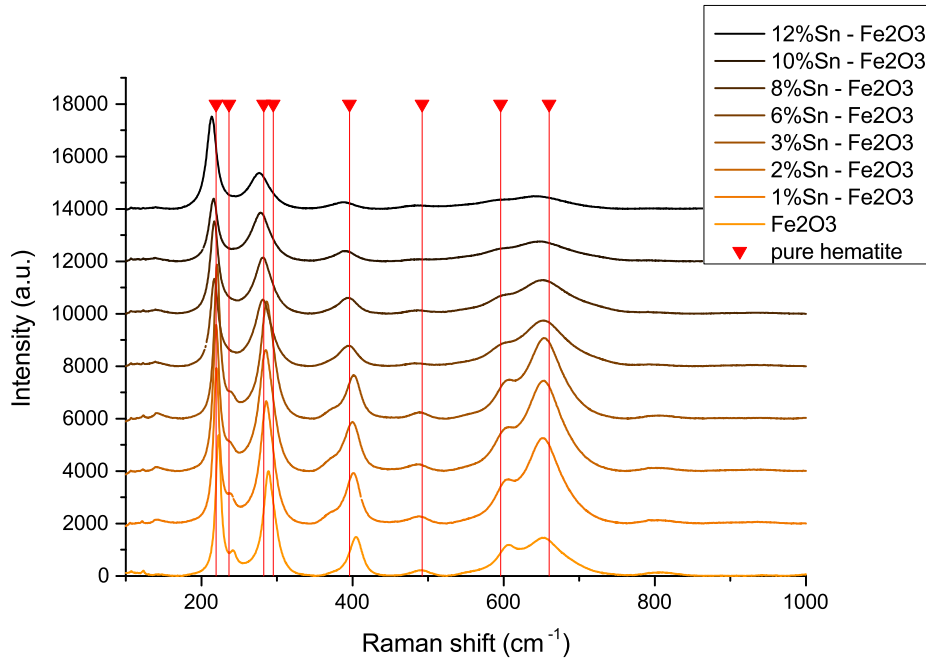
Figure 6.4: μ-Raman spectra of pure and tin-doped hematite films on glass/FTO substrates.

as the activation of the E_u longitudinal optical mode, which is IR active and appears due to the disorder in the hematite lattice [23].

The different intensities and the broadening of the Raman active modes can be explained through a combination of several factors: stress induced by the presence of Sn, size of the crystallites, film thickness. In our case, the crystallite size, as estimated from XRD peaks broadening by using the Scherrer relation, does not vary significantly and no systematic behavior due to the progressive presence of Sn can be recognized. Since film thickness is kept constant, we consider lattice distortion caused by doping as the main reason for the broadening of the Raman peaks.

X-ray diffraction

XRD analysis proved the presence of hematite hexagonal structure as the sole detectable crystalline phase in the deposited films. Rietveld refinement was performed with the Maud software [24], using a March–Dollase texture profile about the (300) hematite plane to account for preferential orientation. The (300) plane, detected at 64.02° in the pure hematite sample, appeared to be the preferred one, allowing good signal fitting for all the dopant loadings.

On the other hand, on the base of our analysis, the (110) reflection resulted to be always in minority, though present in all the spectra (Fig. 6.5).
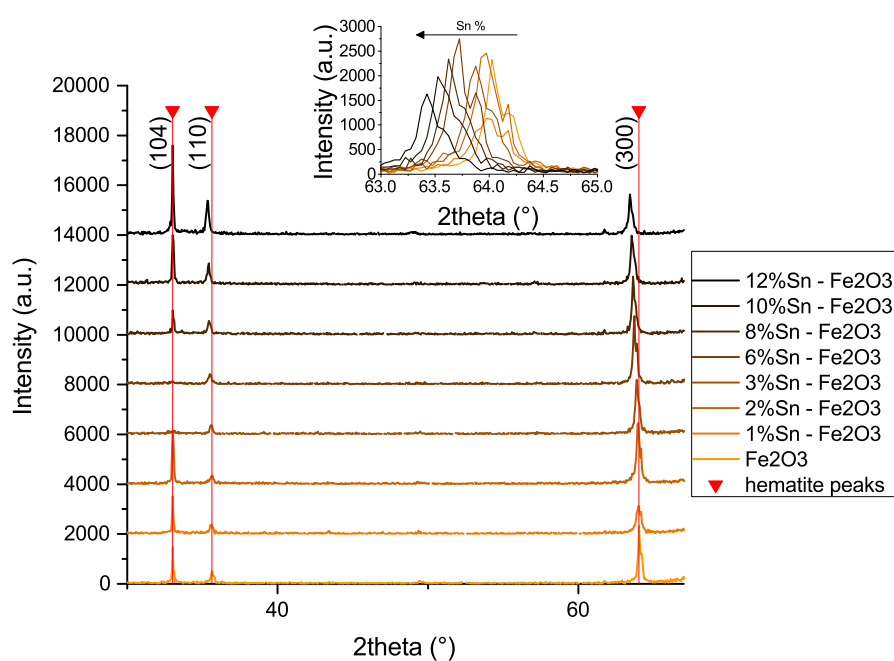
Figure 6.5: XRD spectra of pure and tin-doped hematite (the plot is limited to the range with significant signal). The most intense peaks correspond to (104), (110) and (300) planes. The inset shows (300) peak shifting with different Sn at.%.

Sn %	a (Å)	c (Å)
0	5.0331±0.0003	13.843±0.005
1.2	5.0391±0.0005	13.826±0.005
1.9	5.0395±0.0003	13.818±0.004
3.0	5.0450±0.0003	13.81±0.01
6.2	5.0564±0.0003	13.80±0.01
7.7	5.0613±0.0004	13.771±0.006
9.5	5.0673±0.0004	13.771±0.004
12.4	5.0769±0.0005	13.768±0.004

Table 6.2: Calculation of cell parameters from XRD analysis. b is not reported, since $a = b$.

Since hematite shows a highly anisotropic conductivity and (110) orientation has been proved to be the most favorable one in hematite photoanodes [25], this could explain the absence of a significant photocatalytic activity of our electrodes deposited on FTO.

The phase composition of the films was studied by using as reference the crystalline structures of hematite (Fe_2O_3) and cassiterite (SnO_2) taken from Maud structure database [24] and from the Crystallography Open Database [26], respectively. The Rietveld analysis performed on the diffraction spectrum of the 12.4 at.% sample including the two phases showed that the eventual amount of tin oxide as a distinct phase is below the technique resolution.

Peak positions and relative intensities undergo slight modifications with increasing dopant amount. The cell parameters a and c were extracted from the Rietveld analysis discussed above. The fitting parameters are reported in Table 6.2. As displayed in Fig. 6.6, the hematite hexagonal structure is strained by tin loading, with a progressive elongation of a and b parameters, and contraction of c. The result of the lattice distortion is an approximately linear growth of cell volume as a function of the dopant concentration, as clearly shown in Fig. 6.6(b). In conclusion, XRD characterization proves that in our samples tin atoms are substitutionally located in the hematite lattice.

XPS analysis

XPS spectra were taken both at the surface and in the bulk of the films to investigate the oxidation state of tin and iron. While it is not possible to distinguish between Sn^{2+} and Sn^{4+} due to the strong overlap of their signals [27, 28] (Sn3d5/2 BE= 486.5 ± 0.6 eV and BE= 486.6 ± 0.3 eV, respectively), the presence of metallic Sn (BE= 485.0 ± 0.5 eV) [20] can be considered negligible even for the highest tin content films.
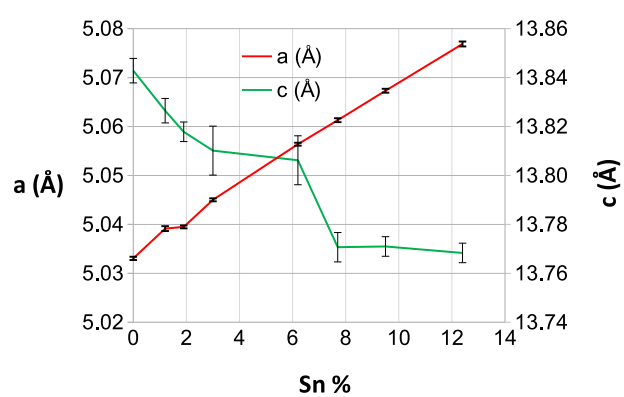
(a)
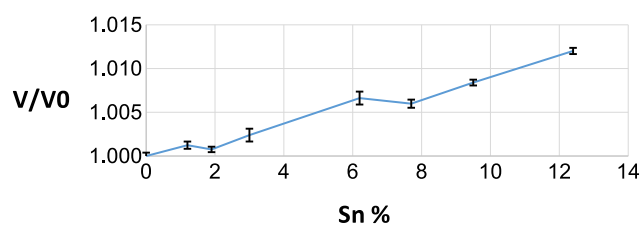
(b)

Figure 6.6: (a) Cell parameters a and c extracted from Rietveld refinement of XRD spectra. (b) Cell volume relatively to pure hematite.
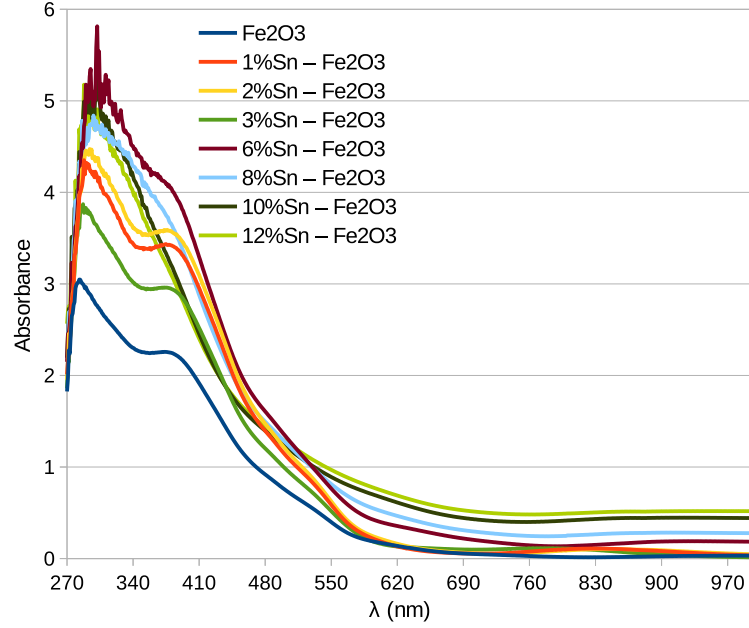
Figure 6.7: Absorbance spectra of pure and tin-doped hematite films on glass/FTO substrates.

Only Fe(III) is detected but, in comparison to pure hematite, the BE for Fe2p signals (Fe2p3/2 peak BE= 710.2 ± 0.5 eV and Fe2p1/2 peak BE= 723.7 ± 0.5 eV) [20] are positively shifted by $0.65 \div 0.85$ eV for all the Sn doped samples. These results indicate that Sn is substitutionally incorporated in the hematite lattice, thus altering the chemical environment of Fe and are in good agreement with XRD and μ-Raman.

Optical properties

UV-VIS-NIR absorption spectroscopy allowed us to study the effect of tin doping on hematite optical properties (Fig. 6.7). The samples with high Sn at.% ($\gtrsim 6$ at.%) show an improved absorption in the entire investigated range and present a progressive absorption range extension toward the infrared region. In order to quantify the absorption range extension, Tauc analysis was performed for both direct and indirect transitions, both of which are reported in literature for hematite [13]. The absorption coefficient was calculated as $a = A/d\log_{10}e$, where A is the absorbance and d the thickness of the film.

Tauc plots in Fig. 6.8 display the quantity $(ah\nu)^{1/r}$ as a function of photon energy, where $r = 1/2$ for direct transitions and $r = 2$ for indirect transitions. The linear fits that allow us to estimate the optical band gap were carried out in the range $2.27 \div 2.42$ eV and $2.40 \div 2.60$ eV for direct

(a)

(b)
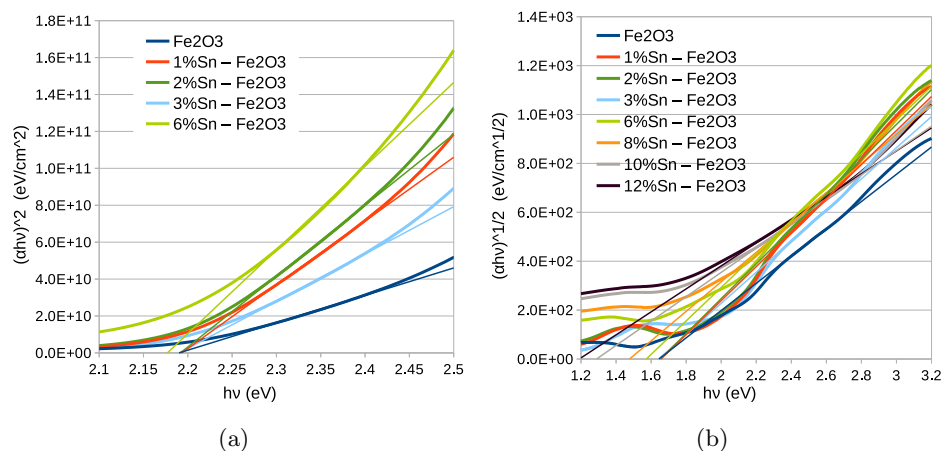
Figure 6.8: Tauc plots for the direct (a) and indirect (b) optical bandgap.

Sn %	0.0	1.2	1.9	3.0	6.2	7.7	9.5	12.4
Direct E_g (eV) ±0.02	2.19	2.19	2.19	2.19	2.18	–	–	–
Indirect E_g (eV) ±0.01	1.64	1.66	1.65	1.64	1.57	1.48	1.29	1.19

Table 6.3: Direct and indirect optical bandgaps.

and indirect transitions, respectively. In the case of high Sn loading (8, 10, 12 at.%) a direct transition was not clearly observed. In Table 6.3, we show the calculated band gaps and especially in the case of indirect transition it is possible to observe a clear band gap reduction of about 0.45 eV at high tin at.%.

In conclusion we experimentally proved that intermediate doping ($\approx$ 6 at.% Sn) causes band gap reduction due to formation of sub-band gap states originated by the introduction of dopant atoms, while at higher Sn percentage the band structure is more deeply altered by the disappearance of the direct transition. These results are in agreement with recent computational work on tin-doped hematite [29].

Electrochemistry

The hematite and tin-doped hematite films deposited on FTO electrodes were tested for electrochemical and photoelectrochemical water oxidation in a three-electrode configuration cell. Before measurement, the electrodes were subjected to voltammetry cycles in the potential range -0.24 ÷ 1.76 V versus SCE in order to obtain a stable response and to remove eventual surface impurities. The $j-V$ characteristics under dark conditions with iR compensation are shown in Fig. 6.9, with the inset showing Tafel plots. The electrode metrics obtained by Tafel analysis (overpotential at $j = 1$ mA/cm^2
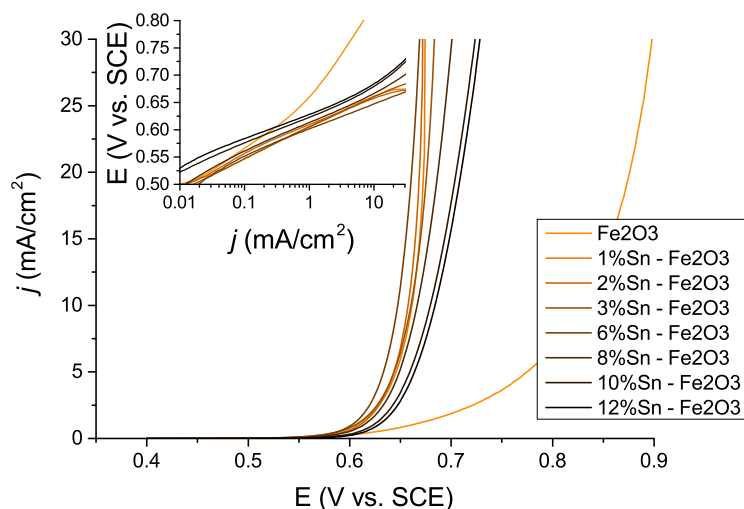
Figure 6.9: LSVs under dark conditions of pure and tin-doped hematite films deposited on FTO electrodes. iR compensation was applied. In the inset, the same data are displayed as a Tafel plot.

Sn %	0.0	1.2	1.9	3.0	6.2	7.7	9.5	12.4
η (mV) ± 5	498	446	449	445	441	453	463	468
b (mV/dec) ± 0.3	102	56.8	48.4	55.5	47.9	49.5	49.0	50.3

Table 6.4: Onset overpotential η ($j = 1$ mA/cm^2) and Tafel slope b.

and Tafel slopes) are summarized in Table 6.4. It is immediately evident that all Sn:Fe$_2$O$_3$ are better OER catalysts than their undoped counterpart, with the best performance for Sn concentration in the range 2÷6 at.% Sn. In particular, the best results were found for the 6.2 at.% sample, which exhibits 441 mV overpotential at 1 mA/cm^2 and 48 mV/dec Tafel slope (see Table 6.4 for details).

It is worth noting that the high Tafel slope of the pure hematite film is halved by introducing Sn: this result has to be attributed to doping since the films have negligible difference in terms of surface morphology, crystallite orientation and film thickness. The electrocatalytic activity of the tin-doped hematite compact films deposited by RF-MS are comparable with that of nanostructured amorphous Fe$_2$O$_3$ thin coatings synthesized by pulsed laser deposition [6] ($\eta = 497$ mV at 0.2 mA/cm^2, $b = 35.6$ mV/dec) or photochemical metal-organic deposition [5] ($\eta = 400$ mV at 0.5 mA/cm^2, $b = 40$ mV/dec). This is remarkable for compact bulk-like films as the ones under study and indicates great potential for improvement by introducing nanostructuring.

The reason for the enhanced OER catalysis performance lies essentially
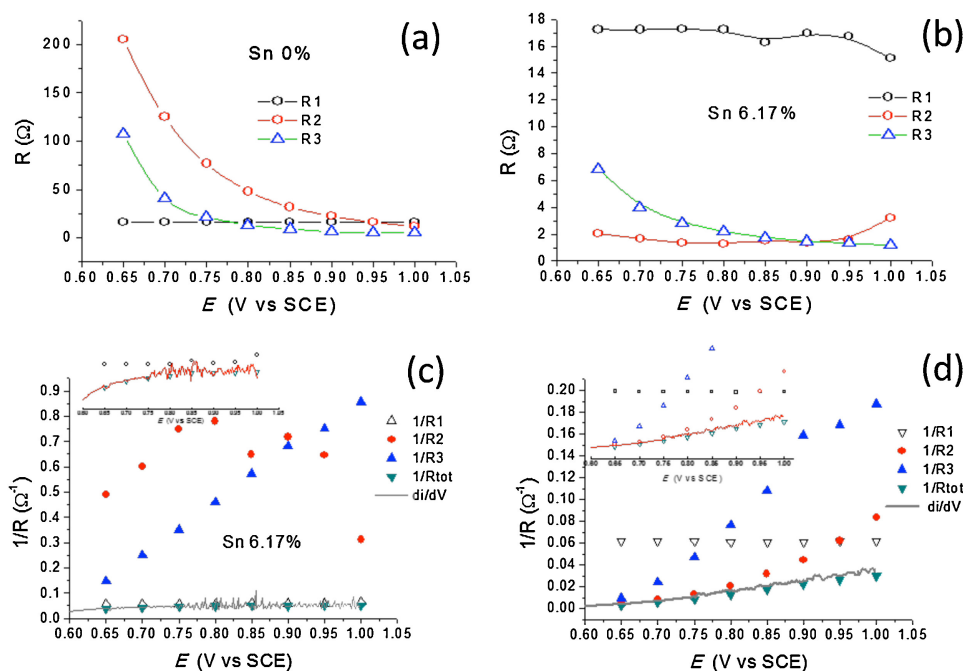
Figure 6.10: (a,b) Individual resistive contributions vs applied voltage in unmodified hematite and 6.17 at.% Sn-doped anodes. (c,d) Reciprocal of the individual resistances (R_i^{-1}) and their sum (R_{TOT}^{-1}, green upside-down triangle) compared to $\delta i/\delta V$ (grey line). 2 M KOH. Inset: magnification of the $\delta i/\delta V$ vs R_{TOT}^{-1} plot.

in a significant reduction of both the R2 resistance and the charge transfer resistance (R3), consistent with both improved conductivity and better electrocatalytic ability of the tin doped hematite films (Fig. 6.10) where each resistive element (R1, R2 and R3) is plotted as a function of the applied potential. In both unmodified hematite (Fig. 6.10(a)) and in the 6.17 at.% (Fig. 6.10(b)) Sn doped sample the ohmic resistance accounting for the cell resistance is essentially the same, ca. 20Ω, expectedly independent from the potential, and in agreement with the typical ohmic resistance of the FTO back contact. In both substrates R3 decreases exponentially with the applied potential, in agreement with the high field approximation of the Butler–Volmer equation, and was thus assigned to the charge transfer resistance (R_{CT}), being about one order of magnitude larger in unmodified hematite with respect to the best performing Sn doped sample.

In the pure Fe_2O_3 electrode, R2 represents the major resistive contribution and decreases exponentially with the applied potential, while in the 6.17% Sn doped sample this contribution is the smallest and is substantially independent from the potential. The summed individual resistive contributions describe both qualitatively and quantitatively well the $j - V$ response

of the electrode, as can be appreciated from Fig. 6.10(c) and (d), where the derivative of the current–voltage curve is compared to R_{TOT} where $R_{TOT} = R_1 + R_2 + R_3$. It can be clearly observed from Fig. 6.10(b) and (d) that in the doped sample it is the ohmic R1 (principally the resistance of the ohmic collector) the dominating factor in controlling the $j - V$ response of the cell, whereas R2 and R3 are on average less than 10 times smaller than the former. By contrast, in the unmodified sample, the electrochemical response is largely limited by both the R2 component and by the charge transfer resistance (R3), with the three resistive contributions becoming relatively comparable in magnitude only at strong positive potential, i.e. for V> 0.9 V vs SCE.

A contribution to the improved conductivity in tin-doped hematite may arise from a reduction of the effective electron mass, as these are inversely proportional quantities for an n-type semiconductor. As recently predicted by theoretical modeling based on first-principles calculations [29], tin doping in the range $1 \div 16$ at.% is indeed expected to induce a decrease in the effective electron mass irrespective of the Miller plane considered.

Despite the enhanced light absorption properties discussed above, all these electrodes did not show a satisfactory photocurrent response if compared to nanostructured films with optimized morphology. This has to be attributed to a combination of film thickness, compact morphology and unfavorable crystallite orientation. In fact, it is known in literature that non-porous hematite films with thickness of some micrometers can show significant photocurrents [30] and that crystallite prevalent orientation can determine the photocatalytic activity [25] by overcoming the issue of the small carrier diffusion length of hematite with a preferential charge transport toward the desired direction.

In addition, constant potential electrolysis carried out on the 7.7 % Sn-doped sample at 1 V versus SCE in 1 M KOH (Fig. 6.11), without iR compensation, showed a current variation smaller than 3% during a 120 min test, testifying an appreciable film stability.

6.4 Conclusions

In this chapter, we described a synthetic procedure for tin-doped hematite based on RF-MS and proceeded to fabricate thin films with a controlled content of Sn in the range $1 \div 12$ at.% (Sn/Sn+Fe). This procedure is in itself an advancement over current fabrication techniques since crystalline tin-doped hematite could be obtained at room temperature, without relying on energy-intensive and potentially substrate-damaging post-fabrication thermal treatments. Moreover, this allowed us to systematically vary the Sn content without significantly altering the surface morphology and the crystal phase of the samples, which are determinant for the OER catalysis perfor-
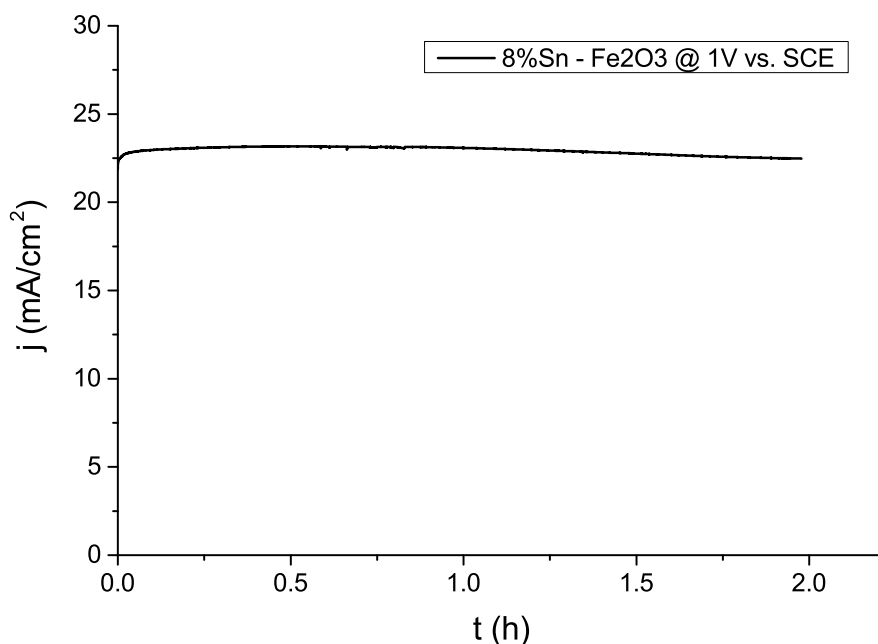
Figure 6.11: Chronoamperometric plot of of the 7.7 at.% Sn-doped sample at 1 V versus SCE during a 120 min electrolysis.

mance, thus effectively surveying the effects of an increasing tin content on the structural, optical and electrochemical properties of the material.

Doping in the range $1 \div 12$ at.% leads to hematite lattice distortion consistent with the presence of tin atoms as substitutional dopants, which is substantially linear with the Sn/Fe ratio. The optical absorption in the visible range is greatly extended due to band-gap narrowing, though this is not paralleled by the appearance of a significant photoelectrochemical activity. The reason for this behavior is likely a combination of unfavorable crystalline planes orientation, compact morphology limiting solvent permeation and excessive thickness compared to the typical carrier diffusion length of hematite.

The electrode metrics with respect to the electrochemical OER are improved by doping, resulting in much better charge transport and transfer properties with respect to the unmodified counterpart. The Tafel analysis revealed the best performance in the case of 6.2% sample, which exhibits 441 mV overpotential at $j = 1$ mA/cm^2 and 48 mV/dec Tafel slope. Although overpotentials are in the usual range for hematite anodes, Tafel slopes of the tin doped samples are in line with state-of-the-art catalysts, e.g. amorphous mixed-metal oxides and Co-Pi, and point out their promising application in electrocatalytic water oxidation.

While useful for a first systematic investigation of tin-doping effects, the

synthetic procedure presented here does not allow pursuing the nanostructuring strategy, which should further improve their performance in OER and is likely essential to enable the efficient extraction of photo-generated electrons, thus allowing to extend our investigation to photoelectrochemical applications. Future work will then focus on the possibility of inducing nanostructures with RF-MS by tuning deposition pressure and temperature according to Thornton's structure-zone diagram [31].

References for Chapter 6

[1] P. C. K. Vesborg and T. F. Jaramillo. "Addressing the terawatt challenge: scalability in the supply of chemical elements for renewable energy". In: *RSC Advances* 2 (2012), pp. 7933–7947. DOI: 10.1039/c2ra20839c.

[2] M.D. Bhatt and J.S. Lee. "Recent theoretical progress in the development of photoanode materials for solar water splitting photoelectrochemical cells". In: *Journal of Materials Chemistry A* 3.20 (2015), pp. 10632–10659. DOI: 10.1039/c5ta00257e.

[3] K. Sivula et al. "Photoelectrochemical Water Splitting with Mesoporous Hematite Prepared by a Solution-Based Colloidal Approach". In: *J. Am. Chem. Soc.* 132 (2010), pp. 7436–7444. DOI: 10.1021/ja101564f.

[4] Y. Ling et al. "Sn-Doped Hematite Nanostructures for Photoelectrochemical Water Splitting". In: *Nano Lett.* 11 (2011), pp. 2119–2125. DOI: 10.1021/nl200708y.

[5] R. D. L. Smith et al. "Photochemical Route for Accessing Amorphous Metal Oxide Materials for Water Oxidation Catalysis". In: *Science* 340 (2013), p. 60. DOI: 10.1126/science.1233638.

[6] M. Orlandi et al. "Pulsed-Laser Deposition of Nanostructured Iron Oxide Catalysts for Efficient Water Oxidation". In: *ACS Appl. Mater. Interfaces* 6 (2014), pp. 6186–6190. DOI: 10.1021/am501021e.

[7] L. Trotochaud et al. "Solution-Cast Metal Oxide Thin Film Electrocatalysts for Oxygen Evolution". In: *J. Am. Chem. Soc.* 134 (2012), pp. 17253–17261. DOI: 10.1021/ja307507a.

[8] N. Dalle Carbonare et al. "Improvement of the Electron Collection Efficiency in Porous Hematite Using a Thin Iron Oxide Underlayer: Towards Efficient All-Iron Based Photoelectrodes". In: *Phys. Chem. Chem. Phys.* 17 (2015), pp. 29661–29670. DOI: 10.1039/C5CP04152J.

[9] F.E. Osterloh. "Inorganic nanostructures for photoelectrochemical and photocatalytic water splitting". In: *Chemical Society Reviews* 42.6 (2013), pp. 2294–2320. DOI: 10.1039/c2cs35266d.

[10] A. Kay, I. Cesar, and M. Grätzel. "New benchmark for water photooxidation by nanostructured α-Fe$_2$O$_3$ films". In: *Journal of the American Chemical Society* 128.49 (2006), pp. 15714–15721. DOI: 10.1021/ja0643801.

[11] B. M. Klahr, A. B. Martinson, and T. W. Hamann. "Photoelectrochemical Investigation of Ultrathin Film Iron Oxide Solar Cells Prepared by Atomic Layer Deposition". In: *Langmuir* 27 (2011), pp. 461–468. DOI: 10.1021/la103541n.

[12] V. Cristino et al. "Efficient Solar Water Oxidation using Photovoltaic Devices Functionalized with Earth-abundant Oxygen Evolving Catalysts". In: *Phys. Chem. Chem. Phys.* 15 (2013), pp. 13083–13092. DOI: 10.1039/c3cp52237g.

[13] V.R. Satsangi, S. Dass, and R. Shrivastav. "Nanostructured α-Fe$_2$O$_3$ in PEC Generation of Hydrogen". In: *On Solar Hydrogen & Nanotechnology*. Ed. by L. Vayssieres. John Wiley & Sons, Ltd, 2010, pp. 349–397. DOI: 10.1002/9780470823996.ch13.

[14] J.Y. Kim et al. "Single-crystalline, wormlike hematite photoanodes for efficient solar water splitting". In: *Scientific Reports* 3 (2013). DOI: 10.1038/srep02681.

[15] C.D. Bohn et al. "Effect of tin doping on α-Fe$_2$O$_3$ photoanodes for water splitting". In: *Journal of Physical Chemistry C* 116.29 (2012), pp. 15290–15296. DOI: 10.1021/jp305221v.

[16] J. Frydrych et al. "Facile fabrication of tin-doped hematite photoelectrodes - Effect of doping on magnetic properties and performance for light-induced water splitting". In: *Journal of Materials Chemistry* 22.43 (2012), pp. 23232–23239. DOI: 10.1039/c2jm34639g.

[17] H. Zhao et al. "Oxygen distribution of fluorine-doped tin oxide films coated on float glass along depth before and after heat treatment". In: *International Journal of Applied Glass Science* 4.3 (2013), pp. 242–247. DOI: 10.1111/ijag.12016.

[18] J.K. Yang et al. "Reference of Temperature and Time during tempering process for non-stoichiometric FTO films". In: *Scientific Reports* 5 (2015). DOI: 10.1038/srep15001.

[19] Y. Surendranath, M.W. Kanan, and D.G. Nocera. "Mechanistic studies of the oxygen evolution reaction by a cobalt-phosphate catalyst at neutral pH". In: *Journal of the American Chemical Society* 132.46 (2010), pp. 16501–16509. DOI: 10.1021/ja106102b.

[20] A. V. Naumkin et al. *NIST X-ray Photoelectron Spectroscopy Database*. Tech. rep. National Institute of Standards and Technology, 2012.

96

[21] J. Cai et al. "Electrodeposition of Sn-doped hollow Fe_2O_3 nanostructures for photoelectrochemical water splitting". In: *J. Alloys Compd.* 574.2 (2013), pp. 421–426. DOI: 10.1016/j.jallcom.2013.05.152.

[22] H. K. Dunn et al. "Tin doping speeds up hole transfer during light-driven water oxidation at hematite photoanodes". In: *Phys. Chem. Chem. Phys.* (2014). DOI: 10.1039/C4CP03946G..

[23] A. M. Jubb and H. C. Allen. "Vibrational Spectroscopic Characterization of Hematite, Maghemite, and Magnetite Thin Films Produced by Vapor Deposition". In: *ACS Appl. Mater. Interfaces* 2 (2010), pp. 2804–2812. DOI: 10.1021/am1004943.

[24] *Maud: Materials Analysis Using Diffraction, Version 2.68.* 2016.

[25] S. Kment et al. "Photoanodes with Fully Controllable Texture: The Enhanced Water Splitting Efficiency of Thin Hematite Films Exhibiting Solely (110) Crystal Orientation". In: *ACS Nano* 9 (2015), pp. 7113–7123. DOI: 10.1021/acsnano.5b01740.

[26] S. Gražulis et al. "Crystallography Open Database (COD): An open-access collection of crystal structures and platform for world-wide collaboration". In: *Nucleic Acids Research* 40.D1 (2012), pp. D420–D427. DOI: 10.1093/nar/gkr900.

[27] J. A. Rodriguez et al. "Surface Chemistry of SO_2 on Sn and Sn/Pt(111) Alloys: Effects of Metal-Metal Bonding on Reactivity toward Sulfur". In: *J. Am. Chem. Soc.* 120.7 (1998), pp. 11149–11157. DOI: 10.1021/ja982174a.

[28] G. J. Siri et al. "XPS and EXAFS study of supported PtSn catalysts obtained by surface organometallic chemistry on metals Application to the isobutane dehydrogenation". In: *Appl. Catal., A* 278 (2005), pp. 239–249. DOI: 10.1016/j.apcata.2004.10.004.

[29] X. Meng et al. "Theoretical Understanding of Enhanced Photoelectrochemical Catalytic Activity of Sn-Doped Hematite: Anisotropic Catalysis and Effects of Morin Transition and Sn Doping". In: *J. Phys. Chem. C* 117 (2013), pp. 3779–3784. DOI: 10.1021/jp310740h.

[30] K.G. Upul Wijayantha, S. Saremi-Yarahmadi, and L.M. Peter. "Kinetics of oxygen evolution at α-Fe_2O_3 photoanodes: A study by photoelectrochemical impedance spectroscopy". In: *Physical Chemistry Chemical Physics* 13.12 (2011), pp. 5264–5270. DOI: 10.1039/c0cp02408b.

[31] J. A. Thornton. "Influence of apparatus geometry and deposition conditions on the structure and topography of thick sputtered coatings". In: *J. Vac. Sci. Technol., A* 11 (1974), p. 666. DOI: 10.1116/1.1312732.

Chapter 7

Pulsed laser deposition of highly nanostructured a-Fe$_2$O$_3$ for photoanode functionalization

Preview By taking advantage of the versatility of pulsed laser deposition technique, in this chapter we discuss the synthesis of an amorphous iron(III) oxide catalyst for water oxidation. In particular, we examine a highly porous morphology compared to a compact nanoparticle-assembled coating. The porous catalyst allows fulfilling two key issues in the design of integrated absorber/electrocatalyst schemes, such as parasitic light absorption and the nature of the absorber/catalyst junction.

Here we study the functionalization of hematite thin layer photoanodes with the porous or compact a-Fe$_2$O$_3$ catalyst and we characterize the photoresponse under simulated solar light. In this chapter, a state of art integrated photoanode as introduced in Chapter 2 is built and characterized in detail.

The content of this chapter was adapted from:
M. Orlandi, N. Dalle Carbonare, S. Caramori, C. A. Bignozzi, S. Berardi, A. Mazzi, Z. El Koura, N. Bazzanella, N. Patel and A. Miotello, ACS Appl. Mater. Interfaces 8 (2016), pp. 20003–20011.
© 2016 American Chemical Society.

7.1 Introduction

Materials designed for photodriven fuel synthesis must perform two essential functions: (1) sunlight absorption to generate electron–hole pairs and

(2) catalysis of the fuel-forming reactions (including the facilitation of charge transfer, surface stabilization, electrode reusability...). The latter becomes critical when multielectron redox reactions are involved, leading to slow kinetics and consequent loss of efficiency. A significant example is photochemical water electrolysis performed in a photoelectrochemical cell (PEC), where the strict kinetic requirements dictated in particular by the oxygen evolution reaction, which involves the proton-coupled exchange of four electrons, have driven for decades the search for efficient catalysts [1–3].

In recent years, the research efforts have been increasingly directed toward schemes where the absorption and catalytic functions are separately optimized and then integrated by functionalization of absorber materials with redox catalysts. Examples include inorganic semiconductors or molecular chromophores as absorbers, functionalized by coupling with molecular catalysts or nanostructures of metals or metal oxides [4–11]. This kind of scheme allows for a simpler yet more in-depth screening of candidate catalysts while taking advantage of materials with already optimized optical properties (e.g., for photovoltaic applications) but also presents new challenges. Two critical issues are (a) the nature of the absorber/catalyst junction and (b) the parasitic light blocking [5, 12] by catalysts deposited on the absorber surface. The former depends largely on the morphology of the catalyst, with dense ion-impermeable structures yielding buried junctions and nonoptimal performance. By contrast, porous ion-permeable architectures can lead to adaptive junctions[1] and substantially enhanced charge separation and photovoltage generation[13]. As for the latter, in the case of metal oxides oxygen evolving catalysts (OEC) deposited on photoanodes, the effect of optical losses on the overall efficiency is so severe that in a recent investigation the best performance was obtained with a subnanometric film thickness [14]. However, a higher catalyst mass loading is generally beneficial to reduce overpotential. This trade-off between optical losses and catalyst loading limits the application of Earth-abundant, cheap, and scalable alternatives to noble-metal-based catalysts because the replacements generally have lower catalytic activity and higher quantities would be needed to produce a comparable performance [15, 16].

In the work presented in this chapter, we address both issues by the design and fabrication of an amorphous Fe_2O_3 (a-Fe_2O_3) OEC with a porous morphology consisting of a nanoparticle-assembled coating. The porous nature of the catalyst allows for ion permeability, leading to the probable formation of an adaptive junction with the photoactive material while maintaining high transparency in the visible region, likely due to the very small size of the nanometric structures (≤ 5 nm), possibly leading to a quantum

---

[1]In adaptive semiconductor/electrocatalyst junctions, the effective interface barrier height Φ_b, and hence the photovoltage output of the electrode, changes depending on the oxidation state of the electrocatalyst. This represents an optimized solution for charge separation and photovoltage generation.

confinement effect, as recently reported for hematite [17]. Capitalizing on the versatility of pulsed laser deposition (PLD), we were able to perform a comparative investigation where by changing the deposition conditions different morphologies of a catalytic material having the same nominal composition (i.e., a largely amorphous iron(III) oxide), ranging from a dense compact layer to a porous nanoparticle-assembled coating, were cast on nanocrystalline hematite thin layers (HTL) acting as light absorber. The latter was selected as model host substrate by virtue of their ease of fabrication with good reproducibility and acceptable baseline performances in photoelectrochemical water oxidation arising from their thickness (about 30 nm), which not only yields modest light-harvesting capability but also is compatible with the short carrier diffusion lengths of hematite [18]. The photoresponse of these modified photoanodes, consisting of the integrated absorber–catalyst system, was largely affected by the specific nature of the catalytic layer. The dense film deposition invariably leads to a large decrease in the photoelectrochemical response compared to the unmodified film, and photoanodes decorated with the porous catalyst show a drastic lowering of the photocurrent overpotential (about 200 mV) and a concomitant fivefold increase in photocurrents at 1.23 V versus reversible hydrogen electrode (vs RHE) in 0.1 M NaOH (pH 13.3). This provides an additional guideline, besides the evaluation of the "dark" electrochemical activity of the oxygen evolving species, on the properties that should be pursued for the successful integration of a charge transfer catalyst in a photoelectrode for water splitting. Clearly, the choice of iron oxide as both the absorber material and OEC is motivated by the need to find Earth-abundant, cheap, and scalable materials to enable the large-scale application of solar water-splitting schemes. Iron oxide not only satisfies all these requisites [19] but also is nontoxic and environmentally safe.

7.2 Experimental methods

Materials $FeCl_3 \cdot 6H_2O$ ($\geq 99\%$) and NaOH (98%) were purchased from Alfa Aesar. Polyethylene glycol bisphenol A epichlorohydrin copolymer (molar weight 15000–20000 Da) were purchased from Sigma–Aldrich. Fluorine-doped tin oxide glass slides (FTO, Hartford Glass) were cleaned by successive 30 min ultrasonic treatments in acetone, ethanol, aqueous Alconox (Sigma–Aldrich) solution, and distilled water and then blown dry with a warm air stream. A portion of the slides was then masked with KAPTON tape (Tesa) to preserve an uncovered zone for the electric contact. A metallic iron disc (purity 99.9%, Sematrade) was used as the target material for PLD.

Crystalline Hematite Thin Layers (HTL) Preparation   Crystalline HTL was spin-coated on FTO electrodes by our collaborators at the University of Ferrara. $FeCl_3 \cdot 6H_2O$ (0.54 g) was dissolved in DI water (20 mL), and then polyethylene glycol bisphenol A epichlorohydrin copolymer (0.54 g) was added under gentle stirring to avoid the formation of bubbles. The solution was spin-coated onto FTO glass (1000 rpm for 9 s and 2000 rpm for 30 s). After each spin-coating cycle, the glass slide was annealed at 550°C for 15 min in air. Spin-coating cycles were repeated 3 times and, after the third cycle, the electrode was heated at 550°C for 2 h and ramped to 800°C and held for 10 min. The electrode was cooled to room temperature (RT) by suspending the heating.

PLD of amorphous Iron Oxide (a-Fe$_2$O$_3$)   a-Fe$_2$O$_3$ was deposited through PLD technique on commercial (Sigma–Aldrich) quartz and p-type Si substrates (for UV–VIS and scanning electron microscopy characterization, respectively) on FTO electrodes (for Raman spectroscopy and electrochemistry experiments) and on FTO/HTL electrodes (for photoelectrochemistry experiments). PLD was performed by using a KrF excimer laser (Lambda Physik LP 220i) with an operating wavelength of 248 nm, pulse duration of 25 ns, operated at a repetition rate of 20 Hz and laser fluence of 2.0 J/cm^2. The deposition chamber was evacuated up to a base pressure of 10^{-6} mbar. Then, oxygen gas was back-filled into the chamber through a mass flow controller. Deposition was performed at a constant oxygen pressure of 0.45 mbar. The distance between the metallic iron target and substrates was optimized to 5.5 cm and the number of pulses was fixed (2000 pulses), to ensure that all samples have the same quantity of material. Substrate temperature during PLD was either room temperature (RT) or 300°C (DEP300). A more detailed description of the PLD apparatus is available elsewhere [20]. For comparison, some samples were deposited at RT and then annealed at 300°C and 550°C in air in a tubular furnace. These are labeled AN300 and AN550 respectively. The heating rate was set to 10°C/min, and the desired temperature was kept constant for 2 h.

Characterization   Scanning electron microscopy (SEM) was used to analyze the morphology and the thickness of the films. Measurements were performed using a JEOL JSM-7001F FEG-SEM at 20.0 keV electron beam energy. The SEM apparatus is equipped with an energy dispersive X-ray spectroscopy detector (EDS, Oxford INCA PentaFETx3). The working distance was maintained between 3 and 8 mm. Surface morphology images were acquired in top-down and tilted modes, whereas cross-sectional analysis was performed putting the films on a 90° stub.

Raman measurements were performed on a Horiba LabAramis setup equipped with a HeNe 633 nm laser as source and a confocal microscope

($100\times$ objective) coupled to a 460 mm focal length CCD-based spectrograph equipped with a four interchangeable gratings turret. In the range between 450 and 850 nm, the wavenumber accuracy is 1 cm^{-1} with a 1800 L/mm grating. The laser power is 15 mW, and the maximum spot size is 5 μm. An accumulation number of 10 and an exposure time of 7 s were employed for all measurements.

UV–VIS absorption was studied using a Varian Cary 5000 spectrophotometer, and quartz substrate was also used to investigate the UV region. Stationary emission spectra were measured by our collaborators in Ferrara with an Edinburgh Instruments FLS 920 spectrofluorimeter, equipped with a double emission monochromator by using an excitation bandwidth ($\Delta\lambda$) of 7 nm. The ferric oxide thin films (RT, AN300, and DEP300) deposited on quartz slides were placed in a dedicated film holder equipped with a micrometer stage in order to optimize the angle between the thin film, the excitation beam and the emitted light reaching the detector. The signal/noise ratio was optimized by summing 10 subsequent scans with 1 nm wavelength step and a dwell time of 0.1 s. Spectra were corrected for the photomultiplier (R928P-Hamamatsu) response by using a factory-built calibration file. Excitation was in the absorption manifold of the ferric oxide, either at 350 or 300 nm. Two different types of cutoff filters (395 and 350 nm) prevented scattered excitation light from reaching the phototubes.

XPS was performed by our collaborators at the University of Mumbai using a PHI 5000 VersaProbe II equipped with a monochromatic Al K_{α} (1486.6 eV) X-ray source and a hemispherical analyzer. Electrical charge compensation was required to perform the XPS analysis. The sample surface was sputtered for 30 s in order to remove any surface oxidation.

$j-V$ and constant potential electrolysis experiments were carried out in a three-electrode configuration cell using a platinum electrode and a saturated calomel electrode (SCE) as counter and reference electrodes, respectively. The cell containing aqueous NaOH (either 0.1 M, pH 13.3, or 1 M, pH 14) as electrolyte was connected to an Eco Chemie Autolab PGSTAT 302/N electrochemical work-station. $j-V$ curves were recorded at a scan speed of 20 mV/s.

The measurements under illumination were performed at the University of Ferrara, by using an ABET solar simulator (AM1.5G, 100 mWcm^{-2}). The illuminated area of the photoelectrode was 1 cm^2. IPCE spectra were recorded under a potential bias of both 1.1 and 1.5 V vs RHE. The steady-state photoanodic current was recorded every 10 nm from 330 to 600 nm on a PGSTAT 30 electrochemical workstation. The incident monochromatic irradiance was measured with a calibrated silicon photodiode (Centronic ASD100–7Q). IPCE was calculated according to Eq. (2.3), while APCE was obtained as IPCE/LHE, where the light harvesting efficiency (LHE) is expressed as:

$$\text{LHE}(\lambda) = 1 - 10^{-A(\lambda)}, \tag{7.1}$$

102
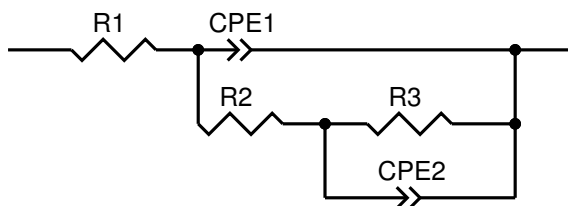
Figure 7.1: Equivalent circuit used for the fitting of EIS data.

A being the absorbance of the photoelectrode measured in transmission mode.

Electrochemical impedance spectroscopy (EIS) data of photoanodes under illumination were recorded, at the University of Ferrara, in the three-electrode configuration cell described above in 0.1 M NaOH (pH 13.3). Sample data were obtained from −0.73 to 1.53 V vs RHE at 50 mV intervals employing a FRA2.v10 frequency-response analyzer controlled by Nova 1.10. A 10 mV amplitude sinusoidal perturbation (single sine) whose frequency ranged between 100 kHz and 0.05 Hz was adopted. The impedance response was fitted using ZView software with the equivalent electric circuit reported in Figure 7.1.

7.3   Results and discussion

Cross-sectional SEM analysis of RT samples deposited on silicon substrates, shown in Fig. 7.2(a), reveals a complex morphology with scattered particles of diameter in the range of about 30÷300 nm covered by a porous structure made of smaller particles assembled in irregular wires. As the size of these latter particles approaches the spatial resolution of the SEM apparatus (2 nm), a conservative estimation for their average diameter is 5 ± 2 nm. Because of the very rough morphology, it is not possible to define a layer thickness, but the surface coverage appears to be complete, as we show in Figure 7.2(c). Annealing of RT samples at 300°C results in a partial collapse of the porous structure by aggregation of the smaller particles (AN300, Figure 7.2(d)), which becomes complete in the case of AN550 (Figure 7.2(e)). Deposition with the substrate heated at 300°C (DEP300) results in a more compact NPs-assembled layer (Figure 7.2(b) and (f), cross-sectional and top views, respectively) similar to the structures typically obtained with lower deposition pressures [21]. This effect is due to the higher mobility of the particles when they hit the heated substrate, leading to aggregation and the formation of bigger and partially assembled particles, mostly of diameter > 10 nm.

In the case of the high-pressure depositions employed here, the oxygen atmosphere reduces the kinetic energy of the ablated material, limits the
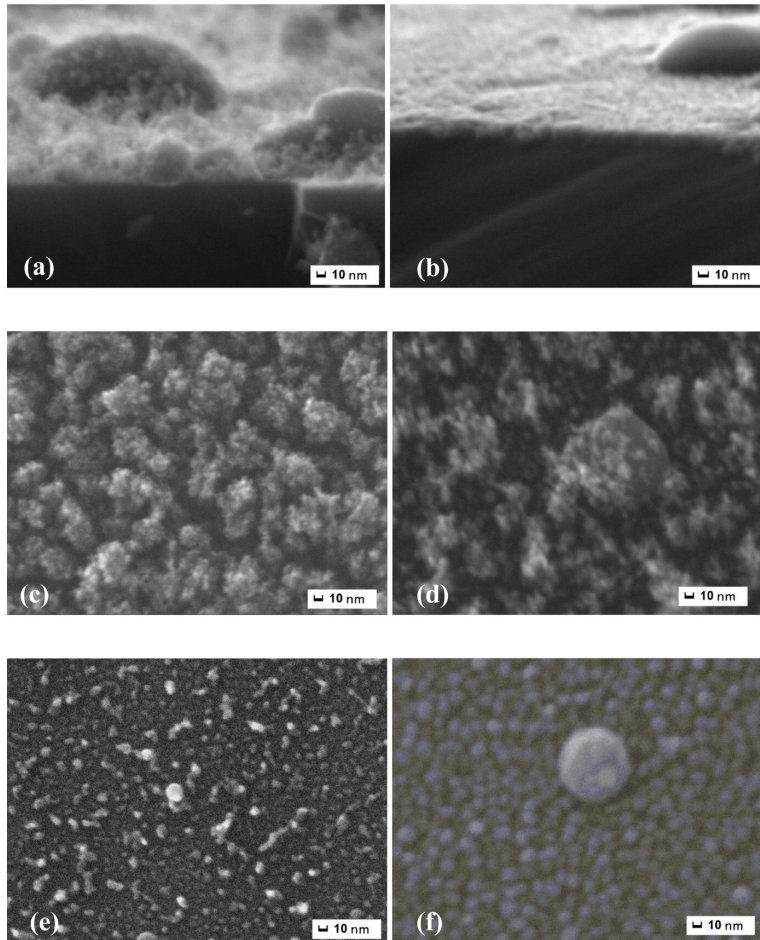
Figure 7.2: SEM analysis of (a and c) RT films, (d) AN300, (e) AN550 and (b and f) DEP300. Substrate is silicon for all samples.
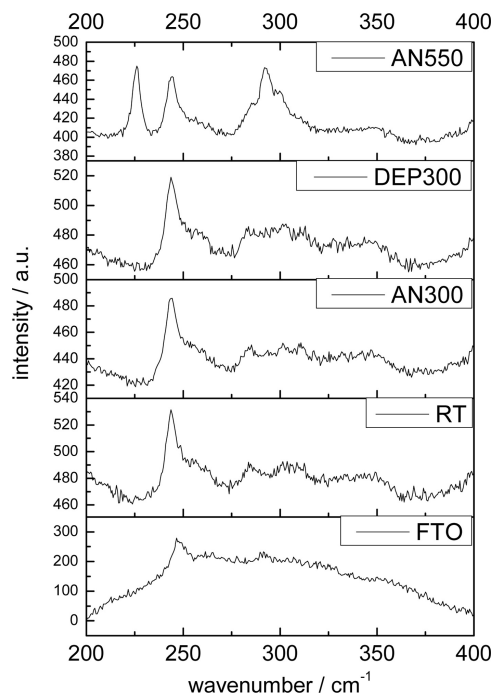
Figure 7.3: Raman spectra on FTO substrates.

plume expansion, and promotes collisions between ablated particles. This results in the formation of nanoclusters in the plume, which are cooled down by the background gas before reaching the substrate where they create a porous structure. By contrast, in lower pressure conditions, the plume expansion is less confined, the ablated material retains a higher kinetic energy, and the higher mobility allows aggregation of the particles after deposition on the substrate. The result is a more dense microstructure composed of partially assembled NPs [22, 23].

Raman analysis (Figure 7.3) reveals the presence of the crystalline hematite main peaks [24] at 226 and 292 cm^{-1} only in the case of AN550. All other samples show spectra with features not clearly different from the FTO reference. This is an indication of the largely amorphous nature of the deposited material, which is known to yield better OER catalysis performance than the crystalline phase [25]. XPS analysis confirmed that the only oxidation state of iron is Fe(III) in all samples.

From the analysis of UV–VIS absorption spectra on quartz substrates (Figure 7.4), two important observations emerge: (1) the sample DEP300 shows a much higher absorbance in all the investigated range; (2) the absorbance correlates with morphology in the direction of higher values for more compact films.

Given that the only varied parameter in the PLD process was the sub-
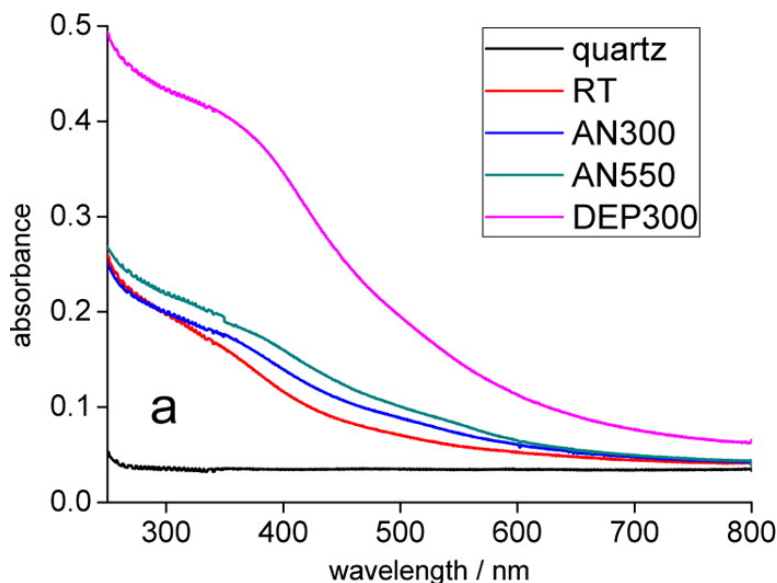
Figure 7.4: UV–VIS absorption spectra on quartz substrates.

strate temperature (RT or 300°C), the quantity of deposited material on the different samples can be considered fixed. From the absorption spectra of Fig. 7.4 the difference between RT and DEP300 is all the more striking. The reason for this behavior probably lies in the different morphology of the films. DEP300 is essentially a 2-D thin film, although with a nanostructured surface, whereas RT sample exhibits a 3-D architecture with scattered big particles and a substantial fraction of the surface composed of very small particles (5 ± 2 nm). In this latter case, a reasonable hypothesis is that a size effect in the form of optical quantum confinement dominates the optical properties, as reported for other materials [26] and for other nanosized hematite films [27, 28]. A recent investigation [17] observed a remarkable blueshift of up to 0.3 eV for both direct and indirect transitions when decreasing a hematite film thickness from 20 to 4 nm, leading to a high degree of transparency in the visible region. The effect is size-dependent and ascribed by the authors to quantum confinement.

Reducing hematite particle diameter to the 5 ± 2 nm level could help alleviate the problem of a very short hole diffusion length [29], lying in the nanometer range, but the resulting low absorption is an issue in the design of photoactive devices based on a single material. This effect can instead be exploited to functionalize an absorber with a transparent iron oxide OER catalyst.

Fe_2O_3 is stable in alkaline environment (pH > 9.8), so electrochemical water oxidation experiments were performed at pH 14 (1 M NaOH) to ensure a well-defined electrochemistry. The oxygen evolution is expected at
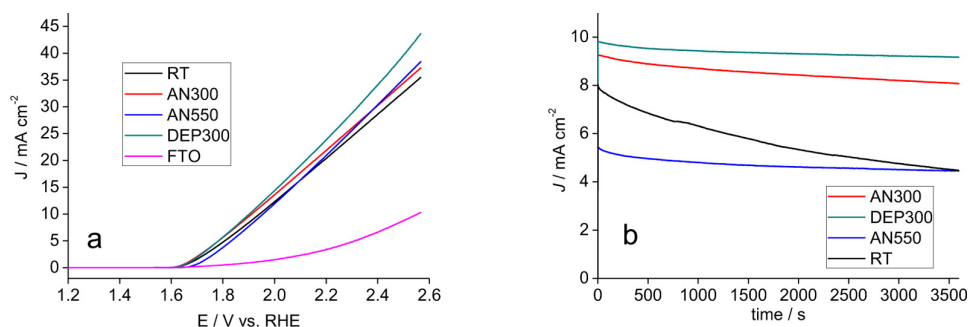
Figure 7.5: (a) Linear sweep voltammetry on FTO electrodes and (b) chronoamperometry at 1.83 V vs RHE.

potential more positive than 1.23 V vs RHE. Figure 7.5(a) illustrates the current responses of the amorphous iron oxide films cast on FTO along with that of a bare FTO taken as a reference.

The linear scan reveals that all samples are active toward water oxidation, with both DEP300 and AN300 showing considerable electroactivity with overpotentials (taken at current density $j = 0.2$ mAcm^{-2}) of 408 and 433 mV, respectively. However, the current response of RT films decreased considerably during a constant potential electrolysis experiment at 1.83 V vs RHE, designed to test film stability under operational conditions at moderate current densities (Fig. 7.5(b)). The current density loss for RT films is of 44%, whereas DEP300 is substantially stable with only a 6% loss. AN300 and AN550 show an intermediate stability with a relative decrease of $10 - 11\%$. In the case of RT films, the performance degradation is irreversible and is due to detachment of active material. Conversely, the initial performance of AN300 was reobtained on successive $j - V$ scans after restoring the electrode by abundant rinsing with water and heating at 80°C in air for 2 h. In this case, the current decrease during electrolysis may originate by adsorption of molecular oxygen, ions, and oxidation intermediates, limiting the active surface of the electrode, rather than by mechanical detachment of a-Fe$_2$O$_3$.

From a purely electrocatalytic point of view, DEP300 is the best electrode, with $j = 41.2$ mAcm^{-2} at 2.53 V vs RHE, whereas AN550 is limited to 36 mAcm^{-2} at the same potential value, confirming that the amorphous material is a better catalyst than crystalline hematite, as reported by recent literature [25, 30].

To verify the application of these iron-based catalysts in photocatalytic devices, HTL electrodes prepared by spin-coating have been functionalized by PLD with AN300 and DEP300 iron-based structures (indicated as HTL–AN300 and HTL–DEP300). The current–voltage behavior of the modified HTLs, recorded by scanning the photoelectrodes under AM1.5G illumination
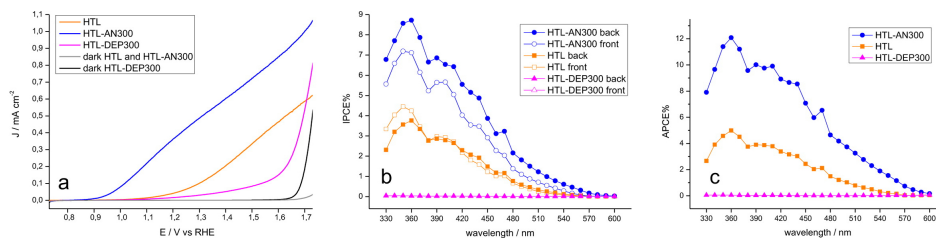
Figure 7.6: (a) $j - V$ curves of HTL, HTL–AN300, and HTL–DEP300 recorded under AM1.5G illumination (100 mWcm^{-2}) and in the dark in 0.1 M NaOH (pH 13.3). (b) IPCE spectra of the same samples recorded at 1.5 V vs RHE shining the electrodes from both the back (full symbols) and front side (empty symbols). (c) APCE spectra of the photoelectrodes reported in panel b.

(at 100 mWcm^{-2} simulated sunlight) in 0.1 M NaOH (pH 13.3), reveals a significantly improved photoelectrode performance after the functionalization with AN300 (Figure 7.6(a)). The photocurrent improves along the whole potential region of interest, reaching 0.4 mAcm^{-2} at 1.23 V vs RHE with respect to $\approx$ 0.08 mAcm^{-2} for the unmodified HTL at the same potential. The curve of HTL–AN300 also shows a cathodic shift of the photocurrent onset of about 200 mV (about 0.9 V vs RHE for HTL–AN300 with respect to 1.1 V vs RHE observed for the bare HTL film) representing, so far, one of the most prominent OEC-induced decreases in photoanodic overpotential [31, 32]. Differently, the functionalization of HTL with the more compact DEP300 has an adverse effect on the photocurrent generation. The "dark" catalytic effect of DEP300 is evident from the rising of the anodic discharge starting at about 1.6 V vs RHE, but the photocurrent generated at lower applied bias is largely inferior to that observed with the unmodified HTL, suggesting a significant degree of recombination or the blocking of the hole transfer from the underlying HTL, where photocharge is generated, to the electrolyte.

IPCE spectra recorded at 1.5 V vs RHE are consistent with the $j - V$ response discussed above, showing better charge generation and transfer properties for the AN300 modified photoelectrode (Figure 7.6(b)). Given the nanometer thicknesses of the photoelectrode and of the catalytic overlayer, no large differences were observed by changing the illumination mode from back (contact side) to front (electrolyte side), ruling out a parasitic effect of the catalysts on the absorption capability of the semiconductor. IPCE spectra collected in back and front mode are indeed nearly superimposable, with only a slight improvement in the absolute values of photon to electron conversion observed in back illumination mode, consistent with the shorter electron collection path.

APCE spectra (Figure 7.6(c)) corroborate the piece of evidence gained
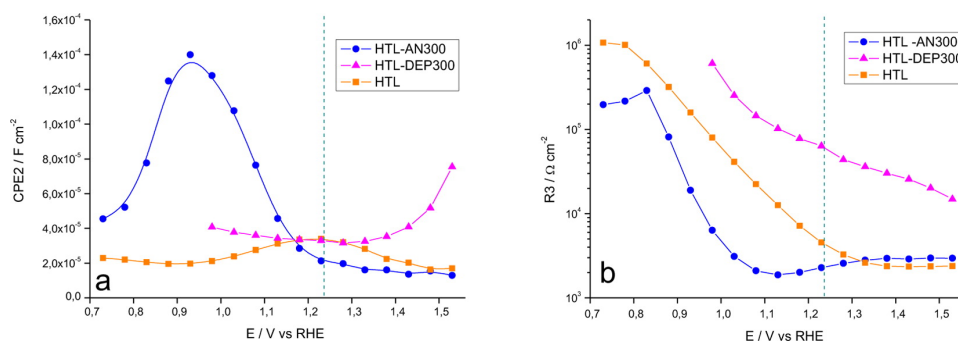
Figure 7.7: (a) CPE2 and (b) R3 plot of HTL, HTL–AN300, and HTL–DEP300 recorded under AM1.5G illumination in 0.1 M NaOH (pH 13.3). The dotted vertical bar in the graphs indicates the thermodynamic potential of water oxidation.

from the IPCE measurements, showing that the HTL–AN300 photoelectrode is intrinsically able to generate and separate photocharge with an efficiency which is at least twice that of the unmodified HTL.

Electrochemical impedance spectroscopy (EIS) data allowed us to obtain more precise information about the nature of the charge transfer processes and were interpreted with the simplified equivalent circuit reported in previous contributions [18, 33, 34] and in Figure 7.1, comprising a nested mesh describing both the charge transfer across the depletion layer (R2–CPE1) and the Helmholtz double-layer (R3–CPE2). The charge transfer resistance (R3) associated with the trapping of holes in surface states is the dominating resistive component in the interfacial dynamics of these type of hematite photoelectrodes. The capacitance associated with such resistance (CPE2) follows in both HTL and HTL–AN300 a bell-shaped distribution typical of the trapping of photoholes in surface states (Figure 7.7(a)), leading to the generation of highly valent reactive states responsible for the formation of Fe(IV)=O type reactive species, which are considered the first key intermediates for the oxygen evolution reaction [35]. The trapped photohole capacitance undergoes indeed a negative shift and a significant enhancement in the presence of the porous AN300 catalyst (1.56×10^{-5} and 4.56×10^{-5} F for the integrated values of HTL and HTL–AN300 respectively), justifying the improved performances of the latter. The formation of oxidized catalyst states in the porous layer must be compensated by the exchange of ions (namely, OH^- and H^+/Na^+) with the electrolyte probably resulting in the formation of an adaptive junction with the semiconductor [13], where the Fermi level of the photoactive semiconductor is essentially unpinned from that of the amorphous catalyst present in the form of highly nanostructured or discontinuous islands. The trapping of holes corresponding to formation and stabilization of Fe(IV) species, revealed clearly by EIS, should automat-
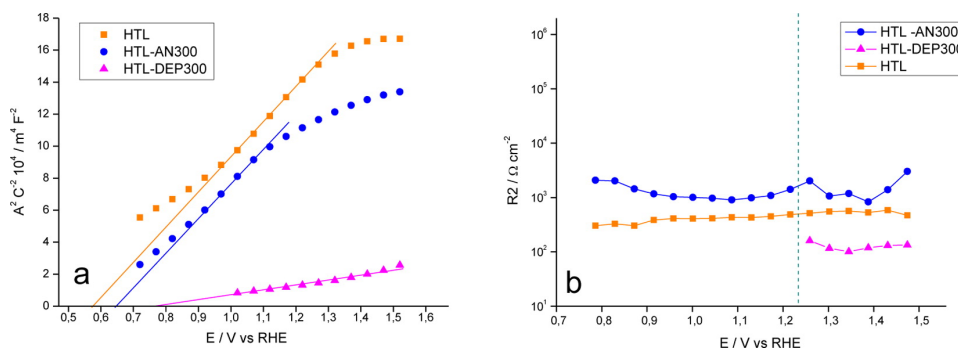
Figure 7.8: (a) Mott–Schottky plot recorded at 100 Hz under AM1.5G illumination in 0.1 M NaOH (pH 13.3) for HTL, HTL–AN300, and HTL–DEP300. (b) R2 plot of the same samples.

ically imply a variation of the Fermi level of the catalyst that is able to move independently from that of the semiconductor. APCE spectra (Fig. 7.6(c)) rule out a role of light absorption in explaining the improved performance of the HTL–AN300, consistent with EIS result being able to separate photocharge with a maximum internal efficiency that is about twice that of the unmodified HTL. It should be noted that the charge transfer resistance shows a broad minimum corresponding to the capacitance maximum of the HTL–AN300 (Fig. 7.7(b)), corroborating the correlation between improved surface trap capacitance and reduced charge transfer resistance of the interface. By contrast, the compact catalytic film (DEP300) is seemingly unable to trap holes, with the interfacial capacitance being essentially constant and at low values (about 3.5×10^{-5} Fcm^{-2}) within the whole potential interval where photocurrent is observed, only showing a sizable increase at potentials corresponding to the dark anodic discharge (Fig. 7.7(a)) where the Fermi level under potentiostatic control intercepts directly the electrochemically active sites of the DEP300 film. The reduced performance of the compact modified HTL–DEP300 junction might be due to both the compact morphology of DEP300, offering a smaller number of reactive sites where photoholes could trap, and to the lower permeability of this compact layer to the electrolyte, which does not allow charge to compensate as easily as in the AN300 layer the trapping of photoholes with the movement of anions to and from the electrolyte. Consistent with such hypothesis, the charge transfer resistance is significantly higher than that in both HTL and HTL–AN300 (Fig. 7.7(b)), steadily decreasing in an almost linear fashion with the increasing potential, instead of sharply dropping as observed in the latter cases.

Finally, the 100 Hz Mott–Schottky plots show a linear behavior of the $1/C^2$ versus applied potential, in agreement with the formation of a depletion layer (Figure 7.8(a)). The donor density (about 3×10^{17} cm^{-3}) for the

HTL and HTL–AN300 agree with previously found values for similar type of electrodes fabricated by our groups [18]. By contrast, although the HTL–DEP300 shows a linear behavior as well, a tenfold increased donor density $(2\times10^{18}\ \text{cm}^{-3})$ is found, suggesting that the depletion layer may extend into the amorphous compact layer having a larger number of defects that contribute to boosting the overall donor density. This effect could be useful to improve the overall n-type conductivity of the thin films; the resistance associated with the depletion layer (R2) is indeed smaller in the HTL–DEP300 with respect to the other two electrode types (Figure 7.8(b)) but will be quite irrelevant in determining the performance of combined films having an overall thickness of less than 50 nm. Most importantly, the involvement of the space charge layer within the DEP300 is consistent with the fact that Fermi level variations within the catalytic DEP300 film occur by acting on the width of the depletion layer rather than by charge compensation with the electrolyte and that the Fermi levels of the crystalline photoelectrode and of the catalyst are not able to move independently of each other. Photoholes will thus have to travel from the crystalline layer through the defective amorphous DEP300 layer, being exposed to recombination reactions, before reaching the interface with the electrolyte where scavenging, leading to oxygen evolution, could finally occur. This explains the lack of a distinct hole-trapping capacitance peak as well as the low capacitance values and the high charge transfer resistance, consistent with DEP300 behaving, in practice, as an intermediate hole-blocking interface, resulting in a large decrease of the photocurrent with respect of that of the unmodified sample. Only the dark electrochemical discharge will be evident in the combined HTL–DEP300 electrode, as indeed experimentally observed, when the applied potential, moving further to anodic values, directly intercepts the redox active sites of the catalyst.

7.4   Conclusions

PLD, an easily scalable fabrication technique already applied in a variety of industrial processes [36], proves to be a versatile method to control morphology at the nanometric scale, thus allowing a systematic investigation of morphological and electronic effects on the properties of functional materials. In the present chapter, we have described the PLD of a porous amorphous Fe_2O_3 OEC based on a nanoparticle-assembled coating morphology. This coating is found to be highly transparent in the visible range possibly due to a quantum confinement effect induced by the size of the nanostructures in the order of few nanometers and to retain the previously documented catalytic activity. Unfortunately, the catalytic layer is unstable under electrocatalytic conditions in the presence of moderate current densities ($< 10\ \text{mAcm}^{-2}$).

A simple low-temperature thermal treatment (300°C in air) was found to improve film stability enough for its successful application as catalytic overcoating for hematite thin film photoanodes, resulting in a dramatic decrease (of about 200 mV) of the photocurrent onset and a remarkable fivefold increase in the photocurrents detected in a photoelectrochemical cell. We believe that this is among the most prominent catalytic effects obtained from the coupling of a surface OEC with a thin layer absorber. By contrast, functionalization of the hematite photoanodes with a more compact catalyst morphology, exhibiting better electrocatalytic properties, is detrimental to photocurrent generation. In our case, $j - V$ curves under illumination, IPCE analysis, and EIS point to the nature of the absorber/catalyst junction rather than to the parasitic light blocking as the dominant factor in determining the PEC performance. Indeed, APCE and EIS data are consistent with a much better charge separation in the porous morphology, which may stem from the formation of an adaptive junction allowing for the efficient storage of photogenerated holes within the porous catalyst. By contrast, the compact overlayer probably forms a buried junction, inhibiting hole transfer to the electrolyte.

Regarding parasitic light absorption, while not critical in this case, likely due to the low thickness of the coatings (< 20 nm for the compact film), the high transmittance, and solvent permeability of the porous morphology opens up the possibility of employing higher mass loadings of catalyst without loss of performance. This would be especially beneficial for Earth-abundant, cheap, and scalable materials such as iron oxides.

On the base of the results of Chapter 8, this work will be extended to intrinsically more active species such as mixed-metal oxides. Work is in progress in our laboratory to study amorphous nickel–iron oxide deposited through PLD using the same procedure described here.

References for Chapter 7

[1] W. Rüttinger and G. C. Dismukes. "Synthetic Water-Oxidation Catalysts for Artificial Photosynthetic Water Oxidation". In: *Chem. Rev.* 97.1 (1997).

[2] N. S. Lewis. "Light Work with Water". In: *Nature* 414 (2001), pp. 589–590. DOI: 10.1038/414589a.

[3] P. V. Kamat and J. Bisquert. "Solar Fuels. Photocatalytic Hydrogen Generation". In: *J. Phys. Chem. C* 117 (2013), pp. 14873–14875. DOI: 10.1021/jp406523w.

[4] W. J. Youngblood et al. "Photoassisted Overall Water Splitting in a Visible Light-Absorbing Dye-Sensitized Photoelectrochemical Cell".

112

In: *J. Am. Chem. Soc.* 131 (2009), pp. 926–927. DOI: 10.1021/ja809108y.

[5]   S. Y. Reece et al. "Wireless Solar Water Splitting Using Silicon-Based Semiconductors and Earth-Abundant Catalysts". In: *Science* 334 (2011), pp. 645–648. DOI: 10.1126/science.1209816.

[6]   V. Cristino et al. "Efficient Solar Water Oxidation using Photovoltaic Devices Functionalized with Earth-abundant Oxygen Evolving Catalysts". In: *Phys. Chem. Chem. Phys.* 15 (2013), pp. 13083–13092. DOI: 10.1039/c3cp52237g.

[7]   M. Orlandi et al. "Ruthenium Polyoxometalate Water Splitting Catalyst: Very Fast Hole Scavenging from Photogenerated Oxidants". In: *Chem. Commun.* 46 (2010), pp. 3152–3154. DOI: 10.1039/b926823e.

[8]   B. Klahr et al. "Photoelectrochemical and Impedance Spectroscopic Investigation of Water Oxidation with "Co-Pi"-coated Hematite Electrodes". In: *J. Am. Chem. Soc.* 134 (2012), pp. 16693–16700. DOI: 10.1021/ja306427f.

[9]   J. Sun, D. K. Zhong, and D. R. Gamelin. "Composite Photoanodes for Photoelectrochemical Solar Water Splitting". In: *Energy Environ. Sci.* 3 (2010), pp. 1252–1261. DOI: 10.1039/c0ee00030b.

[10]   A. Sartorel et al. "Tetrametallic Molecular Catalysts for Photochemical Water Oxidation". In: *Chem. Soc. Rev.* 42 (2013), pp. 2262–2280. DOI: 10.1039/C2CS35287G.

[11]   H. Ye, H. S. Park, and A. J. Bard. "Screening of Electrocatalysts for Photoelectrochemical Water Oxidation on W-Doped $BiVO_4$ Photocatalysts by Scanning Electrochemical Microscopy". In: *J. Phys. Chem. C* 115 (2011), pp. 12464–12470. DOI: 10.1021/jp200852c.

[12]   J. R. McKone, N. S. Lewis, and H. B. Gray. "Will Solar-Driven Water-Splitting Devices See the Light of Day?" In: *Chem. Mater.* 26 (2014), pp. 407–414. DOI: 10.1021/cm4021518.

[13]   F. Lin and S. W. Boettcher. "Adaptive semiconductor/electrocatalyst junctions in water-splitting photoanodes". In: *Nature Materials* 13 (2013), pp. 81–86. DOI: 10.1038/nmat3811.

[14]   L. Trotochaud, T. J. Mills, and S. W. Boettcher. "An Optocatalytic Model for Semiconductor-Catalyst Water-Splitting Photoelectrodes Based on In Situ Optical Measurements on Operational Catalysts". In: *J. Phys. Chem.* 4 (2013), pp. 931–935. DOI: 10.1021/jz4002604.

[15]   E. J. Popczun et al. "Nanostructured Nickel Phosphide as an Electrocatalyst for the Hydrogen Evolution Reaction". In: *J. Am. Chem. Soc.* 135 (2013), pp. 9267–9270. DOI: 10.1021/ja403440e.

[16] J. R. McKone et al. "Ni–Mo Nanopowders for Efficient Electrochemical Hydrogen Evolution". In: *ACS Catal.* 3 (2013), pp. 166–169. DOI: 10.1021/cs300691m.

[17] M. Fondell et al. "Optical Quantum Confinement in Low Dimensional Hematite". In: *J. Mater. Chem. A* 2 (2014), p. 3352. DOI: 10.1039/c3ta14846g.

[18] N. Dalle Carbonare et al. "Improvement of the Electron Collection Efficiency in Porous Hematite Using a Thin Iron Oxide Underlayer: Towards Efficient All-Iron Based Photoelectrodes". In: *Phys. Chem. Chem. Phys.* 17 (2015), pp. 29661–29670. DOI: 10.1039/C5CP04152J.

[19] P. C. K. Vesborg and T. F. Jaramillo. "Addressing the terawatt challenge: scalability in the supply of chemical elements for renewable energy". In: *RSC Advances* 2 (2012), pp. 7933–7947. DOI: 10.1039/c2ra20839c.

[20] M. Bonelli, C. Cestari, and A. Miotello. "Pulsed laser deposition apparatus for applied research". In: *Meas. Sci. Technol.* 10 (1999), pp. 97752–97754. DOI: 10.1088/0957-0233/10/3/024.

[21] M. Orlandi et al. "Pulsed-Laser Deposition of Nanostructured Iron Oxide Catalysts for Efficient Water Oxidation". In: *ACS Appl. Mater. Interfaces* 6 (2014), pp. 6186–6190. DOI: 10.1021/am501021e.

[22] A. Infortuna, A. S. Harvey, and L. J. Gauckler. "Microstructures of CGO and YSZ Thin Films by Pulsed Laser Deposition". In: *Adv. Funct. Mater.* 18 (2008), pp. 127–135. DOI: 10.1002/adfm.200700136.

[23] I. Petrov et al. "Microstructural Evolution During Film Growth". In: *J. Vac. Sci. Technol., A* 21 (2003), S117–S128. DOI: 10.1116/1.1601610.

[24] A. M. Jubb and H. C. Allen. "Vibrational Spectroscopic Characterization of Hematite, Maghemite, and Magnetite Thin Films Produced by Vapor Deposition". In: *ACS Appl. Mater. Interfaces* 2 (2010), pp. 2804–2812. DOI: 10.1021/am1004943.

[25] R. D. L. Smith et al. "Photochemical Route for Accessing Amorphous Metal Oxide Materials for Water Oxidation Catalysis". In: *Science* 340 (2013), p. 60. DOI: 10.1126/science.1233638.

[26] D. Raymand et al. "Investigation of Vibrational Modes and Phonon Density of States in ZnO Quantum Dots". In: *J. Phys. Chem. C* 116 (2012), pp. 6893–6901. DOI: 10.1021/jp300985k.

[27] K. Sivula et al. "Photoelectrochemical Water Splitting with Mesoporous Hematite Prepared by a Solution-Based Colloidal Approach". In: *J. Am. Chem. Soc.* 132 (2010), pp. 7436–7444. DOI: 10.1021/ja101564f.

[28] L. Vayssieres et al. "One-Dimensional Quantum-Confinement Effect in α-Fe$_2$O$_3$ Ultrafine Nanorod Arrays". In: *Adv. Mater.* 17 (2005), pp. 2320–2323. DOI: 10.1002/adma.200500992.

[29] B. M. Klahr, A. B. Martinson, and T. W. Hamann. "Photoelectrochemical Investigation of Ultrathin Film Iron Oxide Solar Cells Prepared by Atomic Layer Deposition". In: *Langmuir* 27 (2011), pp. 461–468. DOI: 10.1021/la103541n.

[30] R. D. L. Smith et al. "Water Oxidation Catalysis: Electrocatalytic Response to Metal Stoichiometry in Amorphous Metal Oxide Films Containing Iron, Cobalt, and Nickel". In: *J. Am. Chem. Soc.* 135 (2013), pp. 11580–11586. DOI: 10.1021/ja403102j.

[31] S. D. Tilley et al. "Light-induced Water Splitting with Hematite: Improved Nanostructure and Iridium Oxide Catalysis". In: *Angew. Chem. Int. Ed.* 49 (2010), pp. 6405–6408. DOI: 10.1002/anie.201003110.

[32] K. M. H. Young and T. W. Hamann. "Enhanced Photocatalytic Water Oxidation Efficiency with Ni(OH)$_2$ Catalysts Deposited on α-Fe$_2$O$_3$ via ALD". In: *Chem. Commun.* 50 (2014), pp. 8727–8730. DOI: 10.1039/C4CC02598A.

[33] B. Klahr et al. "Water Oxidation at Hematite Photoelectrodes: The Role of Surface States". In: *J. Am. Chem. Soc.* 134 (2012), pp. 4294–4302. DOI: 10.1021/ja210755h.

[34] D. Monllor-Satoca et al. "What Do You Do, Titanium? Insight Into the Role of Titanium Oxide as a Water Oxidation Promoter in Hematite-Based Photoanodes". In: *Energy Environ. Sci.* 8 (2015), pp. 3242–3254. DOI: 10.1039/C5EE01679G.

[35] B. Klahr et al. "Electrochemical and Photoelectrochemical Investigation of Water Oxidation with Hematite Electrodes". In: *Energy Environ. Sci.* 5 (2012), pp. 7626–7636. DOI: 10.1039/c2ee21414h.

[36] M. C. Gower. "Industrial Applications of Laser Micromachining". In: *Opt. Express* 7 (2000), pp. 56–67. DOI: 10.1364/OE.7.000056.

Chapter 8

Physical vapor deposition of mixed-metal oxides based on Fe, Co and Ni as water oxidation catalysts

Preview   Here we present a systematic study of water oxidation catalysts based on Fe, Co and Ni oxides. Physical vapor deposition techniques are proposed as scalable, industrially viable methods to synthesize mixed-metal oxides thin films. In agreement with recent literature, $NiFe_2O_x$ resulted as good choice as an oxygen evolution catalyst.

   This study can be combined with that presented in Chapter 7: the PLD synthesis of nickel–iron mixed oxide could result in an optimal solution for the functionalization of hematite photoanodes. On this field, work is in progress in our laboratory.

The content of this chapter was adapted from:
A. Mazzi, N. Bazzanella, M. Orlandi, R. Edla, N. Patel, R. Fernandes and A. Miotello, Mater. Sci. Semicond. Process. 42 (2016), pp. 155–158.

8.1   Introduction

Solar driven efficient water splitting to produce hydrogen would be a smart solution to provide a clean, capillary and renewable energy source for human society needs [1]. A promising way to realize this goal is to couple solar energy absorbing semiconductors with high efficiency catalysts to drive the water splitting process in a photo-electrochemical cell. In particular the

oxygen evolution reaction

$$2H_2O + 4h^+ \rightarrow O_2 + 4H^+ \quad E^\circ = 1.23V \text{ vs. NHE} \tag{8.1}$$
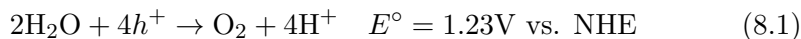
is a kinetically slow process and the development of suitable catalysts is required [2] (here h^+ indicates electron vacancies, while E^0 is the standard reversible potential of water splitting). The search for earth abundant, environmentally friendly, oxygen evolution catalysts is then a key issue to develop scalable water splitting devices [3] and, in this sense, catalysts based on iron, cobalt and nickel have recently met a growing attention from the scientific community [4]. Systematic studies on amorphous metal oxides thin films obtained by chemical deposition techniques have experimentally shown the good potentiality of mixed-metal oxides as WOC in alkaline media [5, 6].

PVD techniques can be successfully employed to deposit thin layers of pure, binary or ternary metal oxides with advantages such as: control of the amount of deposited catalyst, good adhesion on a large variety of substrates, and some degree of freedom in the design of surface morphology. In the work presented in this chapter, we employed the electron beam deposition (EBD) technique to functionalize indium–tin oxide (ITO) electrodes with thin films of CoO_x, NiO_x, $NiCo_2O_x$, $CoFe_2O_x$ and $NiFe_2O_x$, to be tested as anodes for electrochemical water splitting. FeO_x was excluded from this series for two reasons: it is reported in literature as the worst performing WOC [7] and it is technically difficult to deposit it by EBD technique.

8.2 Experimental section

Materials

Electron beam evaporation was carried out on powders of pure and binary metal oxides prepared by chemical synthesis. Reagents include $CoCl_2$ 97% Sigma–Aldrich, $NiCl_2$ 98% Sigma–Aldrich, $Co(NO_3)_2 \cdot 6H_2O$ 97.7% Alfa–Aesar, $FeCl_3 > 99\%$ Sigma–Aldrich, $Fe(NO_3)_3 \cdot 9H_2O$ 98% Sigma–Aldrich, NaOH 98% Sigma–Aldrich, NH_3 25% aq., 99.99% Alfa–Aesar.

Powder preparation

Metal oxide powders were synthesized by co-precipitation methods. Stoichiometric amounts of metal salts were dissolved in water at constant stirring, the solution was then led to basic pH by the addition of a concentrated base. Precipitated metal hydroxides/oxy-hydroxides clusters were further filtered and washed with water, methanol and isopropanol. The product was then dried at 120°C in air overnight. The dried powder was grinded and annealed in air to obtain the desired oxide phase. In order to perform safe EBD of mixed-metal oxides, the powders were cold-pressed at 5

tons/cm^2 and the pellets were then sintered by stepwise heating in a pro-grammed furnace. Details and conditions of the material preparation are shown in Tables 8.1 and 8.2.

Catalyst	Synthesis solution H$_2$O +	Precipitant, conditions
CoO$_x$	CoCl$_2$ 0.04 M	24 ml NH$_3$ 25% aq.
NiO$_x$	NiCl$_2$ 0.05 M	NaOH 0.4 M
NiCo$_2$O$_x$	NiCl$_2$ 0.06 M + Co(NO$_3$)$_2$ 0.12 M	50 ml NaOH 2 M
CoFe$_2$O$_x$	CoCl$_2$ 0.02 M + FeCl$_3$ 0.04 M	NaOH 5 M $\rightarrow$ pH> 12
NiFe$_2$O$_x$	NiCl$_2$ 0.02 M + Fe(NO$_3$)$_3$ 0.04 M	35 ml NaOH 3 M

Table 8.1: Details of chemical synthesis of pure and binary oxide powders.

Catalyst	Powder annealing	Pellet sintering
CoO$_x$	400°C 2 h	
NiO$_x$	350°C 2 h	
NiCo$_2$O$_x$	300°C 2 h	600°C 90 min
CoFe$_2$O$_x$	200°C 2 h	1000°C 90 min
NiFe$_2$O$_x$	400°C 2 h	1000°C 90 min

Table 8.2: Thermal treatments on synthesized powders.

Physical vapor deposition

WOC films were deposited by EBD on silicon (for SEM analysis and XPS measurements), glass (for Raman spectroscopy) and glass/ITO slides (for electrochemical characterization). Compact ITO films $\sim$ 400 nm thick were deposited by RF-magnetron sputtering on micro-rough glass [8].

EBD was performed using a laboratory-built evaporator system equipped with a 10 kV electron gun and 10 mA average beam current. Precursor powders or sintered pellets were placed in graphite crucibles on a water-cooled holder. Background pressure before operation was kept $\lesssim 2 \times 10^{-7}$ torr and at $2 \div 4 \times 10^{-6}$ torr during evaporation. Depositions were carried out both with the substrates at room temperature and at 300±2°C, by using an electric heater and a thermocouple control. Deposition rate was adjusted to 0.2 Å/s by using a quartz crystal transducer type deposition monitor. The use of different substrates facilitates characterization and in the case of PVD techniques without further annealing, the effect of the substrate properties on film morphology and phase seems to be negligible [9].

Material characterization

For material characterization, we deposited films with thickness in the range between 60 and 100 nm. Film thickness and surface morphology were studied by scanning electron microscopy (SEM-FEG, JSM 7001F, JEOL) at 20 keV electron beam energy. This system is also equipped with energy-dispersive spectroscopy analysis (EDS, INCA PentaFET-x3), which was employed to evaluate powder and pellet chemical composition.

Raman spectra were obtained with a Labram Aramis Jobin–Yvon Horiba μ-Raman system equipped with a He–Ne laser source (632.8 nm).

The surface composition and chemical states of each element in the samples were examined by X-ray photoelectron spectroscopy (XPS) using a Kratos AXIS Ultra$^{\text{DLD}}$ instrument equipped with a monochromatic Al K$_\alpha$ (1486.6 eV) X-ray source and a hemispherical analyzer. Charge compensation was necessary to perform the analysis and binding energy was referenced to the C 1s peak. XPS peaks were identified according with the handbook of XPS [10].

Electrochemical measurements

A set of thin films (10 ± 1 nm, calibrated after SEM cross-sectional measurements) was deposited in order to evaluate catalytic activity. Electrochemical water oxidation experiments were performed using a Gamry potentiostat/galvanostat/ZRA Interface 1000 in a three-electrode cell composed by a saturated calomel electrode (SCE, 0.244 V vs. standard hydrogen electrode SHE) as reference, Pt-mesh as counter-electrode and a 1.0 M KOH solution as electrolyte. Glass/ITO/WOC (1 cm^2 area) electrodes were used as working electrodes. Silver paint was applied to a bare portion of ITO to obtain a good electric contact. Cyclic voltammetries (CV) in the potential range $[-0.244, 1.756]$ V vs. SCE were performed to stabilize the electrodes (10 cycles). Then, to observe eventual precatalytic oxidation peaks a single CV cycle was done in the potential range $[-0.244, 0.756]$ V vs. SCE. Linear sweep voltammetries (LSV) were operated after 1 minute constant potential conditioning, which was needed to remove the precatalytic peaks. LSV measurements were carried out starting from the observed current peaks, up to reach current densities larger than 10 mA/cm^2. Both CV and LSV curves were collected at a scan rate of 10 mV/s. Measurements at a faster scan rate (100 mV/s) show a similar qualitative behavior and are not reported here. All measurements were done in static solution and data are corrected for uncompensated resistance (R_u), using current interrupt iR compensation. Electrochemical potentials given in this chapter are relative to the reversible hydrogen electrode (RHE), with pH correction:

$$E_{\text{RHE}} = E_{\text{applied}} + 0.244\text{V} + 0.059 \cdot \text{pH} - iR_u. \tag{8.2}$$

8.3 Results and discussion

Powders and pellets for EBD

The materials ready to be used for EBD (annealed powders for pure oxides and sintered pellets for binary oxides) were characterized by EDS, whose results, summarized in Table 8.3, proved good material homogeneity. The synthesized materials are consistent with Co_3O_4, NiO, $NiCo_2O_4$, $CoFe_2O_4$ and $NiFe_2O_4$. The observed excess of oxygen in the samples can be justified by the presence of eventual surface contaminants.

Catalyst	Area	Stoichiometry
CoO_x	$100 \times 100 \ \mu$m	Co:O = 1.00 : 1.41 ($\pm$0.04)
NiO_x	$100 \times 100 \ \mu$m	Ni:O = 1.00 : 1.19 ($\pm$0.05)
$NiCo_2O_x$	1×1 mm	Ni:Co:O = 1.00 : 2.11 : 4.44 ($\pm$0.08)
$CoFe_2O_x$	1×1 mm	Co:Fe:O = 1.0 : 2.7 : 5.2 ($\pm$0.4)
$NiFe_2O_x$	2×2 mm	Ni:Fe:O = 1.0 : 2.1 : 4.5 ($\pm$0.1)

Table 8.3: EDS examined areas and results. Reported errors give information about material homogeneity.

Film deposition and morphology

Pure and binary metal oxides were deposited by EBD on flat and rough glass, covered with $\sim$ 400 nm ITO, both at room temperature and at 300°C. The films deposited on rough surfaces or with the substrates at 300°C resulted to be stable under electrocatalysis conditions. During preliminary work, the best catalytic behavior was found for rough glass/ITO electrodes with catalyst deposited at 300°C, and for this reason it was chosen as the standard condition for EBD. The typical morphology obtained by EBD is shown in Figure 8.1. The film is nanostructured, with typical nanoparticle size of $\sim$ 10nm.

Raman spectroscopy

Raman spectroscopy was performed on the deposited thick films on glass substrates to investigate material crystallinity and eventually to extract information about the composition; results are shown in Figure 8.2. Cobalt oxide shows the Raman peaks of the Co_3O_4 spinel structure (194.4, 482.4, 521.6, 618.4 and 691.0 cm^{-1}) and results to be partially crystalline. Also nickel–cobalt oxide has a significant crystalline degree, with quite defined peaks at 455 and 657 cm^{-1} corresponding to $NiCo_2O_4$ spinel structure, other peaks are not well identified.
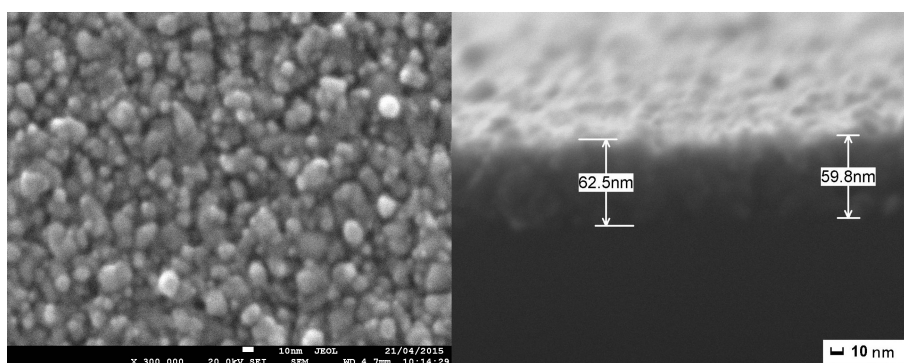
Figure 8.1: (left) Top-down view and (right) cross section SEM images of $NiCo_2O_x$ film deposited by EBD on Si at $300°C$. A small bar corresponding to 10 nm is shown for comparison.
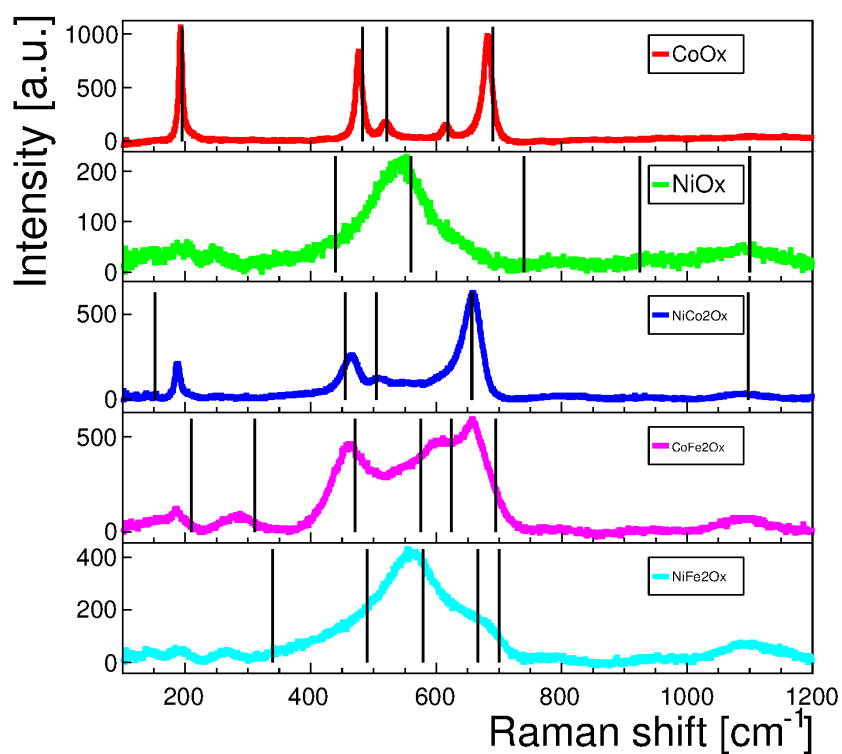
Figure 8.2: Raman spectra of materials deposited by EBD at $300°C$, compared with predicted peaks of crystalline Co_3O_4 [11], NiO [12], $NiCo_2O_4$ [13], $CoFe_2O_4$ [14] and $NiFe_2O_4$ [15].

On the other hand, nickel oxide and nickel–iron oxide show amorphous nature, with very weak Raman response (in Figure 8.2 their spectra are compared with predicted peaks of NiO cubic structure and $NiFe_2O_4$ inverse spinel, respectively). Cobalt–iron oxide shows a partially amorphous structure, with a broad band corresponding to the Raman peaks of $CoFe_2O_4$.

Electrochemical and XPS results
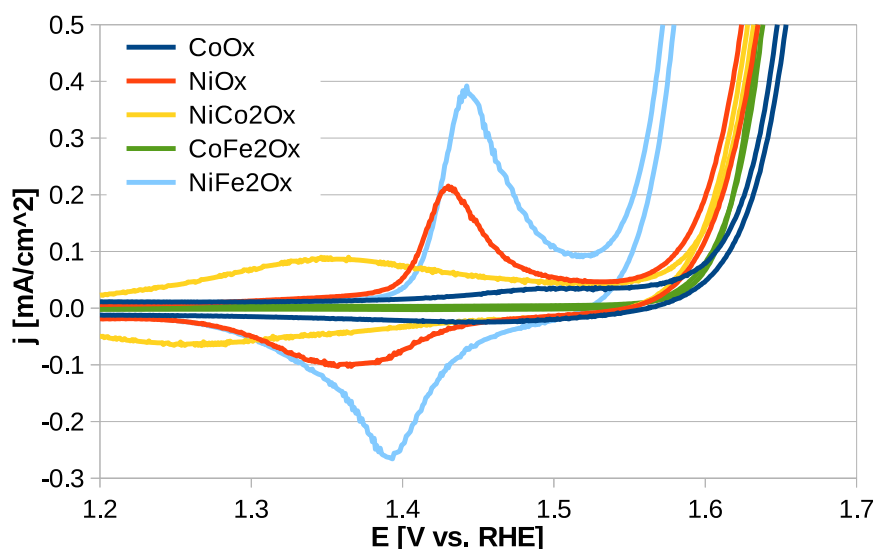
Figure 8.3: Cyclic voltammetries of pure and binary metal oxide functionalized electrodes, collected at scan rate of 10 mV/s in 1 M KOH

The catalysis onset region of cyclic voltammetry curves is expanded in Figure 8.3. In good agreement with the study of Trotochaud et al. [7] a precatalytic oxidation peak is found for pure nickel oxide at 1.43 V vs. RHE, with the associated broad reduction peak at 1.36 V. These peaks are attributed to the reversible couple $Ni(OH)_2$/NiOOH. XPS analysis reveals that Ni is present in both metallic and oxidized form, where the signature peaks of the former are at 852.9 eV and 870.35 eV assigned to $2p_{3/2}$ and $2p_{1/2}$ states respectively. The peaks centered at 854.6 eV ($2p_{3/2}$) and 873.8 eV ($2p_{1/2}$) are due to nickel oxide (NiO and $Ni(OH)_2$), whose satellite peaks are also observed at 859.60 eV and 880.7 eV. In O 1s core level the peaks at 531.8 eV and 530 eV correspond to oxygen attached in NiO and $Ni(OH)_2$ respectively. Stoichiometry and prevalent phase are given in Table 8.4 for all the catalysts.

Moreover, according to Trotochaud et al. [7], with increasing amount of cobalt the $Ni(OH)_2$/NiOOH redox activity decreases, and thus $NiCo_2O_x$ shows broader peaks at 1.35 V (ox.) and 1.26 V (red.) vs. RHE. At the

Catalyst	Stoichiometry	Possible phase
CoO_x	Co:O = 1 : 1.39 ($\pm$0.06)	Co_3O_4
NiO_x	Ni:O = 1 : 0.37 ($\pm$0.02)	NiO, Ni
$NiCo_2O_x$	Ni:Co:O = 1 : 1.95 : 3.36 ($\pm$0.1)	$NiCo_2O_4$
$CoFe_2O_x$	Co:Fe:O = 1 : 1.81 : 1.39 ($\pm$0.07)	$CoFe_2O_4$
$NiFe_2O_x$	Ni:Fe:O = 1 : 2.14 : 4.47 ($\pm$0.1)	$NiFe_2O_4$

Table 8.4: Thin film composition calculated on XPS spectra.

opposite extreme, CoO_x has quite small precatalytic signals.

XPS measurements of $NiCo_2O_x$ revealed the presence of Co^{3+} (Co_2O_3) and Ni^{2+} (NiO) together with metallic cobalt (peaks of $2p_{3/2}$ at 778 eV and $2p_{1/2}$ 792.4 eV) and nickel (peaks of $2p_{3/2}$ 852.8 eV and $2p_{1/2}$ 870.3 eV). Two well defined peaks centered at 531.6 eV and 529.5 eV correspond to oxygen in Co_2O_3 and NiO. XPS spectrum of CoO_x shows the presence of Co^{3+} and Co^{2+} oxidation states, with also shake-up peaks of the Co_3O_4 phase at 789 eV and 803.8 eV. Metallic Co is also present with peaks at 778 eV and 793.5 eV.

In Figure 8.3 $NiFe_2O_x$ shows features analogous to that of NiO_x, thus indicating the presence of active Ni^{2+} cation (1.44 V ox. and 1.39 V red. vs. RHE). Ni 2p core level shows the presence of metallic state (and oxidized Ni^{2+} state, respectively) with peaks centered at 852.8 eV (853.9 eV) of $2p_{3/2}$ level and 870.2 eV (874.9 eV) of $2p_{1/2}$. Iron is present in completely oxidized state with Fe^{3+} (and Fe^{2+}, respectively) peaks at 709.4 eV (712.5 eV) of level $2p_{3/2}$ and 723.1 eV (729.9 eV) of $2p_{1/2}$. In O 1s level the two peaks at 530.2 eV and 531.4 eV are assigned to oxygen and hydroxide attached to Fe and Ni atoms.
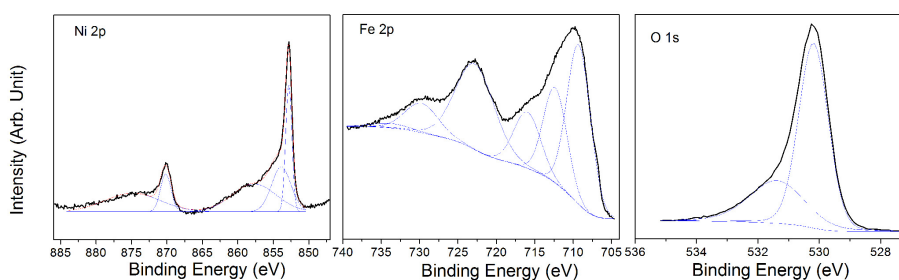
Figure 8.4: XPS spectrum of $NiFe_2O_x$ 90 nm thick on Si.

On the other hand, according to Smith et al. [5] $CoFe_2O_x$ shows almost no precatalytic oxidation process. In this case, XPS analysis shows the presence of metallic cobalt and oxide peaks of Co^{2+} ($2p_{3/2}$ at 781.44 eV and $2p_{1/2}$ at 796.06 eV). Satellite peaks corresponding to $Co(OH)_2$ are revealed at 787 and 803.2 eV. All the peaks (709.2, 712.5, 722.4, 729.8 eV) in Fe 2p

core level are assigned to the various oxides of Fe (FeO, Fe2O3, Fe3O4) with oxidation state of Fe^{2+} and Fe^{3+}. In O 1s level, two peaks at 530.1 and 531.55 eV are assigned to O in iron oxide and $Co(OH)_2$ respectively.

Catalyst	η (1 mA/cm^2)	η (10 mA/cm^2)	Tafel s. [mV/dec]
CoO_x	0.436	0.496	52.7
NiO_x	0.440	0.627	59.0
$NiCo_2O_x$	0.426	0.555	84.1
$CoFe_2O_x$	0.409	0.486	45.6
$NiFe_2O_x$	0.365	0.432	48.0

Table 8.5: Overpotential η expressed in volts and Tafel slopes.

Tafel slopes and overpotentials at $j = 1$ mA/cm^2 and $j = 10$ mA/cm^2 were measured through linear sweep voltammetries on ITO electrodes functionalized with 10 nm catalyst layer; results are summarized in Table 8.5. In agreement with recent results obtained by chemical deposition techniques, the best behavior among the binary oxides based on Fe, Co and Ni is found for nickel–iron oxide [5, 7]. Our results reveal that at $j = 1$ mA/cm^2 the other binary oxides have a higher overpotential, with a difference of about 20%. CoO_x and NiO_x show the lowest catalytic activity, motivating the research on more complex compounds. The good efficiency of $NiFe_2O_x$ amorphous film as WOC are in conclusion due to the possible synergistic activity of Ni and Fe oxides as is proved by the worse overall behavior of pure Ni and Fe oxides (see [9] for FeO_x deposited by PVD). A more detailed mechanistic study investigating the active-sites in these materials is needed to elucidate the exact nature of the observed synergistic effect.

8.4 Conclusions

In this chapter, we reported successful PVD of mixed-metal oxides based on Fe, Co and Ni to functionalize anodes for electrochemical water splitting. Material properties and their catalytic behavior are consistent with recent, high quality studies and our approach provides a very flexible fabrication technique, suitable for a large variety of materials. Nickel–iron oxide resulted as the best performing catalyst, thus our further work will be especially concentrated on the fine design of deposition conditions for this material, in order to improve its efficiency.

In particular, our next goal is to synthesize highly nanostructured thin nickel–iron oxide layers to be employed in the functionalization of hematite-based photoanodes for water oxidation. To this aim, we plan to compare other physical deposition techniques, primarily pulsed laser deposition. A first step forward is the research presented in Chapter 7. In that case, we proved a possible route to obtain a transparent highly nanostructured iron oxide layer through PLD. That strategy allows us to achieve stable improved

124

performances of hematite photoanodes.

References for Chapter 8

[1] K. Rajeshwar et al. "Renewable Energy and the Hydrogen Economy". In: *Solar Hydrogen Generation: Toward a Renewable Energy Future*. Ed. by K. Rajeshwar, R. McConnell, and S. Licht. Springer, 2008.

[2] J. Suntivich et al. "A Perovskite Oxide Optimized for Oxygen Evolution Catalysis from Molecular Orbital Principles". In: *Science* 334 (2011), p. 1383. DOI: 10.1126/science.1212858.

[3] M. G. Walter et al. "Solar Water Splitting Cells". In: *Chem. Rev.* 110 (2010), pp. 6446–6473. DOI: 10.1021/cr1002326.

[4] P. Du and R. Eisenberg. "Catalysts made of earth-abundant elements (Co, Ni, Fe) for water splitting: Recent progress and future challenges". In: *Energy Environ. Sci.* 5 (2012), p. 6012. DOI: 10.1039/C2EE03250C.

[5] R. D. L. Smith et al. "Water Oxidation Catalysis: Electrocatalytic Response to Metal Stoichiometry in Amorphous Metal Oxide Films Containing Iron, Cobalt, and Nickel". In: *J. Am. Chem. Soc.* 135 (2013), pp. 11580–11586. DOI: 10.1021/ja403102j.

[6] C. C. L. McCrory et al. "Benchmarking Heterogeneous Electrocatalysts for the Oxygen Evolution Reaction". In: *J. Am. Chem. Soc.* 135 (2013), pp. 16977–16987. DOI: 10.1021/ja407115p.

[7] L. Trotochaud et al. "Solution-Cast Metal Oxide Thin Film Electrocatalysts for Oxygen Evolution". In: *J. Am. Chem. Soc.* 134 (2012), pp. 17253–17261. DOI: 10.1021/ja307507a.

[8] E. Binetti et al. "Synthesis of mesoporous ITO/TiO_2 electrodes for optoelectronics". In: *Mater. Lett.* 139 (2015), pp. 355–358. DOI: 10.1016/j.matlet.2014.10.120.

[9] M. Orlandi et al. "Pulsed-Laser Deposition of Nanostructured Iron Oxide Catalysts for Efficient Water Oxidation". In: *ACS Appl. Mater. Interfaces* 6 (2014), pp. 6186–6190. DOI: 10.1021/am501021e.

[10] J.F. Moulder and J. Chastain. *Handbook of X-ray Photoelectron Spectroscopy*. Physical Electronics, 1995.

[11] V. G. Hadjiev, M. N. Iliev, and I. V. Vergilov. "The Raman spectra of Co_3O_4". In: *J. Phys. C: Solid State Phys.* 21 (1988), p. L199. DOI: 10.1088/0022-3719/21/7/007.

[12] R. E. Dietz, G. I. Parisot, and A. E. Meixner. "Infrared Absorption and Raman Scattering by Two-Magnon Processes in NiO". In: *Phys. Rev. B* 4 (1971), pp. 2302–2310. DOI: 10.1103/PhysRevB.4.2302.

[13] G. A. Babu, G. Ravi, and Y. Hayakawa. "Microwave synthesis and effect of CTAB on ferromagnetic properties of NiO, Co_3O_4 and $NiCo_2O_4$ nanostructures". In: *Appl. Phys. A* 119 (2015), pp. 219–232. DOI: 10.1007/s00339-014-8951-9.

[14] P. Chandramohan et al. "Cation distribution and particle size effect on Raman spectrum of $CoFe_2O_4$". In: *J. Solid State Chem.* 184 (2011), pp. 89–96. DOI: 10.1016/j.jssc.2010.10.019.

[15] P. R. Graves, C. Johnston, and J. J. Campaniello. "Raman scattering in spinel structure ferrites". In: *Mat. Res. Bull.* 23 (1988), pp. 1651–1660. DOI: 10.1016/0025-5408(88)90255-3.

126

Conclusions

In the present thesis, we collected the results of our recent research on computational and experimental topics. The work is focused on the application of physical vapor deposition techniques in the field of the photoelectrochemical synthesis of solar fuels. First, in Chapter 1 we discussed the social and economic impact of developing scalable devices to produce renewable energy. In particular, we focused on artificial photosynthesis using sunlight. Then, we analyzed the general principles and the current research on semiconductor-based solar water splitting for hydrogen production (Chapter 2). Moreover, we presented some peculiar aspects of physical vapor deposition techniques in the material fabrication for photoelectrochemical cells (Chapter 3). In particular, we put our attention on pulsed laser deposition as a very flexible and industrially scalable method to synthesize nanostructured, stable materials.

Then, we reviewed our results on the modeling of the fundamental mechanisms in the nanosecond laser ablation of metals. In Chapter 4 we discussed an original approach to describe the phase explosion process through a continuum approach, based on thermodynamics. This ablation mechanism, which was recognized as the most relevant in the high energy nanosecond laser ablation of metals, allows the direct nanoparticle formation and ejection from the target. We developed our computational method relying on the theory of homogeneous boiling, which allows us to simulate vapor bubble nucleation in a metastable liquid, followed by the identification of the liquid nanoclusters that are formed. The final result of our work on this topic is a dynamic simulation, presented in Chapter 5, which considers physically meaningful approximations and a detailed vapor bubble dynamics. This computational study allowed us to come to a more quantitative description of the phase explosion process, especially as regards its timing and the size distribution of the ejected nanoclusters.

We applied physical vapor deposition techniques in the synthesis of photoanodic materials for water oxidation. In particular, in Chapter 6, we described a procedure based on radiofrequency magnetron sputtering to synthesize tin-doped hematite thin films. This method allowed us to systematically study the effect of tin doping on the properties of hematite as an anodic material, by showing a remarkable improvement of the charge trans-

port and transfer properties with respect to pure hematite. Furthermore, we studied water oxidation catalysts, which are useful to build integrated absorber/electrocatalyst photoanodes. In particular, we varied catalyst stoichiometry to analyze several pure and mixed-metal oxides, based on earth abundant transition metals (Chapter 8). Moreover, we studied a strategy for the optimization of the electrochemical and optical properties of the electrocatalyst layer, based on the flexibility of pulsed laser deposition technique (Chapter 7). An amorphous, highly nanostructured iron oxide catalyst was studied in depth and successfully employed to functionalize crystalline hematite photoanodes.

Our experimental results can be exploited all together in the next future, by developing integrated photoanodes entirely obtained through physical vapor deposition techniques. Solar active tin-doped hematite could be obtained through radiofrequency magnetron sputtering, for example by arranging its nanostructuring. To this purpose, several solutions adopted in recent literature in the sputtering deposition of semiconductors are available (mesoporous films, scaffold architectures...). Furthermore, we could take advantage of our achievements in the synthesis of transparent amorphous water oxidation electrocatalysts: mixed nickel–iron oxide or nickel-doped iron oxide can be deposited by pulsed laser deposition on tin-doped hematite films, by obtaining an integrated, optimized photoanode.

List of publications

1. N. Vianello, C. Rea, M. Agostini, R. Cavazzana, G. Ciaccio, G. De Masi, E. Martines, A. Mazzi, B. Momo, G. Spizzo, P. Scarin, M. Spolaore, P. Zanca, M. Zuin, L. Carraro, P. Innocente, L. Marrelli, M.E. Puiatti, D. Terranova and the RFX-mod Team. Magnetic perturbations as a viable tool for edge turbulence modification. Plasma Phys. Control. Fus. 57 (2015) 014027.

2. M. Spolaore, M. Agostini, B. Momo, C. Rea, N. Vianello, M. Zuin, R. Cavazzana, G. De Masi, P. Innocente, L. Marrelli, E. Martines, A. Mazzi, M.E. Puiatti, S. Spagnolo, G. Spizzo, P. Scarin, D. Terranova and P. Zanca. Turbulent electromagnetic filaments in actively modulated toroidal plasma edge. Nucl. Fus. 55 (2015) 063041.

3. A. Mazzi, F. Gorrini and A. Miotello. Liquid nanodroplet formation through phase explosion mechanism in laser-irradiated metal targets. Phys. Rev. E 92 (2015) 031301(R).

4. A. Mazzi, N. Bazzanella, M. Orlandi, R. Edla, N. Patel, R. Fernandes and A. Miotello. Physical vapor deposition of mixed-metal oxides based on Fe, Co and Ni as water oxidation catalysts. Mater. Sci. Semicond. Process. 42 (2016) 155–158.

5. M. Orlandi, A. Mazzi, G. Arban, N. Bazzanella, P. Rudatis, S. Caramori, N. Patel, R. Fernandes, C. Bignozzi and A. Miotello. On the effect of Sn-doping in hematite anodes for oxygen evolution. Electrochim. Acta 214 (2016) 345–353.

6. M. Orlandi, N. Dalle Carbonare, S. Caramori, C. Bignozzi, S. Berardi, A. Mazzi, Z. El Koura, N. Bazzanella, N. Patel and A. Miotello. Porous versus compact nanosized Fe(III) based water oxidation catalyst for photoanode functionalization. ACS Appl. Mater. Interfaces 8 (2016) 20003–20011.

7. A. Mazzi and A. Miotello. Simulation of phase explosion in the nanosecond laser ablation of aluminum. J. Colloid Interface Sci. 489 (2017) 126–130.

8. A. Mazzi, F. Gorrini and A. Miotello. Dynamics of liquid nanodroplet formation in nanosecond laser ablation of metals. Appl. Surf. Sci. (2016) http://dx.doi.org/10.1016/j.apsusc.2016.09.006 (Article In Press).

Acknowledgments

In the work presented here, I have been supported by a large number of people, including professors, colleagues, friends and of course my family. Here, I would like to acknowledge all the people that helped me during my doctoral studies, those who contributed to my scientific work, but especially those who believed in me and encouraged me to pursue my objectives. I feel indebted with all of these people and I would like to express my gratitude to some of them for special reasons.

I am grateful to my supervisor, prof. Antonio Miotello, who gave me the opportunity to join the IdEA Laboratory at the University of Trento. His wise guidance has been essential during my PhD period, in order to capitalize on my creativity and to improve my scientific expertise. Moreover, I am indebted with prof. Roger Kelly, a former professor at the University of Trento, whose scientific contributions in collaboration with prof. Miotello inspired my work. I had not the good fortune to meet in person prof. Kelly, but I had the chance to take advantage of his great scientific legacy.

I would like to acknowledge the work of prof. Vincenzo Amendola and prof. Leonid V. Zhigilei who have carefully reviewed the present thesis. I would like to express my sincere gratitude to prof. Zhigilei and his Computational Materials Group at the University of Virginia for their availability for discussions and suggestions on some critical aspects of laser ablation fundamentals.

I am also indebted with many people at the University of Trento for having spent their experience, helping me on specific topics. In particular I am grateful to prof. Francesco Pederiva for having agreed me access to the cluster *Wiglaf* of the theoretical physics group, and I acknowledge the precious support of Giuseppe Froner and Remo Iori for the access to the computational resources. In the experimental work, I took advantage many times of the expertise of Cristina Armellini, dr. Mauro Bortolotti, Massimo Gennara and Enrico Moser.

132